UNIVERSITY OF CALIFORNIA SAN DIEGO

Modeling of implosion dynamics and the magneto-Rayleigh-Taylor instability in single and double liner-on-target, gas-puff Z-pinches

A dissertation submitted in partial satisfaction of the
requirements for the degree
Doctor of Philosophy

in

Engineering Sciences (Mechanical Engineering)

by

Jeffrey Narkis

Committee in charge:

Farhat Beg, Chair
Richard Moyer
Kevin Quest
Hafiz Ur Rahman
Clifford Surko
George Tynan

2019

The dissertation of Jeffrey Narkis is approved, and it is acceptable in quality and form for publication on microfilm and electronically:

_____

_____

_____

_____

_____

_____

Chair

University of California, San Diego

2019

DEDICATION

To my friends, family, and colleagues.

TABLE OF CONTENTS

LIST OF FIGURES

LIST OF TABLES

ACKNOWLEDGEMENTS

This dissertation is the culmination of several years of research that would not have been possible without the support of many others.

First, I would like to thank my committee chair, Farhat Beg. My foray into the wide-ranging discipline of plasma physics from my roots as a mechanical engineer was fraught with steep learning curves, but I am incredibly grateful to have been given the time, freedom, and support to surmount the various challenges during my studies.

I would like to thank Hafiz Rahman for numerous theoretical insights and for being a constant source of encouragement and inspiration, and Paul Ney for allowing me access to the inner workings of the MACH2 code. I would like to thank MIFTI for financial support, and to Emil Ruskov and Frank Wessel for their experimental insights and allowing me to shadow them on multiple experimental campaigns.

Over the many years I have been at UC San Diego, colleagues have come and gone, but I want to thank Gil Collins and Julio Valenzuela who were down in the trenches with me from the very beginning. The many jokes and trips to the soccer field kept me grounded during tough times. I also want to thank Mike Ross and Fabio Conti for their often underappreciated camaraderie, humor, and insight into life as a post-doc. I want to thank Fabio, Julio, and Vlad Fadeev for inclusion in their daily espresso ritual, a constant reminder to enjoy the small things.

My early years were funded in part by my time as a TA and reader, and I am grateful to the various TAs, professors, and lab managers with whom I learned the ins and outs of running large and small-scale engineering courses.

I would like to thank the various institutions and entities that provided funding support in later years. First, I would like to thank the U.S. Department of Energy and ARPA-e, who partially funded the work here under Grant No. DE-AR0000569. I would also like to thank Mike Desjarlais of Sandia National Laboratories, who provided Ar resistivity tables for simulations. Sandia National Laboratories is a multiprogram laboratory managed and operated (at the time the

tables were produced) by Sandia Corporation, a wholly owned subsidiary of Lockheed Martin Corporation, for the U.S. Department of Energy's National Nuclear Security Administration under Contract. No. De-AC04-94AL8500. It is presently operated by National Technology and Engineering Solutions of Sandia, a wholly owned subsidiary of Honeywell International. I would finally like to acknowledge that part of the presented material is based upon work partially supported by the Department of Energy, National Nuclear Security Administration under award No. DE-NA0003842.

I would like to thank Irv Lindemuth for useful discussions about magnetized target fusion, particularly as it relates to Z-pinches, and for his pioneering work in parameter scans that in part motivated the development of the model presented in Chapter 4 of this dissertation.

I would like to thank Marty Marinak and Joe Koning for introducing me to the HYDRA code and providing some useful tutorials on using the various physics packages, including but not limited to MHD and fusion.

Finally, I want to thank my family, friends and acquaintances for their support and acceptance of the various facets of my identity, encouraging me to be myself in a world that demands conformity.

Chapter 2, in part, includes material as it appears in "Investigation of magnetic flux transport and shock formation in a staged Z-pinch", J. Narkis, H. U. Rahman, F. J. Wessel, and F. N. Beg, Phys. Plasmas **24**, 102514 (2017). Chapter 3, in part, includes material as it appears in "Shock formation in Ne, Ar, Kr, and Xe on deuterium gas puff implosions", J. Narkis, H. U. Rahman, P. Ney, M. P. Desjarlais, F. J. Wessel, F. Conti, J. C. Valenzuela, and F. N. Beg, Phys. Plasmas **23**, 122706 (2016). Chapter 4, in part, contains material as it appears in "A semi-analytic model of gas-puff liner-on-target magneto-inertial fusion", J. Narkis, H. U. Rahman, J. C. Valenzuela, F. Conti, R. D. McBride, D. Venosa, and F. N. Beg, Phys. Plasmas **26**, 032708 (2019). J. Narkis was the primary author of these papers.

VITA

2012	Bachelor of Science *with honors* in Mechanical Engineering, Michigan State University Bachelor of Arts *with honors* in Russian, Michigan State University
2016	Master of Science in Engineering Sciences (Mechanical Engineering), University of California San Diego
2019	Doctor of Philosophy in Engineering Sciences (Mechanical Engineering), University of California San Diego

PUBLICATIONS

"Shock formation in Ne, Ar, Kr, and Xe on deuterium gas puff implosions", J. Narkis, H. U. Rahman, P. Ney, M. P. Desjarlais, F. J. Wessel, F. Conti, J. C. Valenzuela, and F. N. Beg, Physics of Plasmas **23**, 122706 (2016).

"Investigation of magnetic flux transport and shock formation in a staged Z-pinch", J. Narkis, H. U. Rahman, F. J. Wessel, and F. N. Beg, Physics of Plasmas **24**, 102514 (2017).

"A semi-analytic model of gas-puff liner-on-target magneto-inertial fusion", J. Narkis, H. U. Rahman, J. C. Valenzuela, F. Conti, R. D. McBride, D. Venosa, and F. N. Beg, Physics of Plasmas **26**, 032708 (2019).

ABSTRACT OF THE DISSERTATION

Modeling of implosion dynamics and the magneto-Rayleigh-Taylor instability in single and double liner-on-target, gas-puff Z-pinches

by

Jeffrey Narkis

Doctor of Philosophy in Engineering Sciences (Mechanical Engineering)

University of California, San Diego, 2019

Farhat Beg, Chair

The gas-puff Staged Z-pinch (SZP) is a magneto-inertial fusion concept in which one or more annular gas-puff liners implode onto a cylindrical target of fusion fuel. This dissertation addresses three topics essential to the viability of the concept: shock preheating of the target, stability of the implosion, and scalability to multi-megaampere drivers.

Shock preheating of the target is necessary because it reduces the required convergence ratio to reach fusion-relevant conditions by raising its adiabat. The strength of the shock is determined by inertial and magnetic forces acting on the target. Initial 1-D magnetohydrodynamic (MHD) simulations of SZP implosions of thin liners show that, while liner resistivity can affect

the onset of shock compression, the final target adiabat is controlled by liner inertia.

As in the conventional Z-pinch, the SZP liner is prone to the magneto-Rayleigh-Taylor (MRT) instability, whose growth must be sufficiently mitigated to maintain liner integrity throughout the implosion. Here, multiple mitigation mechanisms are considered. The first is inherent to a gas-puff Z-pinch liner - modes of wavelengths below a certain minimum can resistively diffuse away. 2-D MHD simulations suggest that Kr and Xe liners have a higher minimum wavelength than Ne and Ar due to their higher resistivity, and later simulations with Ne liners suggest this effect could reduce dominant mode growth below the classical rate, $\sqrt{gk}$.

Two additional mechanisms are implemented: axial premagnetization, which reduces growth via field-line tension, and inclusion of a second liner, which alters the dynamics. 2-D simulations with Ne liners show that stabilization of single and double-liner configurations requires a B_{z0} of 0.5 and 0.2 T, respectively. This reduction is important because there is a rapid drop-off in DD neutron yield for large B_{z0} due to reduced fuel compression.

Finally, a semi-analytic model is developed to assess the scalability of the SZP. After presenting the model, test problems are compared with well-established codes and show reasonable agreement. Then, a simple design study is performed, in which DD neutron yield is optimized on a 850-kA driver and then scaled to 20 MA. Predicted yields agree well with published scaling models and 1-D MHD simulations.

Chapter 1

Introduction

1.1 Introduction

The Z-pinch is one of the oldest and most well-studied topics in plasma physics. When an axial current is applied to a cylinder of plasma, the interaction between the axial current and azimuthal self-magnetic field produces a $\mathbf{J} \times \mathbf{B}$ force directed radially inward. The force either counterbalances thermal expansion, confining the plasma, or compresses the plasma dynamically. There are numerous applications for Z-pinches, because they are capable of efficiently producing high-energy-density plasmas at relatively low cost [1–4]. There are several common experimental configurations (see, e.g. [3] §1.2); among them are fiber, wire-array, solid liner, and gas-puff loads, or some combination of these. Fiber (or exploding wire) Z-pinches are useful as X-ray sources if the material is carbon or metallic (e.g. [5, 6]), and as a fusion source if the material is frozen deuterium (e.g. [6–10]). Wire-array Z-pinches are the dynamic analogue of fiber Z-pinches , notable for their axial uniformity and potential for immense X-ray output (e.g. [11–14]). The inherent azimuthal non-uniformity in wire array Z-pinches is avoided by using a solid liner. The most well-known solid-liner Z-pinches are associated with Magnetized Liner Inertial Fusion (MagLIF) on the Z facility at Sandia National Laboratory [15, 16]. Imploding the heavy solid

liners requires high drive currents (>10 MA) that are not available on university-scale machines. Gas-puff Z-pinches are used on university-scale and higher-current machines (e.g [17–23]) both as an X-ray source and as a neutron source [4].

The work presented here focuses primarily on various configurations of the gas-puff Z-pinch as a source of thermonuclear neutrons, which requires some or all of the load to be deuterium or a deuterium-tritium mixture. The vast majority of experimental work is conducted using deuterium, because tritium is radioactive. Performance of a particular fusion concept is quantified by its thermonuclear neutron yield,

$$Y = n_1 n_2 \langle \sigma v \rangle V \tau \tag{1.1}$$

where n_1, n_2 are the density of reactants with average reaction rate $\langle \sigma v \rangle$ over a volume V and confinement time τ. For a fusion concept to be viable as an energy source, the energy produced in generating Y neutrons must be captured and stored, and it must be larger than the total energy required to produce it. The ratio of this energy to the input energy is commonly referred as gain, and a gain of greater than one is referred to as breakeven.

There is a vast parameter space in which to theoretically reach fusion conditions, but can be broadly categorized according to the method of fuel confinement. Magnetic confinement fusion [24] (MCF) confines fuel along magnetic field lines. Charged particles move in a corkscrew pattern along field lines, with a radius of gyration (Larmor radius) $r_L \equiv mv_\perp/qB$. To avoid end losses, MCF uses toroidal geometry. It operates at relatively low density ($\sim 10^{14}$ cm^{-3}) and for long confinement times ($\sim \mu$s) relative to the predominant counterpart, inertial confinement fusion [25] (ICF). ICF confines fuel with the inertia of an imploding shell or capsule and requires implosion velocities of hundreds of km/s to reach fusion conditions, which are maintained for a short period of time ($\sim$ps) at relatively high density ($> 10^{25}$ cm^{-3}).

A substantial region in parameter space lies in between MCF and ICF that has been

largely unexplored until recently. This category, aptly named magneto-inertial fusion (MIF) or magnetized target fusion (MTF) operates at an intermediate density between ICF and MCF [26–29]. This density requirement (a) relaxes implosion velocity requirements relative to ICF and (b) relaxes stability requirements relative to MCF, and must confine the plasma for longer time than ICF, but not necessarily steady-state as in MCF.

A subset of magneto-inertial fusion concepts based on the Z-pinch have been developed and have received increasing attention in recent years. They are the flow-through Z-pinch [30, 31], Magnetized Liner Inertial fusion (MagLIF) [15, 16, 32], and the Staged Z-pinch (SZP) [10, 33]. The flow-through Z-pinch is more closely analogous to MCF, operating at a low density relative to ICF, but at higher compression than MCF. Because the machine operates at higher compression, it is more prone to instabilities, which are shown to be controlled by the shear induced by axial velocity. MagLIF and SZP are more analogous to ICF in cylindrical geometry, but operate at slower implosion velocity and lower density.

1.2 History of the Staged Z-pinch

The presented work considers topics relevant to SZP. The staging concept, as originally conceived [10, 34], referred to compression of an annular shell ("liner") compressing onto an on-axis cryogenic deuterium fiber, shown in Figure 1.1. In this work, it is assumed a current prepulse is applied such that there is azimuthal premagnetization, i.e. at $t = 0$, $B_\theta(r) = \mu_0 I_0 / 2\pi r$ from $r = a$ to $r = r_i$, where a is the fiber radius and r_i is the inner surface of the liner. Z-pinch compression of the liner by the main current pulse drives the liner toward the axis, and if azimuthal magnetic flux is perfectly conserved inside the liner, the initial prepulse current I_0 would increase as $I(t)/I_0 = \ln[r_{i0}/a_0] / \ln[r_i(t)/a(t)]$, which can grow very large as $r_i \to a$. Current amplification on the fiber is observed, from the initial 200 kA to several MA, exceeding the drive current (2 MA) with I increasing from 1 to an average of 3.5 MA in 0.5 ns, or a dI/dt of 4×10^{15} A/s.

Though the reported results exceed the Lawson criterion [35] by an order of magnitude, the final liner radius of 13 μm is more than a factor of 10^3 smaller than the initial radius of 2 cm and has final thickness ~ 3 μm. Though not performed, a stability analysis of would have been useful to address concerns of instability growth. A cryogenic fiber system was designed [36] but not implemented, so the concept could not be evaluated experimentally.

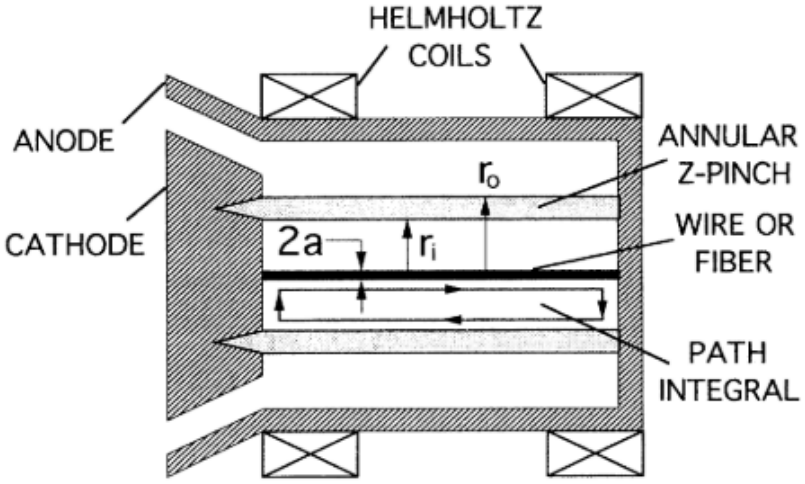

Figure 1.1: Schematic of the original Staged Z-pinch configuration [10], in which an annular Z-pinch liner implodes onto a fiber of frozen deuterium or deuterium-tritium.

The concept evolved [37] to include gas-puff liners. It was theorized that, by using a high-atomic-number (henceforth high Z_A) liner, the liner would radiate significantly, remaining highly magnetically diffusive. Resistive diffusion of the magnetic field tends to smooth out instabilities [4, 38], and because the target is conductive, a non-negligible azimuthal magnetic field can develop at the interface between the liner and the target. This has two potential effects: first, if either the electron or ion Hall parameter ($\omega_{ce}\tau_{ei}$, $\omega_{ci}\tau_{ii}$) is significantly greater than one, this reduces thermal conduction from the target to the liner [26, 39, 40]. It was also proposed recently [41] that if the interfacial $\mathbf{J}_z \times \mathbf{B}_\theta$ force were large enough, it could drive some or all of the target compression rather than the inertia of the liner. However, the internal azimuthal magnetic field profile has yet to be measured in experiment.

As noted by [4], gas-puff onto wire or central gas-jet experiments have been successfully demonstrated to be a source of high-energy electron beams, so the concept of staged energy transfer is not unique to the SZP, and an increased neutron yield in SZP-type loads (high Z_A outer liner, D_2) over pure D_2 have been shown to increase yield over pure D_2 loads in 1-D simulations. Experimental observations and simulations have shown an order of magnitude increase in neutron yield by a factor of 10 on a single-MA machine [42]. Much higher yields have been reported from SZP simulations, e.g. [43], but to produce those yields, the final target radius is a factor of ~ 200 less than the initial radius. There is significant interest in reducing this ratio for SZP-type loads while retaining similar yields, but to discuss this further it is useful to introduce some essential Z-pinch physics.

1.3 Motivation

1.3.1 Bennett and Pease-Braginskii equilibria

Z-pinches were one of the first concepts explored for thermonuclear fusion, with early modeling attempts based on the Bennett [44] and Pease-Braginskii [45, 46] equilibria. The Bennett equilibrium describes a Z-pinch in which the external magnetic pressure balances the internal plasma pressure. Since pinch losses are primarily radiative, the radiation losses must be balanced by additional heating. In an equilibrium, the only heating mechanism is ohmic, and the balancing of ohmic heating with radiation loss leads to the Pease-Braginskii equilibrium. Their brief derivations follow.

The simplest formulation of a Z-pinch in equilibrium assumes that the plasma pressure, p, is balanced by the vacuum $\mathbf{J}\times\mathbf{B}$ force, $\nabla p = \mathbf{J}\times\mathbf{B}$. Using Ampere's law (neglecting displacement current here and throughout), $\nabla\times\mathbf{B} = \mu_0\mathbf{J}$, and assuming all quantities are functions of radius, r,

this becomes

$$\frac{\partial}{\partial r}\left(p+\frac{B_\theta^2}{2\mu_0}+\frac{B_z^2}{2\mu_0}\right)+\frac{B_\theta^2}{\mu_0 r}=0 \tag{1.2}$$

Assuming $B_z = 0$ and a uniform axial current density, such that $B_\theta(r) = \mu_0 I r/2\pi R^2$, upon integration this gives

$$p=\frac{\mu_0 I^2}{4\pi^2 R^2}\left(1-\frac{r^2}{R^2}\right) \tag{1.3}$$

Introducing ion line density $N \equiv 2\pi\int_0^R rn(r)dr$, and taking $p = nk_B(T_i + \bar{Z}T_e)$ and assuming constant temperature, this gives

$$Nk_B(T_i+\bar{Z}T_e)=\frac{\mu_0 I^2}{8\pi}, \tag{1.4}$$

what is called the Bennett relation [44]. The time-scale of the equilibrium described by this relation is the Alfvén transit time, $\tau_A = R/v_A$, where $v_A^2 \equiv B^2/\mu_0\rho$ is the Alfvén speed. The Bennett relation is useful in that it provides an equilibrium temperature provided N, I, and $\bar{Z}$.

However, in order to sustain this equilibrium, energy losses must be offset by continuous heating. In a pure Z-pinch, radiation losses are the dominant mechanism, and in equilibrium the only plasma heating is ohmic. In a deuterium or deuterium-tritium Z-pinch, radiation losses are predominantly due to bremsstrahlung, or "braking radiation", produced by the acceleration of a charge in the Coulomb field of another charge [47]. This is also called free-free emission, since the radiating particle is unbound both before and after the acceleration. In Z-pinches we are generally interested in thermal bremsstrahlung, so the emission power density per unit frequency range is averaged over a thermal distribution of speeds, and then integrated over frequency to give [48]

$$P_{Br}=\frac{16\sqrt{2\pi}}{3\sqrt{3}}\frac{\left(\frac{e^2}{4\pi\varepsilon_0}\right)^3}{\hbar(m_e c^2)^{3/2}}\bar{Z}^2 n_e n_i (k_B T)^{1/2}\,\bar{g}_B \approx 1.5\times10^{-38}\,(T_e\ [\mathrm{eV}])^{1/2}\,\bar{Z}^2 n_e n_i \bar{g}_B\ [\mathrm{W/m^3}] \tag{1.5}$$

where n_e, n_i have units m^{-3} and $\bar{g}_B$ is a frequency average of the velocity-averaged Gaunt factor, which is in the range 1.1 to 1.5. Typically a value of $\bar{g}_B = 1.2$ is used. The total radiation power is simply this quantity integrated over the volume of the pinch. The power equilibrium [1] for ohmic heating ηJ^2 and bremsstrahlung is then

$$2\pi \int_0^R \eta J^2 r dr = 2\pi \int_0^R P_{Br} r dr \tag{1.6}$$

Assuming $T_e = T_i$, η and J constant, and drawing from the Bennett relation, $n = \frac{1}{k_B T_i (1+\bar{Z})} \frac{\mu_0 I^2}{4\pi^2 R^2} \left(1 - \frac{r^2}{R^2}\right)$, this yields

$$I = (4\pi\varepsilon_0)^{3/2} \left(\frac{9\pi\sqrt{3}}{16\sqrt{2\pi}\bar{g}_B}\right)^{1/2} \frac{\hbar^{1/2} m_e c^{3/2}}{e^2} \left(\frac{1+\bar{Z}}{\bar{Z}}\right) (\ln\Lambda)^{1/2} \approx 0.22 \left(\frac{1+\bar{Z}}{\bar{Z}}\right) (\ln\Lambda)^{1/2} \text{ [MA]} \tag{1.7}$$

where the transverse Spitzer resistivity [49]

$$\eta_\perp = \frac{\pi \bar{Z} m_e^{1/2} \ln\Lambda}{(4\pi\varepsilon_0)^2 (k_B T)^{3/2}} \approx 1.04 \times 10^{-4} \bar{Z} \ln\Lambda (T \text{ [eV]})^{-3/2} \tag{1.8}$$

has been used. Eqn. [1.7] is called the Pease-Braginskii current, I_{PB} [1, 3, 45, 46]. If a plasma is in an equilibrium satisfying the above conditions, increasing the current I above $I > I_{PB}$ will result in radiation losses exceeding ohmic heating, and the pinch contracts. When $I < I_{PB}$, ohmic heating exceeds losses and the pinch expands. For a fusion plasma, $I_{PB} \sim 1$ MA. However, charged fusion byproducts (e.g. $\mathrm{D} + \mathrm{T} \rightarrow \mathrm{n} + \mathrm{He}^{2+}$) can redeposit their energy into the fuel and prevent radiative collapse, provided the gyroradius $r_L \equiv mv/\bar{Z}eB$ is small relative to the pinch radius, where v is the birth velocity of an α-particle. For example, $r_{L\alpha} = 50\ \mu$m for a 2.7 MA current on a DT fiber that has expanded to 100 μm. Experiments (e.g. [7, 9]) and simulations (e.g. [50]) showed, however, that such a configuration was highly susceptible to the sausage (m=0) instability.

1.3.2 Dynamic constraints of inertially-confined Z-pinch fusion

If the target plasma is inertially confined, the Pease-Braginskii constraint is no longer applicable because the predominant heating is due to adiabatic compression. However, thermal conduction losses from the imploding fuel to the liner or shell become significant, so they must be considered in addition to radiation losses. If the fuel is magnetized ($\omega_{ce}\tau_{ei} \gg 1$), this can reduce thermal conduction losses, and trap charged particles, as in the fiber Z-pinch. As noted previously, this has the effect of reducing driver requirements and motivated interest in MIF/MTF.

The parameter space between ICF and MCF is large, so in the interest of developing a high-level picture of the viability of MTF, Lindemuth and Kirkpatrick [26] developed a 0-D model of an imploding shell/fuel system. In this model, they assumed adiabatic compression of a spherical target (with separate T_i and T_e) surrounded by a shell driven with a velocity specified by the initial kinetic energy of the shell. Losses by radiation, ion and electron thermal conduction are estimated, as well as α-particle energy deposition. In the event the initial velocity is large relative to the sound speed, shock heating of the fuel is treated simply by raising the initial temperature to $m_i v_0^2/6$. The results of their study confirmed driver requirements in excess of 10 cm/μs (100 km/s) for gain greater than unity for unmagnetized fuel, and found regions with lower velocity and density than conventional ICF (0.1-10 cm/μs, $\rho_0 \sim 10^{-6}$ g/cc) could produce gains greater than unity as well. The model was recently extended [51] to include cylindrical targets embedded with an azimuthal or axial magnetic field, demonstrating gains in excess of 25 were possible for each configuration.

For a Z-pinch magneto-inertial fusion concept to viable, the final radius of the target must be large enough so that the target column does not disrupt due to either stationary or acceleration-driven instabilities. Conventionally, the form places a constraint on the target convergence ratio (CR), or ratio of the initial radius to the final radius. For inertially confined implosions, an upper limit of CR$\sim$ 30 is a typical upper limit. In a purely adiabatic, cylindrical implosion with a CR of $10^{3/2} \approx 31.6$, initial density $n_i = n_f/\mathrm{CR}^2 = n_f/1000$, and initial temperature

$T_i = T_f/\mathrm{CR}^{4/3} = T_f/100$, assuming the ratio of specific heats, $\gamma = 5/3$. Therefore, to reach fusion relevant temperatures, an effective initial temperature in excess of $\sim 10^2$ eV is necessary.

There are generally two approaches for achieving the required effective initial temperature. One method, which is employed in MagLIF [15, 52], is to use the Z-beamlet laser as an external preheating source to deposit energy in the fuel immediately prior to compressing the load. This approach inherently introduces additional complexities, e.g. the uniformity of energy deposition, the propagation of the burn wave, that are actively under investigation. Another method, which is employed in SZP, is preheating by shock compression of the fuel.

Shock preheating is attractive due to its inherent simplicity, with the strength of preheating largely determined by the implosion velocity of the target. Neglecting cylindrical convergence, the post-shock temperature of a strong hydrodynamic shock (in DT) is related to the implosion velocity as

$$T\ [\mathrm{eV}] \approx 48.6 \left(\frac{v[\mathrm{km/s}]}{100} \right)^2 = 48.6 \left(\frac{v[\mathrm{cm}/\mu\mathrm{s}]}{10} \right)^2 \tag{1.9}$$

For deuterium, 48.6 is replaced with 38.9. Shock compression introduces an additional factor of ~ 2 to the CR, so to maintain the same overall CR, the post shock temperature must be a factor of $2^{4/3} \approx 2.5$ higher. Without accounting for losses, implosion velocities on the order of ~ 250 km/s are required, which is approaching conventional ICF velocities. However, In SZP simulations [53] and experiments [54] at the 1-MA current level, this implosion velocity is easily exceeded. This implosion velocity is only required for shock preheating and not adiabatic compression, so one might hypothetically imagine a staged target implosion that is initially fast to provide the required shock strength, then slows to MagLIF-type velocities behind the shock front. Rahman [41] has recently proposed that a diffused magnetic piston could provide the initial shock heating, followed by inertial adiabatic compression. To some degree, this was observed in [53], but the magnitude of the diffused $\mathbf{J} \times \mathbf{B}$ force was relatively small and became dominated by liner inertia as the implosion became snowplow-like. This remains an area of active investigation.

Reaching such high implosion velocity necessarily requires significant acceleration, which

means the Z-pinch load is highly susceptible to acceleration-driven instabilities. The most damaging is the Rayleigh-Taylor instability [55, 56], in which a heavy fluid is compressed by a lighter fluid. If the lighter fluid is a magnetic field, then it is called the magneto-Rayleigh-Taylor instability (MRTI) [57–59]. The initial drive for Z-pinch fusion was significantly hindered by analyses showing that MRTI growth was significant [1], but in recent years mitigation mechanisms have received more attention.

Several mitigation mechanisms have been proposed and successfully demonstrated in gas-puff Z-pinch experiments [2, 4, 60], including the SZP ([54, 61]). Among the mechanisms are axial premagnetization (e.g. [62, 63]), density profile tailoring (e.g. [64, 65]), and (potentially) resistive diffusion effects by using a higher atomic number liner [4]. Qualitatively, the last could explain decreasing MRT growth with higher Z_A liners observed in simulations in [53], but was not explored in that work. Here we will expand on that and previous work on MRT stabilization of SZP implosions in simulations.

1.4 Magnetohydrodynamic modeling

Analytic, semi-analytic, and 0-D models are incredibly useful in performing high-level parameter scans that guide the point design for a particular experiment. However, as noted in (e.g.) [26, 51] they serve as starting points for more detailed simulations. To capture the physics in a SZP implosion with the highest possible fidelity, one would ideally run 3-D kinetic simulations, and then couple it to some sort of Monte Carlo model for neutron generation. This would allow, for example, non-Maxwellian particle distributions, and the production of beam-target neutrons. It has been shown in fully kinetic simulations that on lower current drivers ($\sim$ 1 MA), the primary source of deuterium neutrons in a pure deuterium Z-pinch is from beam-target [66]. One could also consider mixing of liner and target, which can significantly reduce neutron yield - especially for highly-radiative high-Z_A liners as in SZP. However, these simulations are incredibly

computationally expensive and requires access to the appropriate resources.

The next level down in precision is 3-D resistive and/or extended-magnetohydrodynamic (MHD) simulations, where the "extension" refers to additional terms included in Ohm's law, like the Hall, Ettinghausen, and Nernst effects. Such codes have been used for simulating Z-pinch implosions, e.g. GORGON [21, 67, 68], PERSEUS [69, 70] to explain physics that arise from azimuthal asymmetry, e.g. the helical structures observed in MagLIF implosions [71–73]. MHD is valid on length scales greater than the Debye length and electron/ion gyroradii, and on timescales longer than the inverse of the plasma and cyclotron frequencies. Furthermore, the plasma must be sufficiently collisional so that its distribution can be approximated as Maxwellian. It is often the case, especially on university-scale Z-pinches, that ion and electron temperatures are unequal. But, to enforce quasineutrality, there is only a single fluid velocity. Radiation losses are often included by solving the radiation diffusion equation, and adding a coupling term between the electron energy and radiation equations. 3-D MHD simulations, while not as expensive as kinetic simulations, can be prohibitively expensive.

For many of the relevant physics, we can assume azimuthal symmetry and rely on 1-D and 2-D simulations. The majority of published simulations of SZP implosions [37, 41, 43, 61] are performed using the radiation-MHD code MACH2 [74]. The groundwork for the material in Chapter 3, which led to [53], was also simulated using MACH2. In that and later chapters, we will also discuss 1-D and 2-D HYDRA [75] simulation results. The HYDRA code is primarily used for simulating unmagnetized target implosions on the NIF, but MHD capability has been added recently for magnetized target implosions [76].

Both codes solve the resistive MHD equations, as well as include a radiation transport model. The radiation transport model is the single-group (in MACH2) or multi-group (HYDRA) radiation diffusion equation, where a group is defined by a range of photon energies (frequencies), and radiation energy diffuses according to a coefficient that is a function of a frequency-averaged opacity. A single fluid velocity is used, enforcing charge quasineutrality of the fluid. Both

codes have some form of extended-MHD capabilities, but their functionality is limited. As such, we use the simplified Ohm's law to describe the electric field: $\mathbf{E} \equiv \bar{\bar{\eta}} \cdot (\mathbf{J} + \mathbf{v} \times \mathbf{B})$. Ion and electron energies are treated separately, which is important for modeling SZP implosions on university-scale machines.

The two-temperature resistive MHD equations are conservation of mass, momentum, ion energy, electron energy, radiation energy, and magnetic flux, compactly summarized here as:

$$\frac{\partial \rho}{\partial t} + \nabla \cdot (\rho \mathbf{v}) = 0, \tag{1.10}$$

$$\rho \left(\frac{\partial}{\partial t} + \mathbf{v} \cdot \nabla \right) \mathbf{v} = -\nabla \left(p + q + \frac{B^2}{2\mu_0} \right) - (\mathbf{B} \cdot \nabla)\mathbf{B}, \tag{1.11}$$

$$\rho \left(\frac{\partial}{\partial t} + \mathbf{v} \cdot \nabla \right) \varepsilon_e + p_e \nabla \cdot \mathbf{v} = \eta J^2 + \nabla \cdot (\kappa_e \nabla (k_B T_e)) - \Phi_{eR} - S_{ei}, \tag{1.12}$$

$$\rho \left(\frac{\partial}{\partial t} + \mathbf{v} \cdot \nabla \right) \varepsilon_i + (p_i + q) \nabla \cdot \mathbf{v} = \nabla \cdot (\kappa_i \nabla (k_B T_i)) + S_{ei}, \tag{1.13}$$

$$\left(\frac{\partial}{\partial t} + \mathbf{v} \cdot \nabla \right) E_R + \frac{4}{3} E_R \nabla \cdot \mathbf{v} = \nabla \cdot (\kappa_R \nabla E_R) + \Phi_{eR}, \tag{1.14}$$

$$\frac{\partial \mathbf{B}}{\partial t} = \nabla \times (\mathbf{v} \times \mathbf{B}) - \nabla \times (\eta \mathbf{J}) \tag{1.15}$$

where we have taken isotropic resistivity, η, thermal conductivity, κ, and pressure, $p = p_i + p_e$; q is artificial viscous pressure, $\varepsilon_{e,(i)}$ is specific electron (ion) internal energy, κ_R is a radiation diffusion coefficient, E_R is radiation energy, and S_{ei} and Φ_{eR} are coupling terms for electron-ion equilibration and radiation, respectively.

1.5 Thesis organization

Chapter 2 provides an analytical background for topics relevant to the SZP. The various simplified theories used to describe Z-pinch implosions are discussed. In addition to the standard Z-pinch models, the groundwork is laid for discussions of shock formation and MRTI growth in gas-puff Z-pinches, as well as for magnetic flux transport via a Korteweg-de Vries-Burger

equation for magnetoacoustic waves. The limitations of the theories are discussed, thus motivating the simulations presented in the chapters that follow.

Chapter 3 primarily discusses the work that led to the work in [53]. In this work, the role of liner Z_A was considered in the context of azimuthal magnetic field evolution and shock formation in 1-D MACH2 simulations, and MRTI growth in 2-D MACH2 simulations with $B_{z0} = 0$. This work is also extended to MRTI mitigation by application of an axial magnetic field using HYDRA.

In Chapter 4, a semi-analytic model for SZP is developed. The semi-analytic model is based on SAMM, a semi-analytic model for MagLIF [77], but includes additional models for physics relevant to SZP implosions. Two sample problems are presented: first, a comparison of an SZP implosion with the model and with HYDRA, and second: results for a MagLIF implosion model are compared to those obtained in SAMM, to show the modifications do not obtain significantly different results in the MagLIF parameter regime. They are followed by an optimization and scaling study for a newly-constructed linear transformer driver at UC San Diego. The deuterium neutron yield scaling with peak driver current is shown to agree reasonably with other published models in the literature.

Chapter 5 discusses implosion dynamics and MRTI growth in double liner-on-target (or "triple-shell") gas puff Z-pinches. Current and recent work on this load configuration on other machines is briefly reviewed, as well as the motivation for using the configuration from analytical work. Following this introduction, HYDRA and MACH2 simulation results are presented, which consider the effects of liner material, geometry, and axial premagnetization on shock formation in the target and MRTI growth mitigation.

Chapter 6 summarizes the completed work and discusses potential avenues for future work.

Chapter 2

Z-pinch, MRT, and shock theory

2.1 Introduction

The purpose of this chapter is to begin with the elementary theories describing the implosion and stability of a dynamic, gas-puff Z-pinch and discuss the simplifications needed to obtain the presented solutions, which will then provide the motivation for using resistive MHD simulations in the chapters that follow. Where convenient, derivations will preserve cylindrical geometry, but it is generally the case that the phenomena we are considering (from an analytical perspective) occur at sufficiently large radii that a planar approximation is acceptable, or that the inclusion of effects due to cylindrical geometry significantly complicates the analysis without providing much in additional insight.

This section provides the groundwork for the sections that follow. Much of Z-pinch theory was developed prior to the widespread availability of computer codes; the common 0-D models are presented and discussed briefly. Following a presentation of these models, the growth rate for the magneto-Rayleigh-Taylor is presented in planar and cylindrical ideal MHD. Effects due to resistivity are discussed. Finally, a planar Korteweg-de Vries-Burgers equation for magnetoacoustic waves is presented.

2.2 Analytic Z-pinch models

2.2.1 On-axis gas-puff snowplow

One of the earliest and well-known Z-pinch model is the 0-D "snowplow", in which all imploded mass is swept up on the surface of the magnetic piston at radius r. In the original derivation by Rosenbluth [78], a constant mass density profile is assumed. However, a gas puff typically has an initial density profile of the form $\rho(R,t=0)=\rho_0\exp\left(-\alpha R^2\right)$ that extends to some initial radius R_0. The mass per unit length M swept up by the piston is then

$$M(t)=\int_{R(t)}^{R_0}2\pi r\rho_0\exp\left(-\alpha r^2\right)dr=\frac{\pi\rho_0}{\alpha}\left[\exp\left(-\alpha R(t)^2\right)-\exp\left(-\alpha R_0^2\right)\right] \tag{2.1}$$

The equation of motion of the surface is then

$$R\frac{d}{dt}\left(\left[\exp\left(-\alpha R(t)^2\right)-\exp\left(-\alpha R_0^2\right)\right]\frac{dR}{dt}\right)=-\frac{\alpha\mu_0 I^2}{4\pi^2\rho_0} \tag{2.2}$$

where $I=I(t)$ is an applied axial current. This current often has the form $I=I_0\sin^x(\pi t/2t_R)$, where x is 1 or 2 and t_R is the time of peak current. The value of α can be rewritten as $\alpha=4\ln 2/(\Delta)^2=4\ln 2/(fR_0)^2=f_*/R_0^2$, where Δ is the full-width at half-maximum (FWHM) of the gas puff, which is a fraction f of R_0. Taking $R_*=R/R_0$ and $\tau=t/t_R$, we then have

$$R_*\frac{d}{d\tau}\left(\left[\exp\left(-f_*R_*^2\right)-\exp(-f_*)\right]\frac{dR_*}{d\tau}\right)=-\frac{\mu_0 I_0^2 f_* t_R^2}{4\pi^2\rho_0 R_0^4}\sin^{2x}(\pi\tau/2) \tag{2.3}$$

The parameters I_0, t_R, f_*, R_0, x are known for a particular driver, which leaves ρ_0 as the only constraint on implosion time. Generally, ρ_0 is chosen such that $R_*=0$ at approximately t_R. As an example, consider a gas puff with $f_*=10$ ($f\approx 0.52655$), $I_0=1$ MA, $t_R=100$ ns, $R_0=1$ cm, and $x=2$. The solutions of Eq. [2.3] for several values of ρ_0 are shown in Figure 2.1. The pinch implodes earlier in time than for a uniform density profile, because a larger mass fraction is

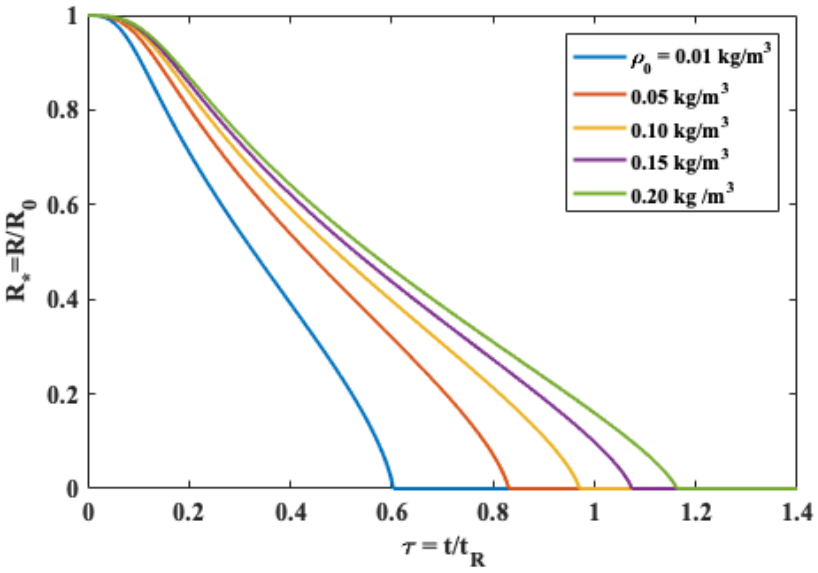

Figure 2.1: Solutions to Eq. [2.3] with $I(t)$ [MA] $= \sin^2(\frac{\pi}{2}\frac{t}{t_R})$, $t_R = 100$ ns, $R_0 = 1$ cm, and $f_* = 10$ (FWHM $= 0.52655R_0$) for peak density values of 0.01, 0.05, 0.10, 0.15, and 0.20 kg/m^3.

on-axis. A similar exercise can be done for wire arrays or hollow gas-puff, but in this case all the mass is already swept up at $t = 0$. This is often called the thin-shell model (e.g. [3]).

2.2.2 Double gas-puff snowplow

It is of interest to extend the snowplow problem of the previous section to one that consists of an annular gas-puff imploding onto an on-axis gas-puff, as this is the general structure of a SZP load. In the snowplow approximation, the only difference is accounting for the change in M,

which is now

$$M(t) = \int_{R(t)}^{R_0} 2\pi r \left[\rho_1 \exp\left(-\alpha_1 r^2\right) + \rho_2 \exp\left(-\alpha_2 (r - r_c)^2\right)\right] dr = \frac{\pi\rho_1}{\alpha_1}\left[\exp\left(-\alpha_1 R(t)^2\right) - \exp\left(-\alpha_1 R_0^2\right)\right] + \frac{\pi\rho_2}{\alpha_2}\left[r_c\sqrt{\pi\alpha_2}\left\{\mathrm{erf}\left(\sqrt{\alpha_2}(R_0 - r_c)\right) - \mathrm{erf}\left(\sqrt{\alpha_2}(R(t) - r_c)\right)\right\} + \exp\left(-\alpha_2 (R(t) - r_c)^2\right) - \exp\left(-\alpha_2 (R_0 - r_c)^2\right)\right] \quad (2.4)$$

where $\rho_1,\ \alpha_1$ describe the on-axis gas-puff, and $\rho_2,\ \alpha_2$ describe the annular gas-puff centered at r_c. The equation of motion is then

$$R\frac{d}{dt}\left(\frac{\pi\rho_1}{\alpha_1}\frac{dR}{dt}\left[\exp\left(-\alpha_1 R(t)^2\right) - \exp\left(-\alpha_1 R_0^2\right)\right] + \frac{\pi\rho_2}{\alpha_2}\frac{dR}{dt}\left[r_c\sqrt{\pi\alpha_2}\left\{\mathrm{erf}\left(\sqrt{\alpha_2}(R_0 - r_c)\right) - \mathrm{erf}\left(\sqrt{\alpha_2}(R(t) - r_c)\right)\right\} + \exp\left(-\alpha_2 (R(t) - r_c)^2\right) - \exp\left(-\alpha_2 (R_0 - r_c)^2\right)\right]\right) = -\frac{\mu_0 I^2}{4\pi} \quad (2.5)$$

which, upon the same assumptions as before and introducing $M_* = \frac{\pi\rho_2}{\alpha_2}/\frac{\pi\rho_1}{\alpha_1}$, $N_* = r_c\sqrt{\pi\alpha_2}$, $f_{i*} = \alpha_i R_0^2$, $A_* = \mathrm{erf}(\sqrt{\alpha_2}(R_0 - r_c))$, and $r_{c*} = r_c/R_0$, is nondimensionalized to give

$$R_*\frac{d}{d\tau}\left(\frac{dR_*}{d\tau}\left[\exp\left(-f_{1*}R_*^2\right) - \exp(-f_{1*})\right] + M_*\frac{dR_*}{d\tau}\left[N_*\left\{A_* - \mathrm{erf}\left(\sqrt{f_{2*}}(R_* - r_{c*})\right)\right\} + \exp\left(-f_{2*}(R_* - r_{c*})^2\right) - \exp\left(-f_{2*}(1 - r_{c*})^2\right)\right]\right) = -\frac{\mu_0 I_0^2 f_{1*} t_R^2}{4\pi^2\rho_1 R_0^4}\sin^{2x}(\pi t/2) \quad (2.6)$$

Continuing with the example from the previous section, let R_0 now equal 2 cm, use gas puffs of similar geometry such that $f_{1*} = f_{2*} = 40$, and let $r_c = 1.2$ cm. The solutions to Eq. [2.6] for $\rho_1 = 10^{-2},\ 10^{-3}$ kg/m^3 and $\rho_2 = 5\times10^{-4},\ 1\times10^{-3},\ 2\times10^{-3}$ kg/m^3 are shown in Figure 2.2. The solutions for $\rho_1 = 10^{-2}$ kg/m^3 are denoted by the dotted lines.

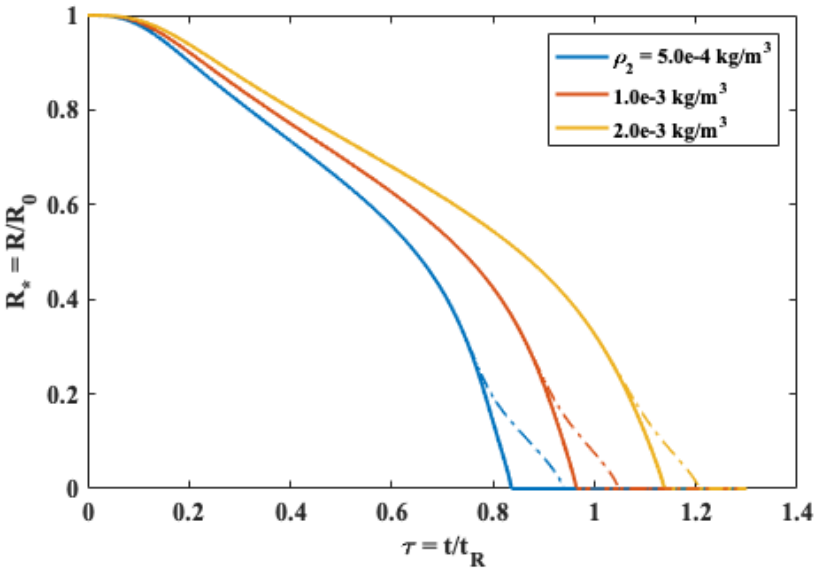

Figure 2.2: Solutions to Eq. [2.6] with $I(t)$ [MA] $= \sin^2(\frac{\pi}{2}\frac{t}{t_R})$, $t_R = 100$ ns, $R_0 = 2$ cm, and $f_{1*} = f_{2*} = 40$ (FWHM $= 0.526$ cm) for ρ_2= 5.0e-4, 1.0e-3, 2.0e-3 kg/m^3 and $\rho_1 = 1.0$e-3, 1.0e-2 kg/m^3. The dotted trajectories are for $\rho_1 = 1.0$e-2 kg/m^3.

2.2.3 Slug model

If the radial implosion velocity of a Z-pinch is supersonic, then a shock front will develop ahead of the external piston. Potter [79] developed a "slug" model that assumes the Rankine-Hugoniot conditions are applicable across a shock front, which will briefly reproduce here. When a strong shock is assumed (see next section), the following relations hold (taking $\gamma = 5/3$):

$$u_2 = \frac{3}{4}u_s, \tag{2.7}$$

$$\rho_2 = 4\rho_1, \tag{2.8}$$

$$p_2 = \frac{3}{4}\rho_1 u_s^2 \tag{2.9}$$

Taking $p_2 = \rho_2 k_B T_2/m$, the pressure jump condition can also be written in terms of temperature,

$$T_2 = \frac{3}{16}\frac{m}{k_B}u_s^2, \tag{2.10}$$

where u_s is the shock-front velocity and $u_2,\ p_2,\ T_2$ are post-shock quantities. Eq. [2.10] is the general form for Eq. [1.9]. The sound speed of the post-shock temperature, $c_S = \sqrt{\gamma p_2/\rho_2}$, is generally greater than u_2, so in this model it is assumed that post-shock quantities are constant. This also means the post-shock region undergoes adiabatic heating, i.e. $pV^\gamma = \text{const.}$, or $\gamma p dV + V dp = 0$.

The volume of the shocked plasma is $V = \pi(r_p^2 - r_s^2)$, which evolves as

$$dV = 2\pi(r_p dr_p - \frac{3}{4} r_s dr_s) \tag{2.11}$$

where the factor $3/4$ is from Eq. [2.7] to reconcile the fact that the adiabatic law applies to an instantaneously fixed mass of gas with the fact that mass is being added to the post-shock region. From Eq. [2.9], $dp_s/du_s = 6/4\rho_0 u_s = 2p_s/u_s$. Substituting into the adiabatic law yields

$$r_p dr_p - \frac{3}{4} r_s dr_s + \frac{3}{5}(r_p^2 - r_s^2)\frac{du_s}{u_s} = 0 \tag{2.12}$$

Since the post-shock pressure is uniform, it must be equal to the pressure of the magnetic piston, i.e.

$$\frac{\mu_0 I^2}{8\pi^2 r_p^2} = \frac{3}{4}\rho_1 u_s^2 \rightarrow u_s = -\left(\frac{\mu_0}{6\pi^2\rho_1}\right)^{1/2} \frac{I}{r_p} \tag{2.13}$$

From Eq. [2.13] it is easily shown that $du_s/u_s = -dr_p/r_p$, which in combination with Eq. [2.12] gives

$$\frac{dr_p}{dr_s} = \frac{3}{4}\frac{r_s}{r_p}\left(\frac{2}{5} + \frac{3}{5}\frac{r_s^2}{r_p^2}\right)^{-1} \tag{2.14}$$

and thus

$$\frac{dr_p}{dt} = \frac{dr_p}{dr_s} u_s \tag{2.15}$$

Eqs. [2.12] and [2.13] give r_p and r_s for a known $I(t)$ and ρ_1. If $I(t) = I$ and $\rho_1(r) = \rho_0$ and Eq. [2.13] is nondimensionalized by taking $r_{s,p} = r_{s*,p*} r_0$ and $t = \tau(\rho_0/\mu_0)^{1/2} 4\pi r_0^2/I$, this

becomes

$$\frac{dr_{s*}}{d\tau} = \frac{-(8/3)^{1/2}}{r_{p*}}, \frac{dr_{p*}}{d\tau} = \frac{-3(8/3)^{1/2} r_{s*}}{4r_{p*}^2}\left(\frac{2}{5} + \frac{3}{5}\frac{r_{s*}^2}{r_{p*}^2}\right)^{-1} \tag{2.16}$$

With the initial conditions $r_{s*}(t=0) = r_{p*}(t=0) = 1$, this gives the solution shown in Fig. 2.3, cf. [79], Fig. 2.

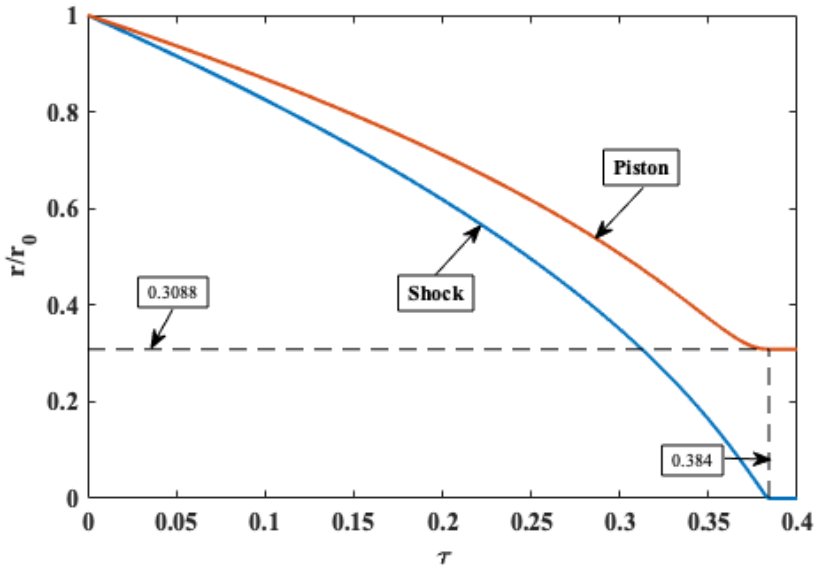

Figure 2.3: Solutions to Eq. [2.16] for $r_{s*}(\tau=0) = r_{p*}(\tau=0) = 1$, cf. [79], Fig. 2. The shock front arrives on axis at $\tau = 0.384$, at which time the piston radius, $r_{s*} = 0.3088$.

In the context of a gas-puff Z-pinch, we could also consider $\rho(r) = \rho_0 \exp(-\alpha r^2)$ and $I(t) = I_0 \sin^2(\pi t/2t_R)$, and nondimensionalize time with respect to t_R to give

$$\frac{dr_{s*}}{d\tau} = -\left(\frac{\mu_0}{6\pi^2\rho_0}\right)^{1/2} \frac{I_0 t_R}{r_0^2} \frac{1}{r_{p*}[\exp(-f_* r_{s*}^2)]^{1/2}} \sin^2(\pi\tau/2) \tag{2.17}$$

$$\frac{dr_{p*}}{d\tau} = \frac{-3}{4}\left(\frac{\mu_0}{6\pi^2\rho_0}\right)^{1/2} \frac{I_0 t_R}{r_0^2}\left(\frac{2}{5} + \frac{3}{5}\frac{r_{s*}^2}{r_{p*}^2}\right)^{-1} \frac{r_{s*}/r_{p*}}{r_{p*}[\exp(-f_* r_{s*}^2)]^{1/2}} \sin^2(\pi\tau/2) \tag{2.18}$$

where f_* has the same definition as before. The solution to Eq. [2.18] can be compared to that of the snowplow, as in Fig. 2.4. There is general agreement between the two models in implosion trajectory, but the usefulness of both models does not extend much beyond providing implosion

time.

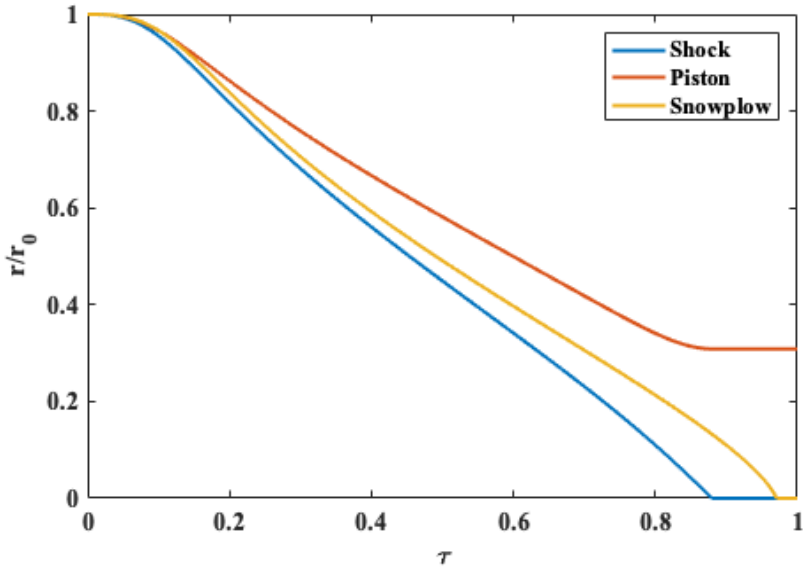

Figure 2.4: Solutions to Eq. [2.18] (for shock at radius r_{s*} and piston at radius r_{p*}) compared with the solution to Eq. [2.3] for $\rho_0 = 0.01$ kg/m^3, $f_* = 10$, $r_0 = 1$ cm, $I(t)$ [MA] $= \sin^2(\pi t/2t_R)$, $t_R = 100$ ns.

2.3 Planar Rankine-Hugoniot relations for MHD

The slug model in the previous model assumes a strong shock $p_2 \gg p_1$, but this is not necessarily true. In this section the planar Rankine-Hugoniot relations for an MHD shock are derived. Shocks are known to accelerate due to cylindrical convergence, but as in other order-of-magnitude models of Z-pinches (e.g. [79], [15]) we will neglect this. We can neglect the effects of resistive diffusion in the context of shock formation in a deuterium plasma because the magnetic Reynolds number, $Lu\mu_0/\eta \gg 1$ for an imploding pinch. Furthermore, we will assume that $T_i = T_e$ and $\bar{Z} = 1$. The first is only true provided the electron-ion equilibration timescale is small relative to the implosion timescale, which is not necessarily valid.

Following [80], mass, momentum, and energy flux are conserved across a planar MHD discontinuity. The normal component of magnetic field and the tangential component of the

electric field are also continuous. Taking $\vec{e}_x$ as the surface normal of the discontinuity, in the reference frame of the shock the jump conditions are

$$[B_x] = 0, \tag{2.19}$$

$$[\mathbf{u}_\perp B_x - u_x \mathbf{B}_\perp] = 0, \tag{2.20}$$

$$[\rho u_x] = 0, \tag{2.21}$$

$$\left[p + \rho u_x^2 + \frac{1}{2\mu_0}(\mathbf{B}_\perp^2 - B_x^2)\right] = 0, \tag{2.22}$$

$$\left[\rho u_x \mathbf{u}_\perp - \frac{1}{\mu_0} B_x \mathbf{B}_\perp\right] = 0, \tag{2.23}$$

$$\left[u_x\left(\frac{\gamma}{\gamma-1}p + \frac{\rho u^2}{2}\right) + \frac{1}{\mu_0}\left(u_x B^2 - B_x(\mathbf{u}\cdot\mathbf{B})\right)\right] = 0 \tag{2.24}$$

For a shock in the target of an SZP implosion, $\mathbf{u} = (u_x, 0, 0)$ and $\mathbf{B} = (0, B_y, B_z)$, (recall $(r, z, \theta) \to (x, y, z)$), which gives the following

$$(u_x B_y)_2 = (u_x B_y)_1, \tag{2.25}$$

$$(u_x B_z)_2 = (u_x B_z)_1, \tag{2.26}$$

$$(\rho u_x)_2 = (\rho u_x)_1, \tag{2.27}$$

$$\left(p + \rho u_x^2 + \frac{B_y^2 + B_z^2}{2\mu_0}\right)_2 = \left(p + \rho u_x^2 + \frac{B_y^2 + B_z^2}{2\mu_0}\right)_1, \tag{2.28}$$

$$\left[u_x\left(\frac{\gamma}{\gamma-1}p + \frac{\rho u^2}{2}\right) + \frac{1}{\mu_0}\left(u_x(B_y^2 + B_z^2)\right)\right]_2 = \left[u_x\left(\frac{\gamma}{\gamma-1}p + \frac{\rho u^2}{2}\right) + \frac{1}{\mu_0}\left(u_x(B_y^2 + B_z^2)\right)\right]_1 \tag{2.29}$$

where the subscripts 1 and 2 refer to the pre- and post-shock quantities, respectively. How these relations are solved depends on which 5 of the 10 variables are unknown. In the standard presentation of the relations, it is assumed that the pre-shock quantities are known and the post-shock quantities are unknown.

Taking

$$\frac{\rho_2}{\rho_1} = \frac{u_{x1}}{u_{x2}} = \frac{B_{y2}}{B_{y1}} = \frac{B_{z2}}{B_{z1}} \equiv X, \tag{2.30}$$

Eqs. [2.25-2.27] are eliminated and the momentum and energy equations become

$$p_2 = p_1 + \left(1 - \frac{1}{X}\right)\rho_1 u_{x1}^2 + \frac{1-X^2}{2\mu_0}(B_{y1}^2 + B_{z1}^2), \tag{2.31}$$

$$2(2-\gamma)P_{B1}X^2 + (2\gamma(p_1 + P_{B1}) + (\gamma-1)\rho_1 u_{x1}^2)X - (\gamma+1)\rho_1 u_{x1}^2 = 0 \tag{2.32}$$

where $P_{B1} \equiv (B_{y1}^2 + B_{z1}^2)/2\mu_0$. If $P_B = 0$, this becomes

$$X = \frac{(\gamma+1)\rho_1 u_{x1}^2}{2\gamma(p_1) + (\gamma-1)\rho_1 u_{x1}^2} \tag{2.33}$$

which in the strong shock limit, $p_2 \sim \rho_1 u_{x1}^2 \gg p_1$, gives the familiar result $X = (\gamma+1)/(\gamma-1)$ used for the slug model in the previous section. If $P_B > 0$, this gives

$$X = \frac{1}{4(2-\gamma)P_{B1}}\Big[-(2\gamma(p_1 + P_{B1}) + (\gamma-1)\rho_1 u_{x1}^2) + \big[(2\gamma(p_1 + P_{B1}) + (\gamma-1)\rho_1 u_{x1}^2)^2 + 8(2-\gamma)P_{B1}(\gamma+1)\rho_1 u_{x1}^2\big]^{1/2}\Big] \tag{2.34}$$

where the positive sign is taken to give $X > 0$. In the limit $p_1 \to 0$,

$$X = \frac{-2\gamma - (\gamma-1)Y + \big[(2\gamma + (\gamma-1)Y)^2 + 8(2-\gamma)(\gamma+1)Y\big]^{1/2}}{4(2-\gamma)} \tag{2.35}$$

where $Y = \rho_{u1}^2/P_{B1}$. In the limit of large Y, it can be shown again that $X \to (\gamma+1)/(\gamma-1)$. Therefore a shock propagating perpendicular to the magnetic field behaves much like a purely hydrodynamic shock, in that the density (and magnetic field) cannot increase by more than a factor of $\gamma+1/\gamma-1$.

As with the analytical models for a Z-pinch implosion, the Rankine-Hugoniot conditions

derived in the previous section are useful insofar as the simplifications made in developing them are reasonably accurate. It is well-known (e.g [80, 81]), for example, that ion and electron temperature profiles are not identical across a shock front, because electrons are significantly more conductive. However, at a certain distance ahead and behind the shock front, the temperature profiles relax to the appropriate values as dictated by the jump conditions. The width of this "relaxation layer" [81] depends on the electron-ion equilibration timescale. While analytical approximations of this behavior are certainly possible, it is far more useful to numerically solve the appropriate equations in simulations.

2.4 Linear MRT instability growth

The Rayleigh-Taylor instability [55, 56] can develop when a heavier fluid is accelerated by a lighter fluid. When the vacuum magnetic field acts as the lighter fluid, it is called the magneto-Rayleigh-Taylor instability. It is customary to assume the fluid is incompressible and use ideal MHD (e.g. [3, 58, 59, 82, 83]) to achieve an analytical solution:

$$\nabla \cdot \mathbf{v} = 0, \tag{2.36}$$

$$\frac{\partial \rho}{\partial t} + \nabla \cdot (\rho \mathbf{v}) = 0, \tag{2.37}$$

$$\rho \left(\frac{\partial}{\partial t} + \mathbf{v} \cdot \nabla \right) \mathbf{v} = -\nabla \left(p + \frac{B^2}{2\mu_0} \right) + \frac{(\mathbf{B} \cdot \nabla)\mathbf{B}}{\mu_0} - \rho g \hat{x}, \tag{2.38}$$

$$\frac{\partial \mathbf{B}}{\partial t} = \nabla \times (\mathbf{v} \times \mathbf{B}) \tag{2.39}$$

We will consider the problem in planar geometry, so the density, pressure, velocity, and magnetic field are linearized as

$$(\rho, p, \mathbf{v}, \mathbf{B}) = (\rho, p, \mathbf{v}, \mathbf{B})_0(x) + (\rho, p, \mathbf{v}, \mathbf{B})_1(x) e^{i(k_y y + k_z z + \omega t)}. \tag{2.40}$$

The stability is considered in the reference frame of the plasma, i.e. $\mathbf{v}_0 = 0$, and it is assumed $\mathbf{B}_0 = B_{0y}(x)\hat{y} + B_{0z}(x)\hat{z}$, so the momentum equation gives

$$g = -\frac{1}{\rho_0}\frac{\partial}{\partial x}\left(p_0 + \frac{B_0^2}{2\mu_0}\right) \tag{2.41}$$

Introducing the perturbation displacement $\boldsymbol{\xi}_1$ and noting $\partial/\partial t \to i\omega,\ \partial/\partial y \to ik_y,\ \partial/\partial z \to ik_z$, the linearized momentum equations are

$$-\rho_0\omega^2\xi_{1x} = -\frac{\partial}{\partial x}\left(p_1 + \frac{\mathbf{B}_0\cdot\mathbf{B}_1}{\mu_0}\right) + \frac{i(k_yB_{0y} + k_zB_{0z})B_{1x}}{\mu_0} - \rho_1 g \tag{2.42}$$

$$-\rho_0\omega^2\xi_{1y} = -ik_y\left(p_1 + \frac{\mathbf{B}_0\cdot\mathbf{B}_1}{\mu_0}\right) + \frac{i(k_yB_{0y} + k_zB_{0z})B_{1y} + B_{1x}\frac{\partial B_{0y}}{\partial x}}{\mu_0} \tag{2.43}$$

$$-\rho_0\omega^2\xi_{1z} = -ik_z\left(p_1 + \frac{\mathbf{B}_0\cdot\mathbf{B}_1}{\mu_0}\right) + \frac{i(k_yB_{0y} + k_zB_{0z})B_{1z} + B_{1x}\frac{\partial B_{0z}}{\partial x}}{\mu_0} \tag{2.44}$$

Adding Eq. [2.43] $\times ik_y$ and Eq. [2.44] $\times ik_z$ gives, using $\nabla\cdot\mathbf{v} = i\omega\nabla\cdot\boldsymbol{\xi} = 0$,

$$-\rho_0\omega^2(ik_y\xi_{1y} + ik_z\xi_{1z}) = \rho_0\omega^2\frac{\partial\xi_{1x}}{\partial x} = (k_y^2 + k_z^2)\left(p_1 + \frac{\mathbf{B}_0\cdot\mathbf{B}_1}{\mu_0}\right) + \frac{-i(\frac{\partial B_{1x}}{\partial x})(k_yB_{0y} + k_zB_{0z}) + iB_{1x}\frac{\partial k_yB_{0y} + k_zB_{0z}}{\partial x}}{\mu_0} \tag{2.45}$$

This can be solved for $p_1 + (\mathbf{B}_0 + \mathbf{B}_1)/\mu_0$ and substituted into Eq. [2.42]:

$$k_y^2 + k_z^2\left(-\rho_0\omega^2\xi_{1x} + \rho_1 g - \frac{i(k_yB_{0y} + k_zB_{0z})B_{1x}}{\mu_0}\right) = -\frac{\partial}{\partial x}\left(\rho_0\omega^2\frac{\partial\xi_{1x}}{\partial x} - \frac{-i(\frac{\partial B_{1x}}{\partial x})(k_yB_{0y} + k_zB_{0z}) + iB_{1x}\frac{\partial k_yB_{0y} + k_zB_{0z}}{\partial x}}{\mu_0}\right) \tag{2.46}$$

B_{1x} is obtained from the magnetic field equation,

$$i\omega B_{1x} = [\nabla\times(\mathbf{v}_1\times\mathbf{B}_0)]_x = -\omega(k_yB_{0y} + k_zB_{0z})\xi_{1x} \tag{2.47}$$

to give

$$k^2\xi_{1x}\left(-\rho_0\omega^2 - g\frac{\partial\rho_0}{\partial x} + \frac{(\mathbf{k}\cdot\mathbf{B}_0)^2}{\mu_0}\right) = \frac{\partial}{\partial x}\left(\left[-\rho_0\omega^2 + \frac{(\mathbf{k}\cdot\mathbf{B}_0)^2}{\mu_0}\right]\frac{\partial\xi_{1x}}{\partial x}\right) \tag{2.48}$$

where $k^2 = k_y^2 + k_z^2$ and $\mathbf{k}\cdot\mathbf{B}_0 = k_y B_{0y} + k_z B_{0z}$, and from continuity, $i\omega\rho_1 = -i\omega\xi_{1x}\frac{\partial\rho_0}{\partial x}$.

Consider an imploding shell ("liner") of thickness $2a$, where the displacement is ξ^+ and ξ^- at $x = a, -a$, respectively. Inside the shell, let $\mathbf{B}_0 = \mathbf{B}_{0l}$, $\rho_{0l} = \rho$, on the outer surface, let $\mathbf{B}_0 = \mathbf{B}_{0v}, \rho_0 = 0$, and on the inner surface, let $\mathbf{B}_0 = 0, \rho_0 = 0$. This is essentially a specific case of the general MRT feedthrough problem considered by Weis [83]. Because $\partial\rho/\partial x = 0$ except at the interfaces, Eq. [2.48] reduces to $k^2\xi = d^2\xi/dx^2$, which has the piecewise solution

$$\xi(x) = \begin{cases} \xi^+ e^{-k(x-a)} & x > a \\ A_2 e^{kx} + B_2 e^{-kx} & -a < x \le a \\ \xi^- e^{k(x+a)} & x \le -a \end{cases} \tag{2.49}$$

where the boundary conditions are $\xi = 0$ at $\pm\infty$ and ξ^+, ξ^- at the interfaces, and $A_2 = (\xi^- e^{-ka} - \xi^+ e^{ka})/(e^{-2ka} - e^{2ka})$, $B_2 = (\xi^+ e^{-ka} - \xi^- e^{ka})/(e^{-2ka} - e^{2ka})$. Integration of Eq. [2.48] across the interface at $x = a$ and rearranging gives

$$\xi^+\left(gk\rho_0 + \left[-\rho_0\omega^2 + \frac{(\mathbf{k}\cdot\mathbf{B}_{0l})^2}{\mu_0}\right]\coth(2ka)\right) = \xi^-\left(\left[-\rho_0\omega^2 + \frac{(\mathbf{k}\cdot\mathbf{B}_{0l})^2}{\mu_0}\right]\operatorname{csch}(2ka)\right) \tag{2.50}$$

and at $x = -a$,

$$\xi^-\left(-gk\rho_0 + \frac{(\mathbf{k}\cdot\mathbf{B}_{0v})^2}{\mu_0} + \left[-\rho_0\omega^2 + \frac{(\mathbf{k}\cdot\mathbf{B}_{0l})^2}{\mu_0}\right]\coth(2ka)\right) = \xi^+\left(\left[-\rho_0\omega^2 + \frac{(\mathbf{k}\cdot\mathbf{B}_{0l})^2}{\mu_0}\right]\operatorname{csch}(2ka)\right) \tag{2.51}$$

The ratio ξ^+/ξ^- must be equal in both equations, and after some rearranging, this yields

$$\omega^4 + \left(-2\frac{(\mathbf{k}\cdot\mathbf{B}_{0l})^2}{\mu_0\rho_0} - \frac{(\mathbf{k}\cdot\mathbf{B}_{0v})^2}{\mu_0\rho_0}\coth(2ka)\right)\omega^2 - (gk)^2 + gk\frac{(\mathbf{k}\cdot\mathbf{B}_{0v})^2}{\mu_0\rho_0} + \frac{(\mathbf{k}\cdot\mathbf{B}_{0v})^2}{\mu_0\rho_0}\frac{(\mathbf{k}\cdot\mathbf{B}_{0l})^2}{\mu_0\rho_0}\coth(2ka) + \left[\frac{(\mathbf{k}\cdot\mathbf{B}_{0l})^2}{\mu_0\rho_0}\right]^2 = 0 \quad (2.52)$$

which has the solution

$$\omega^2 = \left(\frac{(\mathbf{k}\cdot\mathbf{B}_{0l})^2}{\mu_0\rho_0} + \frac{(\mathbf{k}\cdot\mathbf{B}_{0v})^2}{2\mu_0\rho_0}\coth(2ka)\right) \pm \left(\left[\frac{(\mathbf{k}\cdot\mathbf{B}_{0v})^2}{2\mu_0\rho_0}\coth(2ka)\right]^2 + (gk)^2 - gk\frac{(\mathbf{k}\cdot\mathbf{B}_{0v})^2}{\mu_0\rho_0}\right)^{1/2} \quad (2.53)$$

If we take $\mathbf{B}_{0l} = 0$, as in Appendix B4 of Weis [83], take $\mathbf{B}_{0v} = B_{0v}\hat{z}$, and make the substitution $B_{0v}^2 = 4\mu_0\rho_0 ag$ (such that $(\mathbf{k}\cdot\mathbf{B}_{0v})^2/\mu_0\rho_0 = 4k_z^2 ag$) , then the solution of Harris [59] is recovered. Unstable modes are present if $\omega^2 < 0$, which is the case if

$$\left[(gk)^2 - gk\frac{(\mathbf{k}\cdot\mathbf{B}_{0v})^2}{\mu_0\rho_0}\right]^{1/2} \gtrsim \frac{(\mathbf{k}\cdot\mathbf{B}_{0l})^2}{\mu_0\rho_0} \quad (2.54)$$

If an unstable mode does exist, its growth is mitigated when $(\mathbf{k}\cdot\mathbf{B}_{0v})$ and/or $(\mathbf{k}\cdot\mathbf{B}_{0l}) > 0$, though the mitigation is obviously greater for short wavelength perturbations. This is one of the motivations for seeding a Z-pinch implosion with an axial magnetic field.

The problem has been considered in cylindrical geometry (e.g. [59, 84]), but for our purposes - generally as an estimate for the required B_{z0} to mitigate MRT - it is sufficient to consider the problem in planar geometry.

2.5 Mitigation from non-ideal effects

It is difficult to treat MRT growth in a resistive plasma analytically, but it is known that effects due to plasma resistivity have a tendency to smooth out perturbations (e.g. [3, 4]). The theoretical argument originates from Hussey [38], which is summarized as follows. The *e*-folding time for a particular mode is defined as

$$t_{ef} = \left(\frac{\lambda + \lambda_{dg}}{2\pi g} \right)^{1/2} \tag{2.55}$$

where λ is the unstable wavelength, and λ_{dg} is a gradient scale length. Hussey argues that, in order for a unstable mode to grow, the magnetic diffusion time across one half-wavelength of an unstable mode must be larger than the *e*-folding time of the instability. The magnetic field diffusion time is estimated from

$$\frac{\partial \mathbf{B}}{\partial t} = -\nabla \times (\eta \frac{1}{\mu_0} (\nabla \times \mathbf{B})) = \frac{\eta}{\mu_0} \nabla^2 \mathbf{B} \rightarrow \Delta t \approx \frac{\mu_0 \lambda^2}{4\eta} \tag{2.56}$$

where the diffusion scale length is set to $\lambda/2$. The density gradient is typically on the order of 1-2 times the wavelength that grows initially, therefore

$$t_{ef} = \left(\frac{f\lambda}{2\pi g} \right)^{1/2} \tag{2.57}$$

Setting Eqs. [2.56-2.57] equal provides a minimum allowed wavelength,

$$\lambda_{min} = \left(\frac{8 f \eta^2}{\pi g \mu_0^2} \right)^{1/3} \tag{2.58}$$

It would therefore be expected, absent large difference in liner thickness (and assuming a plasma liner so that the electro-thermal instability is not present), shorter-wavelength modes present in lower-Z_A, less resistive liner implosions might be smeared out in higher-Z_A, more resistive

implosions. There is some qualitative evidence to support this observation in the next chapter.

2.6 Planar Korteweg-de Vries-Burgers equation for magnetoacoustic waves

Consider a perturbed plasma in planar geometry with constant density, temperature, velocity, and magnetic field. By linearizing the MHD equations, two classes of waves are found: Alfvén waves, which carry magnetic field perturbations along field lines with the group velocity $\mathbf{v}_A \equiv \mathbf{B}_0/(\mu_0\rho_0)^{1/2}$, and magnetosonic (magnetoacoustic) waves, which carry density and magnetic field perturbations perpendicular to the ambient magnetic field lines. We are generally interested in the fast magnetosonic wave, which propagates with the group velocity $v_0 = \left(v_A^2 + c_{S0}^2\right)^{1/2}$, where c_{S0} is the ambient sound speed.

In the linear approximation of such a wave, all points on the wave travel at the velocity v_0. However, the velocity of a point on a running wave is actually $v_0 + u$, where u is the velocity of the fluid. If u varies in the direction of wave propagation, the profile will continue to steepen until offset by dissipative processes. If the amplitude of the wave is large enough, a shock can develop [80].

Numerical simulations of SZP implosions [41] have suggested that azimuthal magnetic field is carried from the outer surface of the liner to the inner surface on timescales faster than the classical magnetic diffusion timescale (Eq. [2.56] with liner width replacing $\lambda/2$), hence the authors proposed that the field accumulation on the inner surface is due to another cause - magnetosonic waves propagating from the outer surface. The magnetic field carried with the wave is unable to propagate into the highly conductive target, resulting in the gradual accumulation of field at the interface. As magnetosonic waves carry density perturbations along with the magnetic field, the presence of such a phenomena would result in mass accumulation at the interface, which does not appear to be the case in [41].

Nevertheless, the notion of a traveling magnetosonic wave developing into a shock prompted the derivation of a Korteweg-de Vries-Burgers (KdVB) equation for magnetosonic waves. The KdVB equation [85] describes the solution for wave propagation that accounts for both dispersion and dissipation,

$$\frac{\partial n}{\partial t} + Q_A n \frac{\partial n}{\partial x} - Q_B \frac{\partial^2 n}{\partial x^2} + Q_C \frac{\partial^3 n}{\partial x^3} = 0 \tag{2.59}$$

where Q_B and Q_C are coefficients related to dissipation and dispersion, respectively, and n is the perturbed quantity. In [86], it was found that for a typical SZP implosion, $Q_C \ll 1$, so here we will neglect dispersion. The solution is obtained in planar geometry, though the problem has been solved for other plasmas in cylindrical geometry (e.g. [87]), albeit with significantly more effort.

First, consider the planar MHD equations, Eq. [2.37-2.39] and energy conservation, treating all quantities as functions of x and taking $\mathbf{v} = v(x)\hat{x}$, $\mathbf{B} = B(x)\hat{y}$, and $\mathbf{J} = J(x)\hat{z}$,

$$\frac{\partial \rho}{\partial t} + \frac{\partial}{\partial x}(\rho v) = 0, \tag{2.60}$$

$$\rho \frac{\partial v}{\partial t} + \rho v \frac{\partial v}{\partial x} = -\frac{\partial}{\partial x}\left(p + \frac{B^2}{2\mu_0}\right), \tag{2.61}$$

$$\rho \left(\frac{\partial}{\partial t} + v\frac{\partial}{\partial x}\right)\frac{T}{m_i} = -p\frac{\partial v}{\partial x} + \frac{\eta}{\mu_0^2}\left(\frac{\partial B}{\partial x}\right)^2 + \frac{\partial}{\partial x}\left(\kappa \frac{\partial T}{\partial x}\right), \tag{2.62}$$

$$\frac{\partial B}{\partial t} = -\frac{\partial}{\partial x}(vB) + \frac{\eta}{\mu_0}\frac{\partial^2 B}{\partial x^2} \tag{2.63}$$

where the specific internal energy is written T/m_i, $T = T_i + T_e$. Rather than linearize the equations, the approach to obtain Eq. [2.59] is to first nondimensionalize the above equations with the substitutions, $\rho = \rho_0 \rho_*$, $v = v_A v_*$, $B = B_0 B_*$, $T = T_0 T_*$, $t = x_0 t_*/v_A$, $x = x_0 x_*$:

$$\frac{\partial \rho_*}{\partial t_*} + \rho_* \frac{\partial v_*}{\partial x_*} + v_* \frac{\partial \rho_*}{\partial x_*} = 0, \tag{2.64}$$

$$\rho_* \left(\frac{\partial v_*}{\partial t_*} + v_* \frac{\partial v_*}{\partial x_*} \right) = \frac{-\beta_*}{2} \left(\rho_* \frac{\partial T_*}{\partial x_*} + T_* \frac{\partial \rho_*}{\partial x_*} \right) - B_* \frac{\partial B_*}{\partial x_*}, \tag{2.65}$$

$$\rho_* \left(\frac{\partial T_*}{\partial t_*} + v_* \frac{\partial T_*}{\partial x_*} + T_* \frac{\partial v_*}{\partial x_*} \right) = \frac{2\eta_*}{\beta_*} \left(\frac{\partial B_*}{\partial x_*} \right)^2 + \frac{2\kappa_*}{\beta_*} \frac{\partial^2 T_*}{\partial x_*^2}, \tag{2.66}$$

$$\rho_* \left(\frac{\partial B_*}{\partial t_*} + v_* \frac{\partial B_*}{\partial x_*} + B_* \frac{\partial v_*}{\partial v_*} \right) = \rho_* \eta_* \frac{\partial^2 B_*}{,} \partial x_*^2 \tag{2.67}$$

where $\beta_* \equiv \frac{T_0 \rho_0 / m_i}{B_0^2 / 2\mu_0}$ is the ratio of plasma pressure to magnetic pressure, $\eta_* = \frac{\eta}{\mu_0 v_A x_0}$ is the inverse Lundquist number with length scale x_0, $\kappa_* = \frac{\kappa T_0}{\rho_0 v_a^3 x_0}$is a quantity describing the ratio of energy transport by heat conduction relative to magnetic advection, $T_0 = k(T_i + T_e)$, and the transport coefficients η and κ are taken as constant. To be consistent with the derivations presented in [86, 88], the magnetic diffusion equation has been multiplied by ρ_*.

The reductive perturbation method [89, 90] has been used extensively in obtaining equations describing nonlinear wave evolution. In this method, the spatial and temporal coordinates (x_*, t_*) are transformed to stretched coordinates (ξ, τ),

$$\xi = -\varepsilon^\alpha (x_* + v_0 t_*), \tau = \varepsilon^{\alpha+1} t_*,$$

such that the spatial and temporal derivatives are (for $\alpha = 1$)

$$\frac{\partial}{\partial t_*} \to -\varepsilon v_0 \frac{\partial}{\partial \xi} + \varepsilon^2 \frac{\partial}{\partial \tau}, \; \frac{\partial}{\partial x_*} \to -\varepsilon \frac{\partial}{\partial \xi}.$$

v_0 is a constant to be determined later, and ε is a smallness parameter. The nondimensional

quantities are expanded in a power series in epsilon,

$$\rho_* = 1 + \varepsilon\rho_1 + \varepsilon^2\rho_2 + \varepsilon^3\rho_3 + \ldots,$$
$$v_* = \varepsilon v_1 + \varepsilon^2 v_2 + \varepsilon^3 v_3 + \ldots,$$
$$B_* = 1 + \varepsilon B_1 + \varepsilon^2 B_2 + \varepsilon^3 B_3 + \ldots,$$
$$T_* = 1 + \varepsilon T_1 + \varepsilon^2 T_2 + \varepsilon^3 T_3 + \ldots,$$

Making these substitutions and transforming to the stretched coordinates, Eqns. [2.64-2.67] can be separated by powers of ε. For example, the first- and second-order continuity equations are

$$(\varepsilon): \; v_0\frac{\partial\rho_1}{\partial\xi} = -\frac{\partial v_1}{\partial\xi},$$
$$(\varepsilon^2): \; \frac{\partial\rho_1}{\partial\tau} - v_0\frac{\partial\rho_2}{\partial\xi} - v_1\frac{\partial\rho_1}{\partial\xi} - \frac{\partial v_2}{\partial\xi} - \rho_1\frac{\partial v_1}{\partial\xi} = 0$$

Noting that u_1, ρ_1, T_1, B_1 vanish as $\xi \to \infty$, the first order equations conveniently reduce to

$$\frac{-u_1}{v_0} = \rho_1 = T_1 = B_1, \tag{2.68}$$

where we find $v_0 = \sqrt{\beta_* + 1}$. The second-order equations can be written

$$\frac{\partial\rho_1}{\partial\tau} - v_0\frac{\partial\rho_2}{\partial\xi} + 2v_0\rho_1\frac{\partial\rho_1}{\partial\xi} - \frac{\partial v_2}{\partial\xi} = 0, \tag{2.69}$$
$$-v_0\frac{\partial\rho_1}{\partial\tau} - v_0\frac{\partial v_2}{\partial\xi} = \frac{\beta}{2}\left(\frac{\partial\rho_2}{\partial\xi} + \frac{\partial T_2}{\partial\xi}\right) + v_0^2\rho_1\frac{\partial\rho_1}{\partial\xi} + \frac{\partial B_2}{\partial\xi}, \tag{2.70}$$
$$\frac{\partial\rho}{\partial\tau} - v_0\frac{\partial T_2}{\partial\xi} = \frac{\partial v_2}{\partial\xi} - 2v_0\rho_1\frac{\partial\rho_1}{\partial\xi} + \frac{2\kappa_*}{\beta_*}\frac{\partial^2\rho_1}{\partial\xi^2}, \tag{2.71}$$
$$\frac{\partial\rho_1}{\partial\tau} - \frac{\partial u_2}{\partial\xi} + 2v_0\rho_1\frac{\partial\rho_1}{\partial\xi} - v_0\frac{\partial B_2}{\partial\xi} = \eta_*\frac{\partial^2\rho_1}{\partial\xi^2} \tag{2.72}$$

These can be combined into the evolution equation

$$\frac{\partial \rho_1}{\partial \tau} + \left(\frac{\sqrt{\beta_* + 1}}{2} + 1 \right) \rho_1 \frac{\partial \rho_1}{\partial \xi} - \frac{\kappa_* + \eta_*}{2(\beta_* + 1)} \frac{\partial^2 \rho_1}{\partial \xi^2} = 0 \tag{2.73}$$

For a third-order (dispersive) term to appear, one has to modify the original equations to include additional terms, e.g. see [86–88]. Eq. [2.73] is analytically solveable - one method of obtaining is a solution is the tanh method [91], where the ansatz

$$\rho_1(\xi, \tau) = A \tanh(k\xi - \omega\tau) + A \tag{2.74}$$

is used. This gives, after some rewriting,

$$\left[(AQ_A + 2Q_B k)kY + (\omega - AQ_A k) \right] (Y^2 - 1) = 0 \tag{2.75}$$

where $Y = \tanh(\omega\tau - k\xi)$, $Q_A = \frac{\sqrt{\beta_* + 1} + 2}{2}$, $Q_B = \frac{\kappa_* + \eta_*}{2(\beta_* + 1)}$. A non-trivial solution exists for Y if

$$k = \frac{-AQ_A}{2Q_B}, \ \omega = AQ_A k \tag{2.76}$$

The solution to Eq. [2.74] is a monotonic profile of amplitude $A/2$, width $2\pi/k$, and phase/group velocity AQ_A. Large values of k result in a highly-dissipative profile and no shock develops, whereas small values of k result in a shock-like solution. As noted in [86], the dominant term in Q_B depends very strongly on temperature ($\kappa_*/\eta_* \propto T_0^5/(\bar{Z}B_0 \ln\Lambda)^2$) - in hotter plasmas the nonlinearity is balanced by thermal dissipation, in colder plasmas the nonlinearity is balanced by resistive dissipation.

In later sections, we will discuss the value of k in the context of SZP.

2.7 Conclusion

The analyses presented in this section provide a summary of the relevant analyses one might perform in the context of a fluid description of a Z-pinch. The 0-D analytic snowplow and slug models provide estimates of implosion time as a function of load mass, and could provide approximate final conditions assuming a Bennett equilibrium. However, they are lossless and give us limited information on stability. In deriving the Rankine-Hugoniot relations for a planar MHD shock, it was found the jump conditions are similar to a hydrodynamic shock, with the magnetic field jump limited to the same value as the density jump, $\gamma+1/(\gamma-1)$. However, we have not included the effects of cylindrical convergence, differing electron and ion temperatures, or the effects due to radiation (which can increase shock strength). From linear MRT stability analysis, it was shown that the presence of an axial magnetic field in either the liner or vacuum can stabilize shorter wavelength modes. Similar, more detailed analyses have been extended to cylindrical geometry [59, 84], and three dimensions. However, these analyses assume ideal MHD, which has limited applicability to SZP. Estimates of instability mitigation by resistive "smoothing" of density gradients is made, but they are approximate. Finally, a Burgers's equation for planar magnetosonic waves is obtained, but deriving an analytical solution requires assuming uniformities in the plasma that are generally not true during a SZP implosion. The goal here is not to diminish the usefulness of the presented analyses, but rather to strongly motivate the simulations in the following chapters. It is simply not feasible to obtain a one-size-fits-all purely analytic model of a Z-pinch implosion without neglecting relevant physics. We thus turn to simulations.

2.8 Acknowledgments

§2.6, in part, includes material as it appears in "Investigation of magnetic flux transport and shock formation in a staged Z-pinch", J. Narkis, H. U. Rahman, F. J. Wessel, and F. N. Beg,

Phys. Plasmas **24**, 102514 (2017). J. Narkis was the primary author of this paper.

Chapter 3

Dynamics and MRTI growth of unmagnetized liner-on-target (SZP) implosions

3.1 Introduction

The analytic models presented in the previous chapter are useful for providing context and a preliminary understanding of the dynamics in a SZP implosion, but proper treatment requires modeling using non-ideal radiation-MHD simulations. This chapter will address shock heating and MRT instability in the context of gas-puff liner-on-target loads on a university-scale (1 MA, 100 ns) driver.

The work of [37, 41] has shown that the magnitude of azimuthal magnetic field at the interface between the liner and target of an SZP-like load can be a significant fraction or larger than the vacuum magnetic field. The target plasma is typically a low-Z_A material like hydrogen or deuterium, it will generally be much less resistive (much more conductive), which can lead to a large azimuthal magnetic field gradient and a corresponding axial current. This could provide

some degree of Ohmic (ηJ^2) preheating to the target, but for this heating to be relevant it would have to be comparable to or exceed the preheating by shock. The model presented in the following chapter quantifies the relative effects of Ohmic and shock heating, and concludes that the latter is significantly larger. Another effect to consider is that a $\mathbf{J} \times \mathbf{B}$ force will develop on the interface. If the magnitude of this force is large relative to the inertial compressive force by the liner, it could cause the target to detach and accelerate ahead of the liner. Finally, if the azimuthal magnetic field at the interface is large at peak compression, the Hall parameters could be large enough to inhibit thermal conduction, which would raise the peak temperature in regimes in which thermal conduction losses are dominant relative to radiation.

In 1-D simulations using the radiation-MHD code MACH2, it was found that, for SZP-like loads in which the interfacial $\mathbf{J} \times \mathbf{B}$ force affected target dynamics, that (a) the resistivity of the liner was the most significant predictor of the strength of the force, and that (b) there was significant discrepancies among resistivity tables for the same material within the SESAME libraries, and that these tables disagreed somewhat with Spitzer-Braginskii.

3.2 On the importance of resistivity

To obtain the magnetic field evolution equation in resistive MHD, Faraday's Law, Ampere's Law, and Ohm's law,

$$\nabla \times \mathbf{E} = -\frac{\partial \mathbf{B}}{\partial t}, \tag{3.1}$$

$$\nabla \times \mathbf{B} = \mu_0 \mathbf{J}, \tag{3.2}$$

$$\mathbf{E} = \bar{\bar{\eta}} \cdot \mathbf{J} + \mathbf{v} \times \mathbf{B}, \tag{3.3}$$

are combined to obtain

$$\frac{\partial \mathbf{B}}{\partial t} = -\nabla \times \left(\frac{\bar{\bar{\eta}}}{\mu_0} \cdot (\nabla \times \mathbf{B}) \right) - \nabla \times (\mathbf{v} \times \mathbf{B}) . \tag{3.4}$$

The $\mathbf{J} \times \mathbf{B}$ force at the interface can either develop by magnetic field advection with the flow, or by resistive diffusion. In addition, in a quiescent medium, a perturbation in density and magnetic field would propagate and could develop into a discontinuity according to the Burgers equation derived in §2.6. As discussed in that section, this is a challenging phenomenon to quantify in liner-on-target Z-pinches.

The magnetic Reynolds number, $Lu\mu_0/\eta$, describes the relative strengths of these terms, and if the characteristic velocity is taken as the Alfvén speed, $v_A = |B|/(\mu_0 \rho)^{1/2}$, then it is called the Lundquist number. In the early stages of a liner-on-target Z-pinch implosion, the resistivity can differ by several orders of magnitude depending on the density and material of the liner. If a solid liner is used, then the material is generally conductive enough that resistive effects can be neglected. However, this is not true for a gas-puff liner.

Consider, for the sake of argument, a stationary cylinder made of a resistive material. Neglecting any effects due to changing material properties, when an axial current is applied on the surface with rise time (quarter-period) τ, there is a characteristic distance called the skin depth over which the surface current attenuates by a factor of $1/e$,

$$\delta = \sqrt{\frac{2\eta}{\omega \mu_0}} = \sqrt{\frac{4\eta\tau}{\pi \mu_0}} \tag{3.5}$$

For a gas-puff liner of (initial) resistivity 10^{-4}-10^{-5} Ωm and a rise time of 100 ns, the skin depth is 1-3 mm. It would therefore be expected that an appreciable azimuthal magnetic field could diffuse through a liner if it were that approximate resistivity and width.

Initial MACH2 simulations of a gas-puff, liner-on-target implosion used a liner FWHM of approximately 1 mm. As will be discussed later, magnetic field diffusion was significant and the

magnitude of diffused field had a strong material dependence. As multiple resistivity models were available for the liner materials, before comparison among the different available liner materials, it was necessary to consider (a) whether the resistivity model affected the dynamics using a single material and (b) how to select the most accurate model if the effect is significant.

The material chosen for this study was argon, because at the time there were concurrent and upcoming SZP experiments that used an argon liner. The SESAME electrical conductivity tables available for Ar at the time were 25171 and 25174, both of which are from experimentally-obtained data. The floor values of these tables are 0.37 and 1 kg/m^3, respectively, or $n_i = 5.7 \times 10^{18}$ and 1.5×10^{19} cm^{-3}. Liner density for a gas-puff in this regime is $\sim 10^{18}$ at peak compression, so the resistivities were extrapolated such that the density dependence was neglected. As a first approximation, this would not introduce much error because the density dependence on resistivity only appears in the Coulomb logarithm. However, there is substantial discrepancy in the table values at temperatures below 100 eV, which is problematic because the liner plasma is relatively cold in the early stages of the implosion.

In order to resolve this discrepancy, category 3 SESAME tables were generated by M. P. Desjarlais at Sandia National Laboratories for argon using the latest and most accurate models available. It was found that, within the density and temperature regime of interest (1-100 eV, 10^{14}-10^{20} cm^{-3}), the Desjarlais tables (numbered 29171) agreed within a factor of two with the Spitzer model using ionization data from SESAME 19517 - a category 2 SESAME table with high resolution at lower temperatures (below 10 eV) and lower densities (the floor is 10^{-7} kg/m^3). These observations are summarized in Fig. 3.1, which shows the resistivities as functions of temperature at constant density for the following tables: SESAME 25171 at its floor density 0.376 kg/m^3, SESAME 25174 at its floor density 1 kg/m^3, SESAME 29171 at 0.1 (solid) and 0.001 (dashed) kg/m^3, and 0.5$\times$ Spitzer at 0.1 (solid) and 0.001 kg/m^3 (dashed), where $\bar{Z}$ (and therefore $\ln\Lambda$) is taken from SESAME 19517.

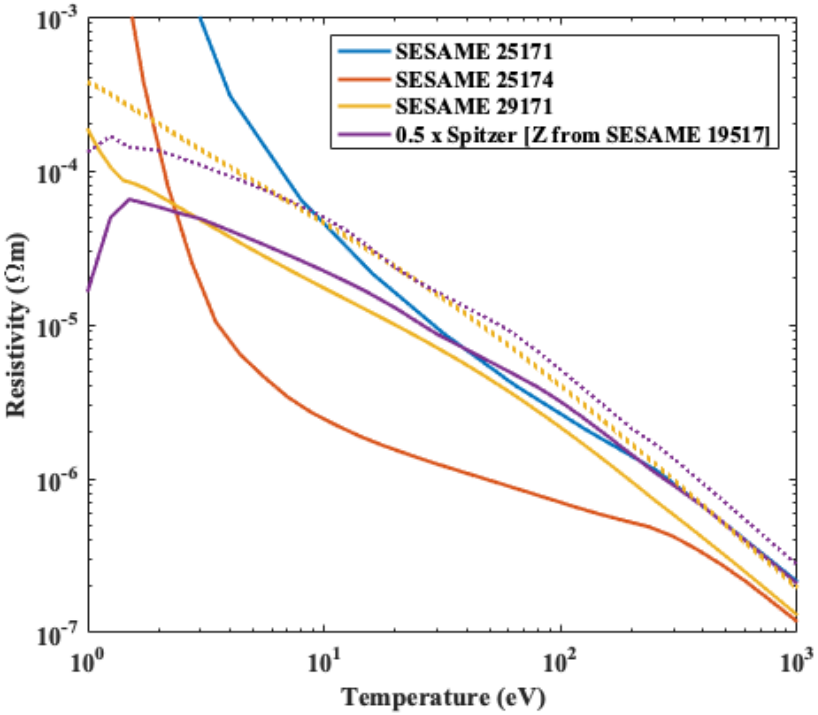

Figure 3.1: Electrical resistivities as functions of temperature at constant density for argon using several SESAME tables. SESAME 25171 and 25174 are actual SESAME tables available to the library, with floor values of 0.376 and 1 kg/m^3, respectively. SESAME 29171 is a table generated by M. P. Desjarlais at Sandia National Laboratories; densities are 0.1 (solid) and 0.001 kg/m^3 (dashed). The SESAME 29171 values are compared with 0.5$\times$ Spitzer resistivity, where $\bar{Z}$ is taken from SESAME 19517, a category 2 (opacity) table available in the standard SESAME libraries.

3.3 On the role of resistivity in shock formation for Ar/D

The previous section showed that the standard SESAME electrical resistivity tables for argon, 25171 and 25174 are in significant disagreement with one another, in addition to truncating at very high densities ($\sim 10^{18}$ cm^{-3}) relative to the typical range of densities expected on a university-scale gas-puff Z-pinch. To determine whether this could effect the dynamics, a test problem is constructed in MACH2, in which the only variable is the resistivity table. The initial conditions are as follows: the load is Ar liner onto D target with the density profile shown in Fig. 3.2, coupled to an RL-circuit of resistance 0.19 Ω and inductance 69 nH driven by the

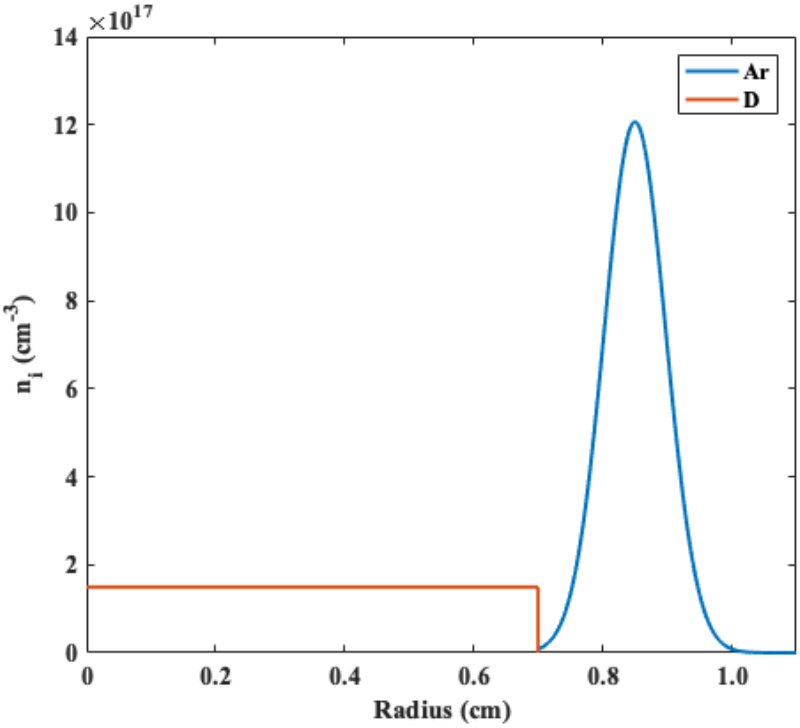

Figure 3.2: Initial density profiles for argon and deuterium for the argon resistivity test problem. The liner FWHM is approximately 1 mm.

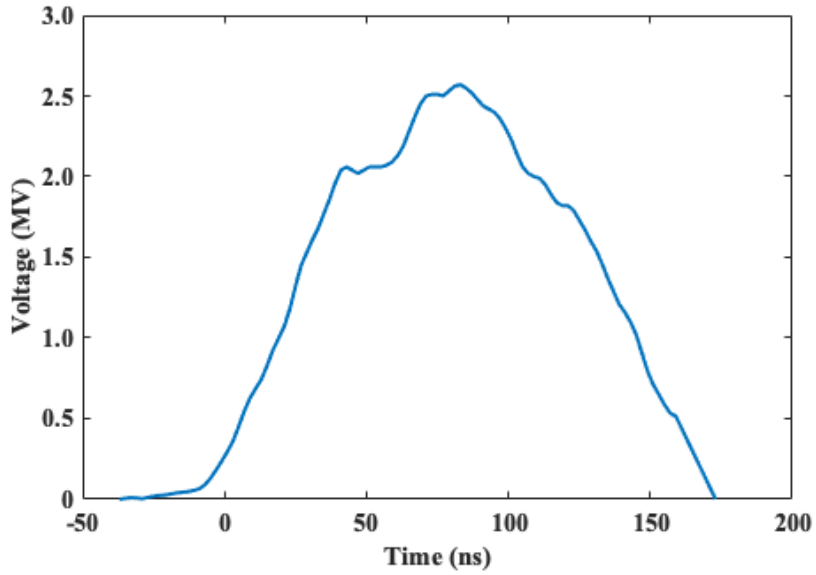

Figure 3.3: Approximate open-circuit voltage waveform for the Zebra driver. Approximately 1 MA is delivered to the load in 100 ns.

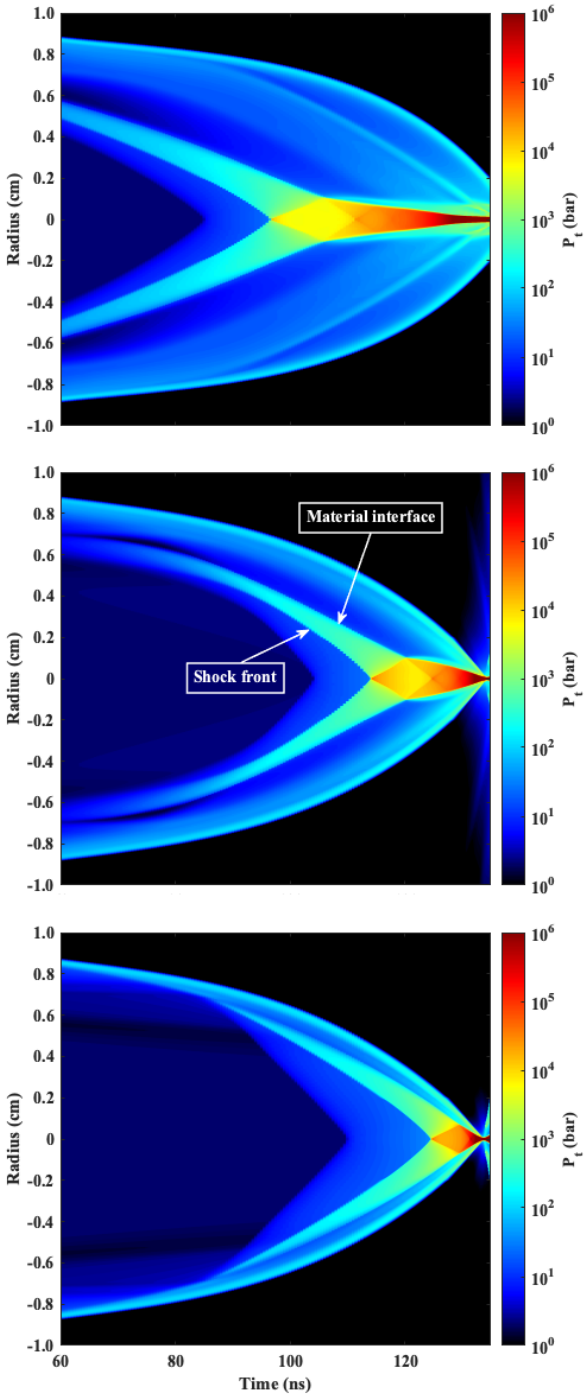

Figure 3.4: Plasma pressure as a function of radius and time for the argon resistivity test problem. All simulations are identically initialized Ar/D implosions, with the exception of different argon resistivity tables: SESAME 25171 (top), SESAME 29171 (middle, produced by Desjarlais for this study), and SESAME 25174 (bottom).

voltage waveform shown in Fig. 3.3. The simulation was Eulerian, with 10-μm radial resolution from 0 to 0.2 cm, and 50-μm radial resolution from 0.2 cm to 1.1 cm. Both the ion and electron temperatures were initialized to 3 eV to ensure some degree of ionization in both materials, and there was no axial premagnetization. The 'emission' radiation model was used, which assumes the entire load is optically thin and emits radiation as a black body at a volumetric cooling rate $P_{rad} = ac\rho\chi_{\text{planck}}T_e^4$, where a is Stefan's constant, c is the speed of light, ρ is density, T_e is electron temperature, and χ_{planck} is the Planck mean opacity [92]. For this simulation, argon opacities were obtained from Post and Jensen [93].

The trajectory of the interfaces between the target, liner, and vacuum, as well as the shock front, are readily visualized in streak-like images of total plasma pressure. It is challenging to compare such an image with an experimental image, because streak cameras capture emitted radiation over a certain energy range (e.g. optical). This is true particularly in the case of a high-Z gas-puff liner imploding onto a low-Z target, because the intensity of radiation emitted by the liner is orders of magnitude greater than that emitted by the target. However, they are still useful in interpreting simulation results.

For example, there is strong correlation between the resistivity table used and the time of shock formation, as shown in Fig. 3.4. At the initial temperature of 3 eV, Fig. 3.1 shows that the resistivities for Ar for tables 25171, 29171, and 25174 are 2.6×10^{-3}, 4.8×10^{-5}, and 2.0×10^{-5} Ωm, respectively. The corresponding skin depths are 16.2, 2.2, and 1.4 mm, respectively. All of these values, particularly for 25171, are larger than the initial liner FWHM, 1.1 mm, so significant magnetic field diffusion through the liner surface will occur.

There are two main consequences of this diffusion. First, if the magnetic pressure ($P_B = B^2/2\mu_0$) at the interface between the liner and target is larger than the corresponding ram pressure ($P_{ram} = \rho v^2$), then target compression and shock heating can be attributed to the diffused magnetic field. Second, if the diffused B_θ is large enough that the Hall parameters are much greater than one in the vicinity of the interface, then it becomes relevant to consider the possible

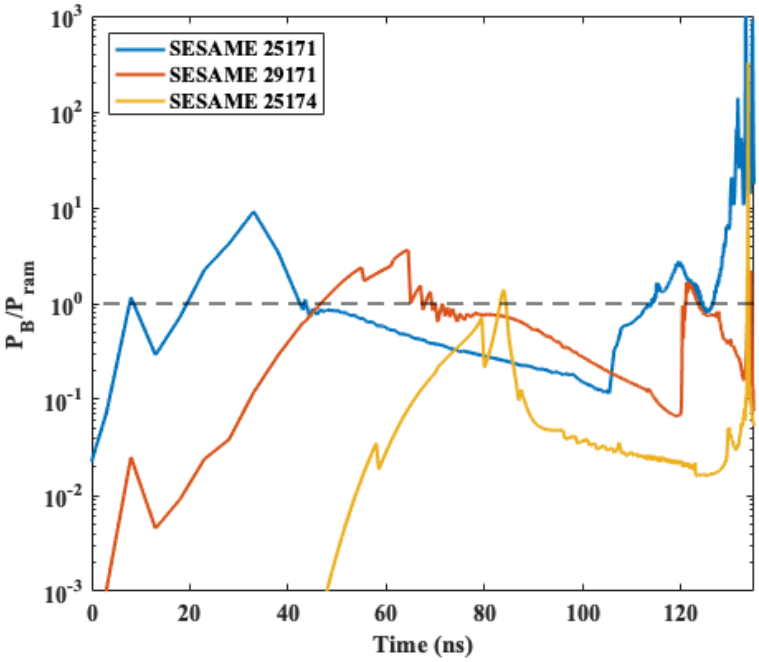

Figure 3.5: The ratio of magnetic to ram pressure at the liner/target interface as a function of time for the argon resistivity test problem. Because the simulations are Eulerian, here the interface is defined as outermost cell that is purely liner material.

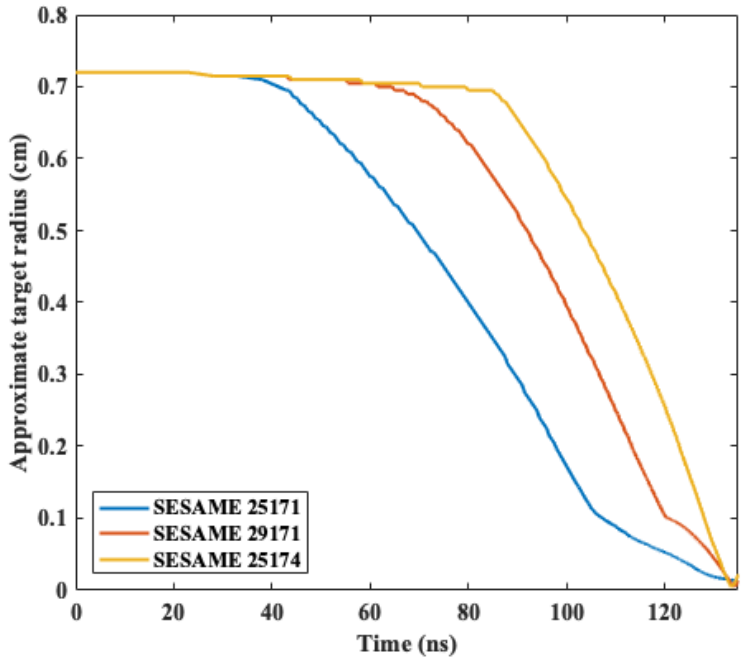

Figure 3.6: Target radius as a function of time for the argon resistivity test problem. Earlier onset of target compression correlates with higher liner resistivity.

relevant to consider the possible reduction in thermal conduction from the target to the liner.

These quantities are readily extractable from simulations, because multi-material MHD codes require a material specification parameter for each cell. For example, in MACH2, the parameter is called 'conimat'. It is standard for SZP simulations to use conimat=1 for the target material and conimat=2 for the liner material - and possibly 3 if there are two liner materials. The material interface between the liner and target is then defined as the radius at which the value for conimat increases from 1 to 2. In a Lagrangian simulation, there are no mixed cells, so the radius is explicitly defined at a single cell interface. In an Eulerian simulation, the boundary between materials is one to a few cells thick. Rather than a discontinuous jump, the material parameter will increase over the range of cells. This requires a mix model to determine the relative weight of each material and track the relevant physical quantities - for example, the radiation produced in a 10% Kr, 90% D cell - denoted in MACH2 by conimat=1.1, will be significantly different from the radiation produced in a cell that is 50% Kr, 50% D.

Consider first the relative strengths of liner ram and magnetic pressure on the target. Fig. 3.5 shows the ratio of P_B to P_{ram} on the right side of the interface, i.e. the innermost cell that is purely liner material, for tables 25171, 29171, and 25174. A comparison of these plots with the radius of this location with time, shown in Fig. 3.6 - essentially the radius of the target - shows that (a) P_B/P_{ram} is greater than unity just prior to target acceleration, and (b) the value drops below unity once the shock has been launched in the target. This suggests that, if a liner is highly resistive, P_B contributes to the initial acceleration of the target. However, regardless of liner resistivity, liner inertia will ultimate dominate and do more work on the target.

Second, consider the electron Hall parameter in the vicinity of the interface, $\omega_{ce}\tau_{ei}$, where $\omega_{ce} = eB/m_e$ is the electron cyclotron frequency, and τ_{ei} is the electron-ion collision time. To account for the different resistivities, and so that the Hall parameter can be estimated explicitly

from simulated quantities, an effective collision time is used, $\tau_{ei,eff} \equiv m_e/\eta n_e e^2$,

$$\omega_{ce}\tau_{ei} \approx \frac{|B|}{\eta \bar{Z} n_i e} \tag{3.6}$$

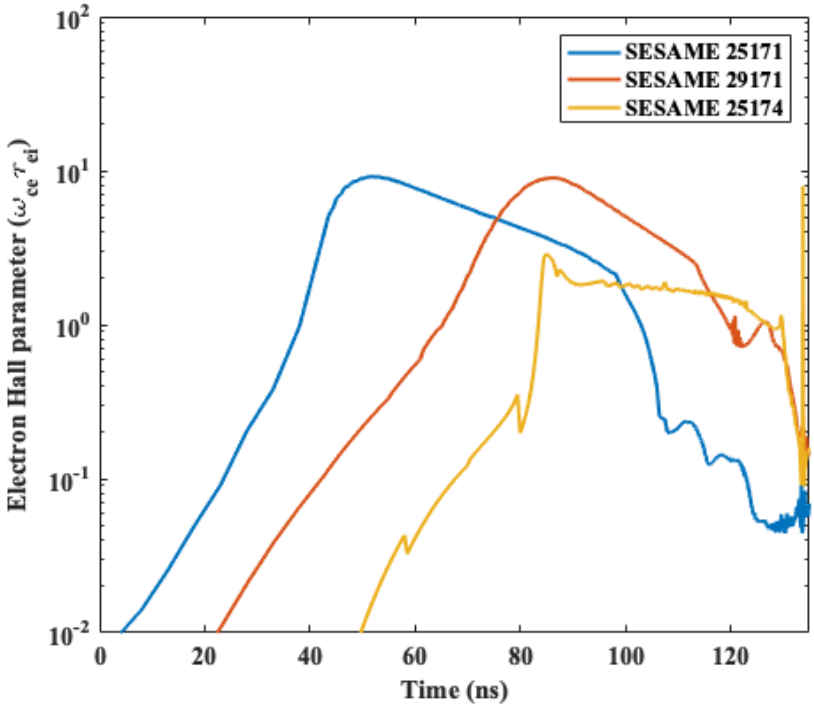

Figure 3.7: Electron hall parameter as a function of time for the argon resistivity test problem. Because the simulations are Eulerian, here the interface is defined as outermost cell that is purely liner material.

The reduction in thermal conductivity is approximately proportional to the square of the Hall parameter; an electron Hall parameter of 20 and 214 reduces thermal conductivity by approximately a factor of 100 and 10^4, respectively [39, 77]. Fig. 3.7 shows that, independent of resistivity model, the electron Hall parameter is within the range of 10^0-10^1 when the shock first forms, and that it drops to 10^{-1}-10^0 as the liner converges on axis. This would suggest that, for this particular liner-on-target configuration, thermal insulation by pure azimuthal magnetic field diffusion is negligible, and that this is largely independent of the resistivity model.

Finally, it is of interest to establish whether the resistivity model has an effect on shock

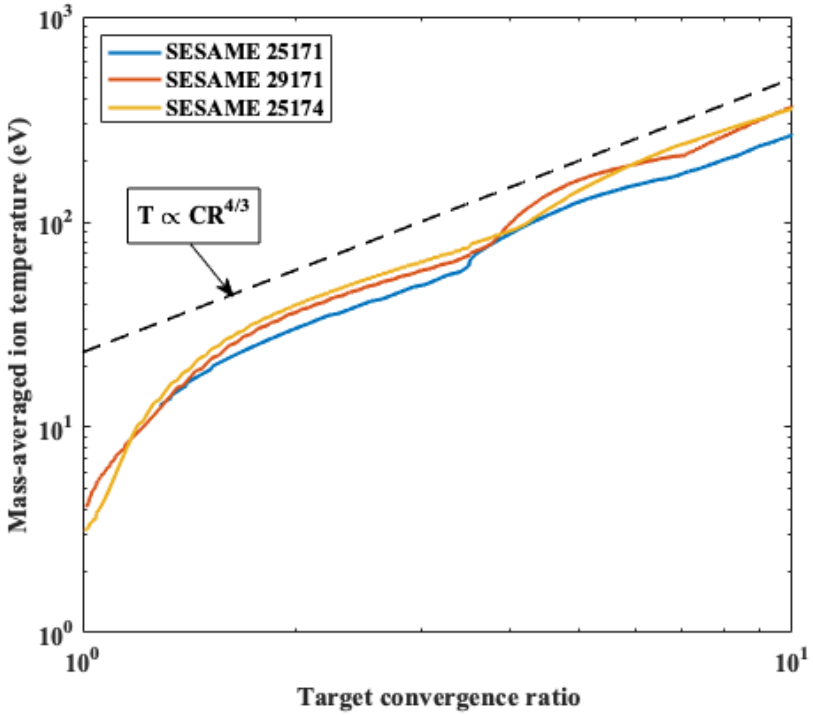

Figure 3.8: Mass-averaged ion temperature as a function of target convergence ratio for the argon resistivity test problem. The dashed line is for reference, representing the 4/3-power dependence of temperature on convergence ratio in purely adiabatic compression of a cylindrical, monatomic gas.

strength, or more practically, on the overall target heating. A time shift in the implosion of the target might suggest a difference in target heating. To consider this, the mass-averaged ion temperature is plotted as a function of target convergence ratio in Fig. 3.8 for the three resistivity models. In such plots, for an ideal monatomic gas in cylindrical geometry, temperature increases as $\mathrm{CR}^{4/3}$ if the implosion is purely adiabatic. Shock compression will heat the target faster than this rate, whereas thermal conduction and radiation losses can lower heating to below this rate. Although the target does compress by more than a factor of 10, shock heating terminates when the shock front arrives on axis, which occurs prior to $CR = 10$. It is clear from Fig. 3.6 that, while the shock launch time is affected by the choice of liner resistivity, there is not a significant effect between resistivity model and increased shock heating when the liner material is held constant.

The study presented in this section demonstrates a clear inadequacy in the standard

SESAME resistivity tables for argon, particularly in the regime of university-scale gas-puff Z-pinches. It was found that, in the range of a few-tens of eV, SESAME 25171 and SESAME 25174 resistivities disagree by orders of magnitude, and that this effect caused the target implosion time to shift by 60 ns, over half the current rise time. A similar discrepancy is found between the krypton SESAME tables 25181 and 25184, and xenon SESAME tables 25191 and 25194. Similar analyses could be done with those tables, but they are not presented here because it would be redundant.

3.4 On the role of liner material in shock formation

In the previous section, it was shown that in a liner-on-target, gas-puff implosion in which the liner width is comparable to its initial skin depth, an appreciable magnetic field can diffuse through the outer surface, and that in such a problem it is necessary to use accurate resistivity tables because material resistivity can significantly affect the timing of shock formation. In an identically-massed load, varying the liner material will affect the resistivity because both the ionization level and electron temperature will differ as a function of liner material. Furthermore, liner thickness can also vary depending on the material. While the effect of Z_A difference has been mentioned in the context of target heating in a SZP-like load (e.g. [41]), the liner material has not been explicitly studied as the only variable, particularly in gas-puffs. This motivated the work that lead to Narkis et al [53], which considered a gas-puff liner-on-target load on a university scale driver.

As in the previous section, this problem is of a gas-puff, liner-on-target implosion on a driver that delivers 1 MA in 100 ns, and it is simulated using the MHD code MACH2. Four liner materials are considered: Ne, Ar, Kr, and Xe. The physical models are identical, with two exceptions. First, the radiation model: the opacities in Post [93] are used for Ne and Ar, but for Kr and Xe the tables have floor values of 50 eV - which is higher than the liner temperature for much

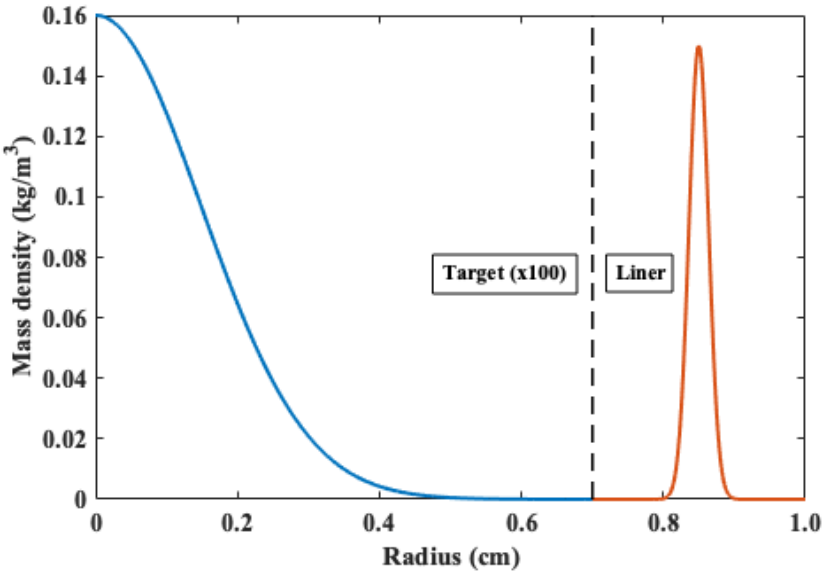

Figure 3.9: Initial density profile for single-liner SZP simulations on 1-MA driver. The liner FWHM is 650 μm.

of the implosion. To address this, PrOpacEOS opacity tables are used instead for those materials. The potential effects of radiation transport are included by solving the radiation diffusion equation with the appropriate flux limiter to account for the optical thinness of both the liner and target for the majority of the implosion. Second, in order to ensure consistency among the materials, ionization tables were obtained for each material from the same PrOpacEOS simulations that generated the opacity tables, and resistivity was calculated as 0.75$\times$ Spitzer calculated according to the values in the ionization table (except for Ar, for which 29171 was used).

The density profile has the form shown in Fig. 3.9, in which the peak number densities are 5×10^{17} cm^{-3} and 0.7-4.5 $\times 10^{18}$ cm^{-3} for the liner and target, respectively. The initial temperature is set to 3 eV to ensure adequate preionization, as before. The liner FWHM is 650 μm, which was chosen to allow significant magnetic field diffusion through the liner, but would be challenging to reproduce in experiment.

For direct comparison with the Ar resistivity problem, streak-like images of plasma pressure are shown in Fig. 3.10. A detailed discussion of the dynamics of shock formation may

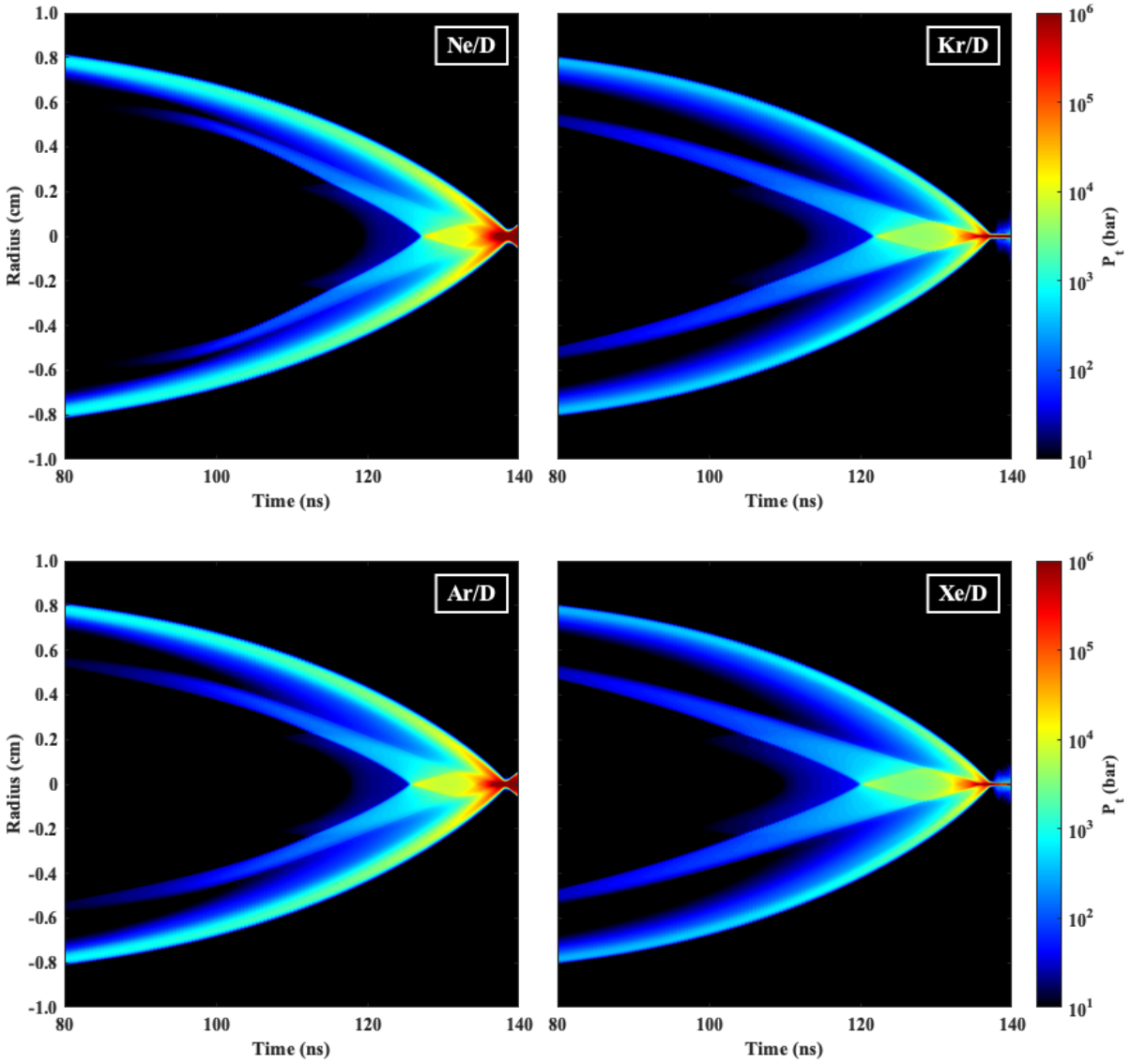

Figure 3.10: Plasma pressure as a function of radius and time for the different liner Z_A test problem. The initial conditions are identical, with the except of liner material: Ne (top, left), Ar (bottom, left), Kr (top, right), and Xe (bottom, right).

be found in [53]; here we note the observations relevant to the current discussion. Because the load mass is held constant, the trajectory of the liner radius is unchanged among the four cases. The lack of liner expansion after peak compression, colloquially referred to as "bounce", in the Kr/D and Xe/D simulations is actually a delay of a few ns. These simulations were performed on a purely Eulerian grid with resolution 50 μm. The liner overcompresses because these are

low-resolved, 1-D simulations - to the point that the target is less than one cell width. The load

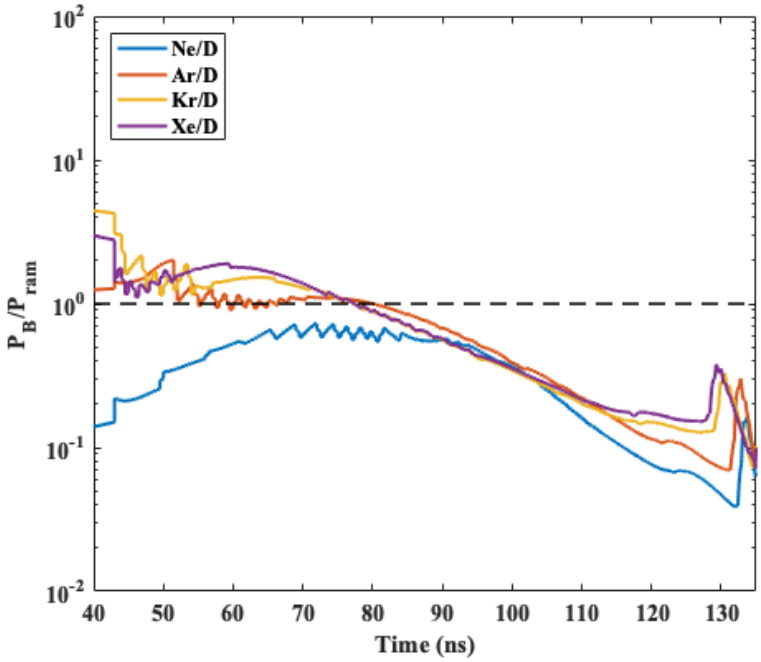

Figure 3.11: The ratio of ram to magnetic pressure at the liner/target interface as a function of time for the different liner Z_A test problem. Because the simulations are Eulerian, here the interface is defined as outermost cell that is purely liner material.

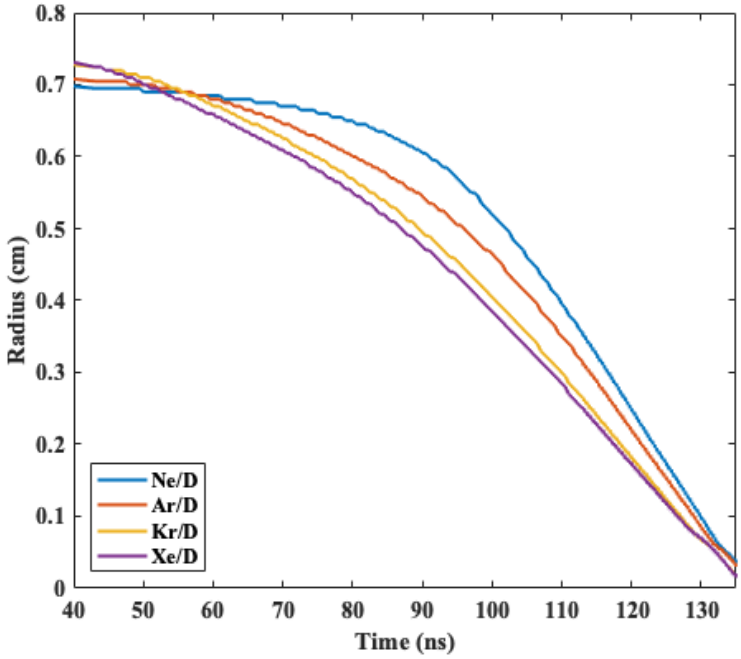

Figure 3.12: Target radius as a function of time for the different liner Z_A test problem. Onset on target compression is earlier in the more-resistive, higher-Z_A liners.

then undergoes radiative collapse, as the liner radiates significantly more than the target.

Analogous to the Ar resistivity problem, shock compression of the target is initiated earlier in time, correlating with greater azimuthal magnetic flux diffusion into the target. Compression of the target is initiated by magnetic forces in the cases of Ar, Kr, and Xe, whereas for the complete duration of the Ne test case, target compression is predominantly by liner inertia. This is shown in a comparison of Figs. 3.11 and 3.12, which show the ratio of ram to magnetic pressure and target radii, respectively, for the four test cases. Although target compression is initiated earlier for higher Z_A materials, Fig. 3.12 shows that target radii are comparable at 130 ns. While the change in liner material does affect when the shock is launched in the target, and whether it is launched by magnetic or inertial forces, the net effect on shock heating of the target is negligible. This is observed in Fig. 3.13, which shows the mass-averaged target ion temperature as a function of convergence ratio. Again, a reference line for adiabatic compression of a cylindrical, monatomic target, for which temperature scales as $\mathrm{CR}^{4/3}$, illustrates that shock heating is negligible beyond

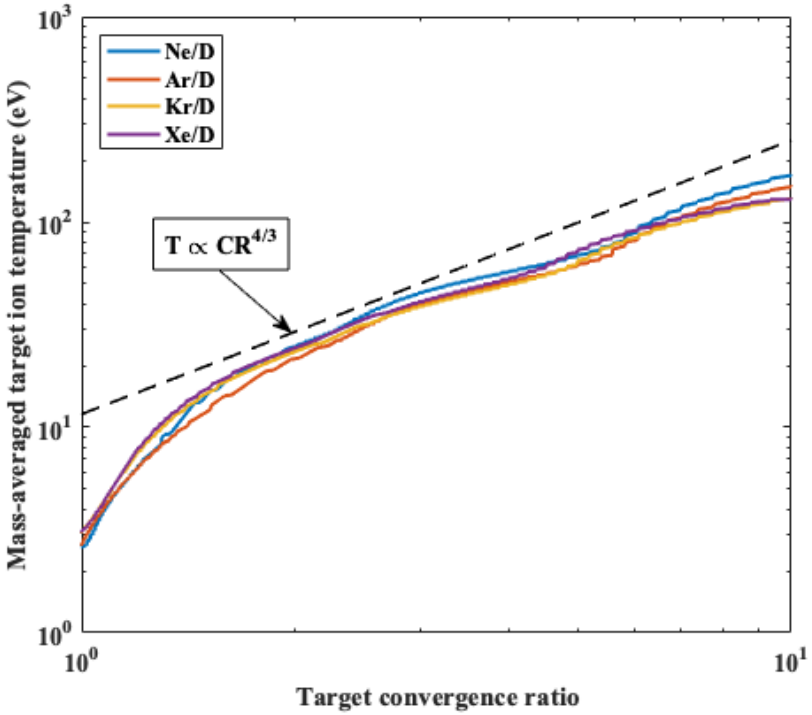

Figure 3.13: Mass-averaged ion temperature as a function of target convergence ratio for the different liner Z_A test problem. The dashed line is for reference, representing the 4/3-power dependence of temperature on convergence ratio in purely adiabatic compression of a cylindrical, monatomic gas.

CR of 2-3.

Although shock heating among the materials for the test problem is insigificant, the final temperatures achieved could be different if there is a correlation between magnetization of the liner, as estimated by the electron Hall parameter, and the liner material. This is considered in Fig. 3.14, which shows the electron Hall parameter at the interface between the liner and target as a function of time for the four test cases. Early in the implosion, a significant correlation is seen between $\omega_{ce}\tau_{ei}$ and liner material, but that the values converge at order unity near peak compression. However, as in the case of the Ar test problem, the reduction in thermal conduction is negligible for all cases because the Hall parameter does not exceed 20 at any point in time.

The observations from both the Ar resistivity test problem and the different liner Z_A test problem can be summarized as follows: (a) for a gas-puff liner-on-target implosion on a 1 MA,

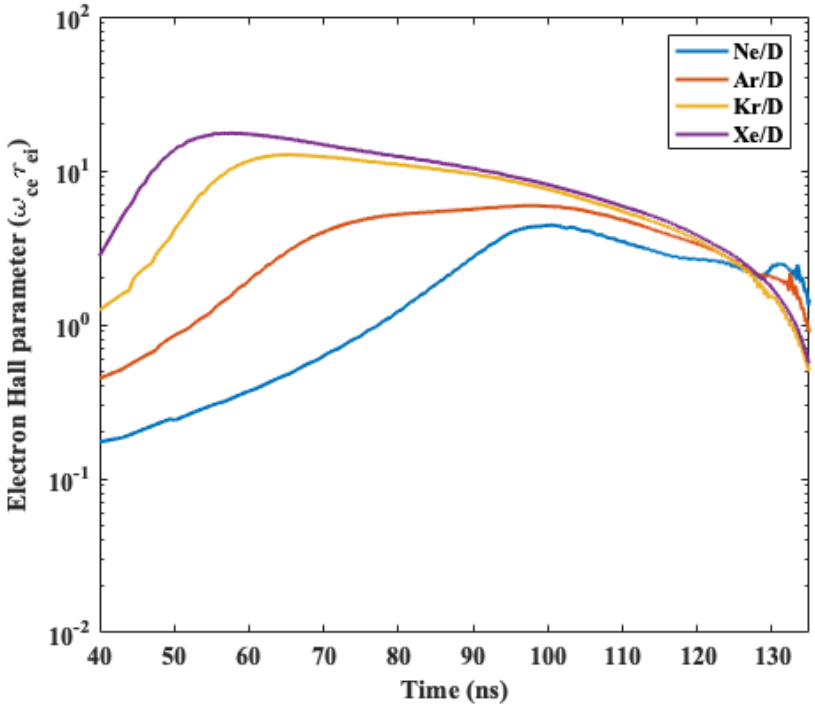

Figure 3.14: Electron hall parameter as a function of time for the different liner Z_A test problem. Because the simulations are Eulerian, here the interface is defined as outermost cell that is purely liner material.

100 ns driver, that changing either the material resistivity or the liner atomic number causes a demonstrable shift in time of shock initiation, but that net shock heating is predominantly controlled by liner inertia; (b) a material dependence on electron Hall parameter is observed, but in all test cases, it does not exceed 10, which would suggest negligible thermal insulation due to diffusion of azimuthal magnetic field.

3.5 MRT growth

Growth of the magneto-Rayleigh-Taylor instability was studied for the different liner Z_A test problem by running the same MACH2 simulations in 2-D, and applying a $\pm 1\%$ random density perturbation throughout to seed instability growth. The axial resolution for these simula-

tions was 100 μm, which sets a lower limit on the MRT wavelength. The lower limit needs to be comparable to or smaller than the limiting wavelength described in §2.5. For example, by Eq. 2.58, a liner with resistivity 10^{-5} Ωm undergoing a constant acceleration of 6×10^{12} m/s^2 has a minimum allowable wavelength of ~ 300 μm (for $f = 1$).

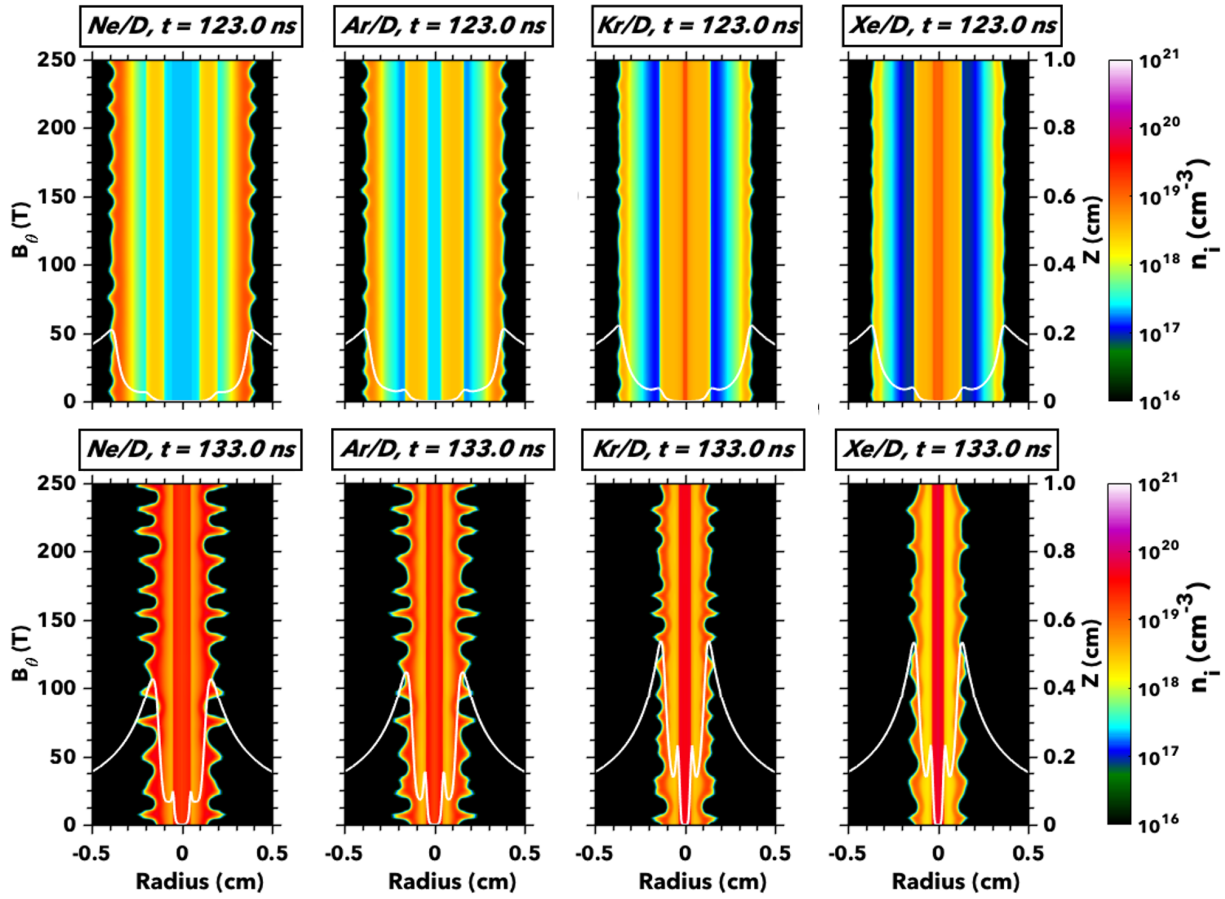

Figure 3.15: 2-D density contours at ∼20 (above) and ∼10 (below) ns prior to peak compression for the different liner Z_A test problem. The axially-averaged azimuthal magnetic field is overlaid, showing that field diffusion from the liner surfaces increases with liner Z_A. The growth of shorter-wavelength modes present in the Ne/D and Ar/D cases is mitigated in the Kr/D and Xe/D cases.

In this preliminary study, it was found that MRT growth was only significant near peak compression, as shown in 2-D density contours taken at approximately 10 and 20 ns prior to peak compression Fig. 3.15. The similarity in the structure of the density perturbation on the surface of the liner among the different liner materials is not coincidental. In this particular version of

MACH2, the pseudorandom number sequence that is applied to the density perturbation is static, meaning that the same random perturbation is applied to simulations that are identically meshed.

To quantify the perturbation growth and identify dominant wavelengths, liner radius as a function of axial location is defined as the point at which the ion density is below a specified cutoff value. The exact value is somewhat arbitrary; here we use $n_i = 10^{16}$ cm^{-3} to be consistent with Fig. 3.15. The average radius is subtracted so that the perturbation displacement ξ oscillates about zero. If the perturbation function were continuous, the Fourier transform of ξ at a wavenumber k is

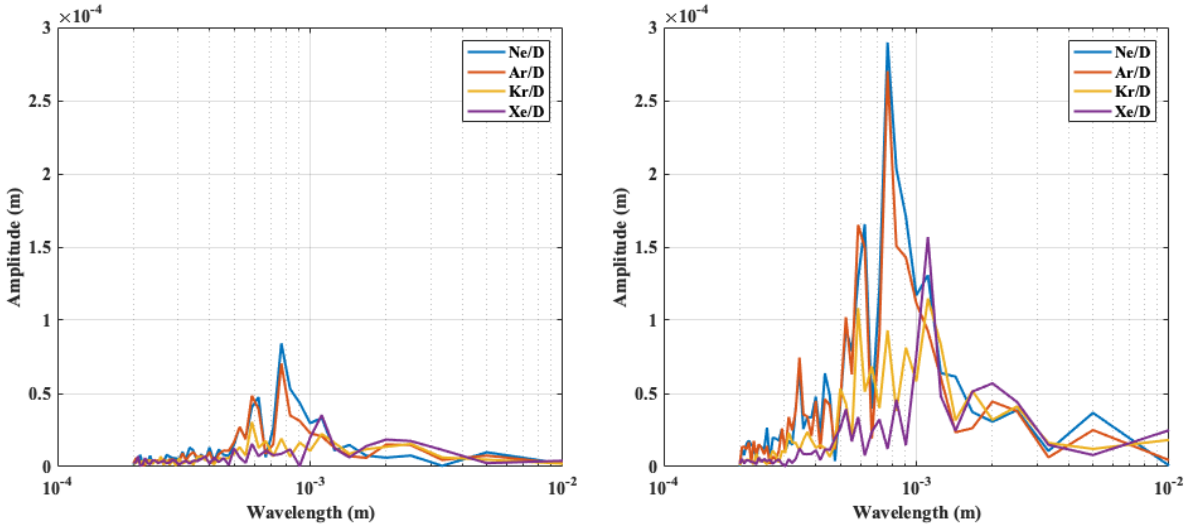

Figure 3.16: Discrete Fourier transform of the perturbation displacement on the liner surface at 20 ns prior and 10 ns prior to peak compression for each case in the different liner Z_A test problem. The lower limit of the transform of 200 μm is limited by the axial resolution of the problem, 100 μm.

$$\hat{\xi}(k) = \int_{-\infty}^{\infty} \xi(x) e^{-2\pi i k x} dx \tag{3.7}$$

However, the perturbation function is discrete, with the sampling "frequency" determined by the axial resolution of the simulation, which here is 100 μm. The discrete Fourier transform (DFT) at

wavenumber k is

$$\hat{\xi}(k) = \sum_{n=0}^{N-1} \xi_n e^{-2\pi i k n/(N-1)}, \tag{3.8}$$

where N is the number of interfaces. The wavenumbers k are

$$k_n = \frac{2\pi}{N-1} n, \;\; n = 0,1,2,...,N-1. \tag{3.9}$$

or equivalently,

$$k_n = \frac{2\pi}{N-1} n, \;\; n = -\frac{N-1}{2}, -\frac{N-1}{2}+1, ..., \frac{N-1}{2}. \tag{3.10}$$

The DFT is Hermitian, $\hat{\xi}^*(k) = \hat{\xi}(-k)$, so the magnitude of the single-sided function ($n = 1,2,...(N-1)/2$, i.e positive wavenumbers) is just double the magnitude of the original function for $n = 1,2,...,(N-1)/2$. For this particular problem, the axial resolution is 100 μm, so the range of possible wavenumbers is $100, 200, ..., 5000$ m^{-1} ($k = 0$ is discarded). Alternatively, this gives wavelengths ranging from the lowest possible, 200 μm, to a maximum of 1 cm. It is more useful (and intuitive) to consider wavelengths. The fast Fourier Transform function in MATLAB is used to perform the DFT on the density profiles shown in Fig. 3.15 to give displacement amplitude as a function of wavelength, shown in Fig. 3.16.

The dominant wavelengths in the Ne/D and Ar/D are in the range 550-800μm. These same wavelengths are present in the Kr/D and Xe/D simulations, but at much lower amplitudes. The dominant wavelength in the Kr/D and Xe/D simulation is 1.1 mm, and this wavelength is also present in the Ne/D and Ar/D simulations. Because the liner surface acceleration is determined by M/L, which is constant among the simulations, this suggests that the critical wavelength, below which density perturbations resistively diffuse away, is lower in the case of Ne/D and Ar/D relative to Kr/D and Xe/D.

This observation is consistent with the qualitative statements made elsewhere on MRT mitigation by resistive diffusion, e.g. [4]. However, it would be useful to reproduce this behavior

in experiment and using initial conditions in simulations that are more closely aligned with what is realistically achievable in experiments. It should finally be noted that mitigation by resistive diffusion from a high-Z_A liner is alone insufficient to adequately stabilize the load against MRT growth. In these simulations, the frequency-averaged amplitude ratio between the two plots is 4.1, 4.0, 3.7, and 3.6 for Ne/D, Ar/D, Kr/D, and Xe/D, respectively. The corresponding frequency-averaged *e*-folding times are less than 10 ns, so as might be expected, in each of the four cases the pinch is disrupted at or near peak compression. Later sections will consider additional MRT mitigation mechanisms.

3.6 Conclusion

In this chapter, it was shown that material resistivity can affect both shock formation and stability in liner-on-target gas-puff Z-pinches in two test problems. In the first test problem, an identical argon on deuterium load was simulated for three cases with three different resistivity tables. Two of these tables, SESAME 25171 and SESAME 25174 are part of the standard SESAME data table library, but disagree by orders of magnitude at low temperature. Furthermore, these tables have floor densities below those seen in university-scale SZP-like experiments except at peak compression, so use of these tables neglects the density dependence on resistivity that appears in the Coulomb logarithm if it is Spitzer-like. This motivated the development of a more-accurate, updated resistivity table courtesy of M. Desjarlais and Sandia National Laboratories, which was found to agree reasonably well with a constant multiple of Spitzer-like resistivity in the density and temperature range of university-scale Z-pinches.

It was found that, when liner thickness is of the order of the liner skin depth, magnetic field diffusion is significant, and that the corresponding diffused $\mathbf{J} \times \mathbf{B}$ can launch a shock in the target. It was found that the higher resistivity in correlated with earlier initiation of target compression, but that this did not translate to greater heating. This suggests that the determining

factor in shock strength for such a Z-pinch is liner inertia. The second test problem demonstrated a similar trend, in which the higher Z_A liners were more resistive, and thus resulted in earlier shock formation. Again, it was found that the net effect on target heating - quantified as mass-averaged target ion temperature as a function of target convergence ratio - was unaffected by liner material. It was also shown that, despite a significant fraction of the azimuthal magnetic field diffusion through the liner, the estimated electron Hall parameter at the interface did not exceed 20. This suggests that azimuthal magnetic field diffusion alone (in a gas-puff) would not substantially reduce radial thermal conduction from a hot target to a colder liner.

Finally, a preliminary consideration of stability supports the hypothesis that resistive diffusion can provide some stabilizing effect against MRT instability growth. This was demonstrated in 2-D simulations which showed that, under otherwise identical conditions - including the initial random perturbation - that the dominant sub-millimeter wavelengths observed in neon and argon-liner implosions were mitigated or suppressed in the krypton and xenon-liner implosions. Because the load mass was held constant among the four test problems, variations in acceleration on the liner surface were not present and cannot explain the difference in MRTI growth. A possible explanation is that higher-Z_A materials are more resistive (either due to higher ionization or lower temperature via greater radiation) than lower-Z_A materials, such that shorter-wavelength modes are more likely to diffuse away. It would be useful to either confirm or refute this observation in experiments. Estimates of the e-folding time of less than 10 ns near peak compression agree with the observed pinch disruption in simulation at or near peak compression independent of liner material, suggesting resistive diffusion alone is not sufficient for stabilizing a SZP-like load against the MRT instability.

3.7 Acknowledgments

Chapter 3, in part, includes material as it appears in “Shock formation in Ne, Ar, Kr, and Xe on deuterium gas puff implosions”, J. Narkis, H. U. Rahman, P. Ney, M. P. Desjarlais, F. J. Wessel, F. Conti, J. C. Valenzuela, and F. N. Beg, Phys. Plasmas **23**, 122706 (2016). J. Narkis was the primary author of this paper.

Chapter 4

A semi-analytic model for single liner-on-target, magneto-inertial fusion

4.1 Introduction

Semi-analytic models are useful tools for obtaining reasonably accurate, order-of-magnitude estimates of experimental performance in much shorter times than full-fledged simulations. This allows for a rapid parameter scan of initial conditions that, once completed, lays the groundwork for more sophisticated simulations. The work of Lindemuth and Kirkpatrick [26] is the standard example for magneto-inertial fusion. The model was recently expanded [51] from spherical geometry to include cylindrical geometry with either axial or azimuthal premagnetization. The results of the newer work generally supported the initial conclusions of [26] - that fusion conditions are readily achievable in all three geometries, but required substantial premagnetization and preheating in excess of 100 eV prior to adiabatic compression. While a very simple model, the results of [51] generally agree with the original MagLIF calculations by Slutz et al [15].

Contemporaneously, McBride and Slutz [77] developed a semi-analytic model for MagLIF (henceforth SAMM), a model of greater complexity than Lindemuth's, and solved the physics

equations relevant specifically to a MagLIF implosion. These include: fuel preheating (optionally by laser); liner compressibility with an analytic EOS, artificial viscosity, internal magnetic pressure, and ohmic heating; adiabatic compression and heating of the fuel; radiative losses and fuel opacity; magnetic flux compression with Nernst thermoelectric losses; magnetized electron and ion thermal conduction losses; end losses; mix losses; fusion reactions; and α-particle energy deposition. The predicted yield of the MagLIF point design was ~ 1 MJ/cm, compared to 500 kJ/cm in [15].

4.1.1 Modifications to SAMM

The equations developed for SAMM are insufficient for describing a SZP implosion, particularly on a university scale driver. This motivated the development of a semi-analytic model for SZP (henceforth SAMSZP), which would retain the appropriate equations of SAMM and replace or add equations where necessary.

First, the SZP is a magnetically-diffuse gas-puff, as opposed to a highly-conductive solid liner. It has been shown in simulations [41, 53, 61, 86] that a significant fraction of the azimuthal magnetic field can diffuse through the liner and accumulate on the interface between the target and the liner. We therefore solve the magnetic diffusion equation for the azimuthal magnetic field. This naturally leads one to question whether it is also necessary to solve the magnetic field diffusion equation for the axial magnetic field. Significant axial magnetic flux diffusion from the target to the liner would partially negate the thermal insulation resulting from the reduction in thermal conductivity due to fuel magnetization. Furthermore, if there is a significant temperature gradient between the fuel and the liner, axial flux is lost by the Nernst thermoelectric effect. This is believed to be responsible for significant flux losses in MagLIF (e.g. [15, 77]), but in performing HYDRA simulations to test our model, we found that, due to the snowplow compression of the liner, the net axial flux change is small enough to assume it is frozen in, and the Nernst losses are negligible relative to resistive diffusion. In its present form, the model assumes frozen-in axial

magnetic flux, though future work aimed at higher current (>10 MA) machines will include these effects in a similar manner as [77].

The second major modification to the model is inclusion of separate ion and electron temperatures, as well as separate conductivities. This is necessary, particularly on university-scale machines, because the electron-ion equilibration time is comparable to or larger than the implosion timescale. A more sophisticated ionization model is included than the one used in SAMM.

A shock model that explicitly solves the MHD Rankine-Hugoniot relations, Eqs. [2.25]-[2.29], is included. For simplicity, effects due to cylindrical convergence have been neglected. The fusion byproduct deposition model has been expanded to include other charged fusion byproducts, and a simple radiation model that accounts for liner and target emission, and liner absorption has been included.

4.2 Model description

As with SAMM, SAMSZP was written as a self-contained MATLAB script ($\sim 10^3$ lines) that takes on the order of 1 minute to run on a standard laptop computer. The model consists of approximately 100 couple ODEs solved using the built-in MATLAB solvers (typically ode23 or ode113). Future work will involve rewriting this model in a standalone program, giving the user more access over how the equations are solved. For example, we would like to implicitly solve the magnetic diffusion equation and explicitly solve other equations, which is not simple to do using MATLAB's built in solvers.

The models presented here are: (a) the set of circuit equations, including calculation of target and liner azimuthal flux change, (b) azimuthal magnetic field diffusion, (c) liner equations of motion, (d) liner heating and ionization, (e) target heating and compression by shock, (e) adiabatic target heating, (f) fusion reactions and byproduct deposition, and (g) radiation transport.

4.2.1 Circuit and azimuthal magnetic field equations

The circuit for a SZP load is modeled as a single-loop RLC circuit driven either by an external voltage source, V_{OC}, or by charging the capacitor to a certain voltage, V_C,

$$R_0 I + L_0 \dot{I} + V_{load} = V_C + V_{OC}, \tag{4.1}$$

where $V_C \equiv V_0 - \frac{1}{C_0}\int_0^t I(\tau)d\tau$. For example, the Zebra driver is modeled with the voltage waveform shown in Fig. 3.3, $V_C \equiv 0$, $R_0 = 2.3\ \Omega$, and $L_0 = 69$ nH. The Z driver is modeled as discussed in Ref. 77. The newly-constructed LTD machine at UC San Diego is modeled as a 580 nF capacitor bank charged to 200 kV, with $V_{OC} \equiv 0$, $R_0 = 47.5\ \text{m}\Omega$, $L_0 = 19$ nH.

Since we are using the MATLAB ODE solvers, each equation must be solved for the time derivative of a certain quantity, i.e. Eq. [4.1] is solved for $\dot{I}$:

$$\dot{I} = \frac{V_{OC} + V_0 - \int_0^t I(\tau)d\tau - R_0 I - \dot{L}_v I - \dot{\Phi}_{\theta,l} - \dot{\Phi}_{\theta,t}}{L_0 + L_v}. \tag{4.2}$$

The load voltage is calculated from Faraday's law as the time derivative of total magnetic flux in the volume. Since we will assume the total axial magnetic flux does not change, this leaves only the azimuthal flux change,

$$V_{load} = \dot{\Phi}_\theta = \dot{\Phi}_{\theta,v} + \dot{\Phi}_{\theta,l} + \dot{\Phi}_{\theta,t}, \tag{4.3}$$

Here the t, l, v subscripts refer to the target, liner, and vacuum, respectively. In order to define V_{load}, we have to first construct the azimuthal magnetic field equation. As with SAMM, the liner is discretized into N_{LS} shells, which have $N_{LI} = N_{LS} + 1$ interfaces. The number N_{LS} needs to be sufficiently large to prevent overcompression of the liner - we find 20 to be sufficient.

Each interface has an associated position (r_i), velocity $(\dot{r}_i)$, and azimuthal magnetic field $(B_{\theta,i})$. Each shell has a constant resistivity η_s, axial current density $J_{z,s}$, and axial magnetic field

$B_{z,s}$.

The Lagrangian form of the resistive magnetic field diffusion equation is

$$\dot{\mathbf{B}} = (\mathbf{B}\cdot\nabla)\dot{\mathbf{r}} - \mathbf{B}(\nabla\cdot\dot{\mathbf{r}}) - \nabla\times\left(\frac{\eta}{\mu_0}\nabla\times\mathbf{B}\right) \tag{4.4}$$

We will assume axial magnetic flux is frozen into the plasma, which is not true unless the magnetic Reynolds number, $Re_M \equiv Lu\mu_0/\eta$ is much larger than one. It is shown later that, for the university-scale SZP, the net axial magnetic flux diffusion from the target to the liner is less than a few percent during an implosion, so we have chosen to consider the flux frozen in. Azimuthal magnetic flux is constantly being added to the system, so we have to solve the diffusion equation for it:

$$\dot{B}_\theta = \frac{\partial}{\partial r}\left(\frac{\eta}{\mu_0 r}\frac{\partial}{\partial r}(rB_\theta)\right) - B_\theta\frac{\partial\dot{r}}{\partial r} \tag{4.5}$$

This describes the evolution of B_θ on internal interfaces, but on the outermost interface, N_{LI}, we know that

$$B_{\theta,N_{LI}} = \frac{\mu_0 I}{2\pi r_{N_L I}}, \tag{4.6}$$

$$\dot{B}_{\theta,N_{LI}} = \frac{\mu_0}{2\pi r_{N_{LI}}}\left[\dot{I} - \frac{\dot{r}_{N_{LI}}}{r_{N_{LI}}}I\right]. \tag{4.7}$$

Inside the liner, on interfaces $i = 2,3,\ldots,N_{LI-1}$, we discretize Eq. [4.5] using a central finite difference,

$$\dot{B}_{\theta,i} = \frac{1}{r_{i+1/2}-r_{i-1/2}}\left[\frac{\eta_{i+1/2}}{\mu_0}\left(\frac{1}{r_{i+1/2}}\frac{(rB_\theta)_{i+1}-(rB_\theta)_i}{r_{i+1}-r_i}\right)\right.$$
$$\left. -\frac{\eta_{i-1/2}}{\mu_0}\left(\frac{1}{r_{i-1/2}}\frac{(rB_\theta)_i-(rB_\theta)_{i-1}}{r_i-r_{i-1}}\right)\right] - \frac{B_{\theta,i}}{2}\left[\frac{\dot{r}_{i+1}-\dot{r}_i}{r_{i+1}-r_i} - \frac{\dot{r}_i-\dot{r}_{i-1}}{\dot{r}_i-\dot{r}_{i-1}}\right] \tag{4.8}$$

where $r_{i\pm1/2} = (r_i + r_{i\pm1})/2$, $\eta_{i-1/2} \equiv \eta_{s=i}$, and $\eta_{i+1/2} \equiv \eta_{s=i+1}$.

As a brief aside, it is typical (for example, in MACH2, but also in other codes) to use implicit time-stepping to advance the magnetic field due to its unconditional stability. For example, the Crank-Nicolson method is commonly implemented for diffusion-type equations. However, we were unable to successfully implement an implicit version of this model in MATLAB. In the future, we will rewrite this model as a standalone program, perhaps in Fortran, which might allow a better comparison with other similar models (e.g. the present form of the model in [26]).

As we will discuss later when describing fuel heating, the target is discretized into at most two shells, so the azimuthal magnetic field at the interface between the liner and target ($i = 1$) and the field inside the target cannot be solved for directly. Some sort of assumption about the shape of the profile is therefore necessary. A schematic illustrating the model discretization is shown in Figure 4.1.

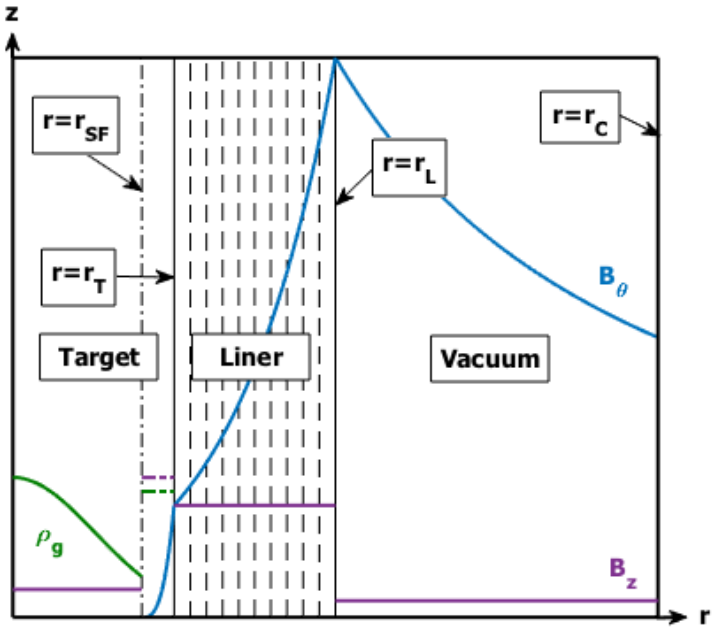

Figure 4.1: Schematic of the load discretization. There are three main regions: target, liner, and vacuum. If a shock is present in the target, that region is subdivided into an unshocked region, characterized by the initial conditions (e.g. here, the density profile is Gaussian), and a shock region, characterized by the relevant average quantities. The liner is subdivided into N_{LS} regions or shells. Axial magnetic field is assumed conserved in each region, including the vacuum - it is not necessarily constant. Azimuthal magnetic field evolves according to the magnetic field diffusion equation. B_θ is assumed to approach zero at the shock front.

This model is being developed for SZP implosions, in which there is a strong shock in the target plasma. The post-shock temperature is typically in excess of 10^2 eV, so the resistivity will be $< 10^{-6}$ Ωm, assuming it is Spitzer-like. If a shock is present, then B_θ will drop rapidly, so that we may assume that at the shock front, r_{SF}, $B_\theta = 0$. Although not necessarily true, we will assume that the post-shock target can be characterized by a single resistance, η_S.

In addition to these assumptions, a magnetic field profile must be assumed. As in Ref. [77] for B_θ in the liner, we assume a power-law dependence of the magnetic field in the target,

$$B_\theta(r) = \begin{cases} 0 & r \le r_{SF}, \\ B_{\theta,1}\left(\frac{r-r_{SF}}{r_1-r_{SF}}\right)^\beta & r_{SF} \le r_1. \end{cases} \tag{4.9}$$

The value of β determines the steepness of the profile, which depends on the magnetic Reynolds number within the shock front. If the magnetic Reynolds number is very high, β will tend toward 1 and B_θ will be linear. As Re_M decreases, the profile will tend to steepen, and β should increase. This was confirmed in a series of simple MHD test problems in MACH2. By this argument, we use an ad-hoc definition for β which ensures this general behavior,

$$\beta \equiv \max\left\{1, \ln\left(\frac{\eta_S/\mu_0}{|\dot{r}_1|(r_1 - r_{SF})}\right)\right\}. \tag{4.10}$$

With the magnetic field profile specified inside the target, the magnetic field at the target-liner interface is written as

$$\dot{B}_{\theta,1} = \frac{1}{r_{3/2} - r_{1/2}}\left[\frac{\eta_{3/2}}{\mu_0}\left(\frac{1}{r_{3/2}}\frac{(rB_\theta)_2 - (rB_\theta)_1}{r_2 - r_1}\right) - \frac{\eta_S}{\mu_0}\left(\nabla B_1^-\right)\right] - \frac{B_1}{2}\left[\frac{\dot{r}_2 - \dot{r}_1}{r_2 - r_1} + \frac{\dot{r}_1 - \dot{r}_{SF}}{r_1 - r_{SF}}\right] \tag{4.11}$$

where ∇B_1^- is ∇B_1 approaching from the left. By Eq. [4.9], $\nabla B_{\theta,1^-} = \frac{B_{\theta,1}\beta}{r_1 - r_{SF}}$.

Prior to shock formation, we assume that $\beta = 1$ and replace r_{SF} with $r_1/2$ in Eq. [4.9].

The axial current density is obtained from Ampere's law,

$$J_z(r) = \begin{cases} 0 & r \leq r_{SF} \\ \frac{1}{\mu_0 r}\left[B_{\theta,1}\left(\frac{r-r_{SF}}{r_1-r_{SF}}\right)^{\beta}\right] + \frac{B_{\theta,1}\beta}{\mu_0(r_1-r_{SF})^{\beta}}(r-r_{SF})^{\beta-1} & r_{SF} < r \leq r_1 \end{cases} \tag{4.12}$$

When the shock has just formed, $r_1 \approx r_{SF}$ so $\beta \to \infty$ and thus $J_z \to \infty$. As expected, during the development and testing of the model this led to anomalously high Ohmic heating in the target shortly after the shock formed. To avoid this anomalous heating, an upper value of 10 is used for β. The exact value of the upper limit was found to essentially arbitrary, so long as it is sufficiently larger than one.

It should be stated again for emphasis that axial magnetic flux is assumed frozen in for this model. While this has been shown to be largely valid for a SZP implosion on a 1-MA driver, approximately 25% of the axial magnetic flux in the target is lost from the target to the liner in the original MagLIF calculations [15].

Furthermore, axial magnetic flux can be lost by the Nernst thermoelectric effect. The original SAMM model [77] includes a Nernst term, but the calculation of this term requires a temperature gradient in the fuel. In SAMM, a temperature gradient is assumed because the laser preheating is done on axis, and a "burn wave" propagates radially outward. However, our model assumes the (post-shock) density and temperature are constant. In SAMSZP, the Nernst term would be added to the magnetic field equation. It has the form, in 1-D (CGS) [94]

$$\left[\frac{\partial B_x}{\partial t}\right]_{\text{Nernst}} = \frac{\partial}{\partial x}\left(\frac{n\omega_e\tau_e\left[1.5(\omega_e\tau_e)^2+3.053\right]}{m_e\left[(\omega_e\tau_e)^4+14.79(\omega_e\tau_e)^2+3.7703\right]}\frac{c}{en}\frac{\partial T}{\partial x}\right) \tag{4.13}$$

It is necessary to consider when $\omega_{ce}\tau_e \gg 1$, which does not generally apply to past or present SZP loads. However, it may be necessary for SZP loads in the future.

To calculate liner resistivity, we note that field diffusion is radial, i.e. perpendicular to the magnetic field, and that, in general, the plasmas considered here sufficiently collisional. It is

therefore reasonable to use Spitzer-Braginskii transverse resistivity [39, 49],

$$\eta_\perp\ [\Omega\mathrm{m}] = \frac{m_e \nu_{ei}}{e^2 n_e} = \frac{m_e}{e^2 n_e} \frac{4\sqrt{2\pi} e^4 \bar{Z}^2 n_i \ln\Lambda}{[4\pi\varepsilon_0]^2 3\sqrt{m_e}\,(q_e T_e)^{3/2}} = \frac{4\sqrt{2\pi}\sqrt{m_e} e^2}{[4\pi\varepsilon_0]^2 3 q_e^{3/2}} \frac{(\bar{Z})^2}{\bar{Z}} \ln\Lambda T_e^{-3/2}$$
$$\approx 1.03 \times 10^{-4} \bar{Z} \ln\Lambda (T_e\ [\mathrm{eV}])^{-3/2} \quad (4.14)$$

where ν_{ei} is the electron-ion collision frequency. The Coulomb logarithm is calculated as in Appendix A of Ref. [77], which uses $\ln\Lambda = \max[1, \ln(\lambda_D / b_{min})]$, where λ_D is the Debye length,

$$\lambda_D = \sqrt{\frac{\varepsilon_0 kT}{e^2 (n_e + \bar{Z}^2 n_i)}} \quad (4.15)$$

and the minimum impact parameter, b_{min}, is the larger of the classical and quantum minimum impact numbers,

$$b_{min} = \max\left[\frac{\bar{Z} q_e^2}{12\pi\varepsilon_0 kT}, \frac{\hbar}{2 m_e v_{th,e}}\right] \quad (4.16)$$

4.2.2 Load voltage

Recall that the load voltage is calculated by the integral form of Faraday's law,

$$V_{load} = \frac{\partial \Phi}{\partial t} = \frac{\partial \Phi_t}{\partial t} + \frac{\partial \Phi_l}{\partial t} + \frac{\partial \Phi_v}{\partial t} \quad (4.17)$$

where, because the total axial magnetic flux in the system is conserved, these refer only to changes in azimuthal flux. The voltage due to the change in magnetic flux in the target is written

$$\frac{\partial \Phi_{\theta t}}{\partial t} = \frac{\partial}{\partial t}\left(h \int_{r_{SF}}^{r_1} B_\theta(r) dr\right) = h B_\theta(r_1)\dot{r}_1 - h B_\theta(r_{SF})\dot{r}_{SF} + h \int_{r_{SF}}^{r_1} \frac{\partial}{\partial t}\left(B_\theta(r_1)\left(\frac{r - r_{SF}}{r_1 - r_{SF}}\right)^\beta\right) dr$$
$$= h\left[\frac{(r_1 - r_{SF})\dot{B}_\theta(r_1) + (\dot{r}_1 - \dot{r}_{SF}) B_\theta(r_1)}{\beta + 1}\right] \quad (4.18)$$

where h is the pinch length, noting that$B_\theta(r_{SF})$ is zero and neglecting the time-dependence

of β. By the definition of azimuthal magnetic field inside the target, this could improperly treat azimuthal magnetic flux and give a somewhat erroneous voltage. Future implementations of this code (i.e. in a standalone executable rather than in MATLAB) will give greater flexibility with treating azimuthal flux.

The voltage change due to azimuthal magnetic flux for liner shell s, is, approximately

$$\begin{aligned}\dot{\Phi}_{\theta l,s} &= \frac{\partial}{\partial t}\left(h\int_{r_{i=s}}^{r_{i=s+1}} B_\theta dr\right) = h(B_\theta(r_{i=s+1})\dot{r}_{i=s+1} - B_\theta(r_{i=s})\dot{r}_{i=s}) + h\int_{r_{i=s}}^{r_{i=s+1}} \dot{B}_\theta dr \\ &\approx h(B_\theta(r_{i=s+1})\dot{r}_{i=s+1} - B_\theta(r_{i=s})\dot{r}_{i=s}) + \frac{h}{2}(r_{i=s+1} - r_{i=s})(\dot{B}_\theta(r_{i=s+1}) + \dot{B}_\theta(r_{i=s})) \quad (4.19)\end{aligned}$$

On the liner surface, recall that

$$\dot{B}_{\theta,N_{LI}} = \frac{\mu_0}{2\pi r_{N_{LI}}}\left[\dot{I} - \frac{\dot{r}_{N_{LI}}}{r_{N_{LI}}} I\right],$$

and with the definition of load voltage, Eq. 4.2 is now

$$\dot{I} = \frac{V_{OC} + V_0 - \int_0^t I(\tau)d\tau - R_0 I - \dot{L}_v I - \dot{\Phi}_{\theta,l} - \dot{\Phi}_{\theta,t}}{L_0 + L_v} \equiv \frac{\sum V - \dot{\Phi}_{\theta l,N_{LS}}}{L_0 + L_v}$$

This expression must be substituted into the definition for $\dot{B}_\theta(r_{i=N_{LI}})$, i.e.

$$\begin{aligned}\dot{\Phi}_{\theta l,N_{LS}}\left[1 + \frac{h}{2}(r_{i=s+1} - r_{i=s})\frac{\mu_0}{2\pi r_{LI}(L_0 + L_v)}\right] &= h(B_\theta(r_{i=s+1})\dot{r}_{i=s+1} - B_\theta(r_{i=s})\dot{r}_{i=s}) + \\ &\frac{h}{2}(r_{i=s+1} - r_{i=s})\left(\frac{\mu_0}{2\pi r_{LI}}\left[\frac{\sum V}{L_0 + L_v} - \frac{\dot{r}_{LI}}{r_{LI}}\right] + \dot{B}_\theta(r_{i=s})\right) \quad (4.20)\end{aligned}$$

With this, all the values are specified to calculate the load voltage self-consistently.

4.2.3 Liner equations of motion

In each of the N_{LS}, constant material properties are assumed. The equations of motion of each of the N_{LI} liner interfaces can be written simply as

$$\ddot{r}_i = 2\pi r_i h \left[\frac{p_{s-1} - p_s}{(m_{s=i-1} - m_{s=i})/2} \right] \tag{4.21}$$

where each shell s has mass m and total pressure p. Each pressure p is comprised of material pressure $p_{m,s}$, azimuthal magnetic pressure $p_{B_\theta,s}$, axial magnetic pressure $p_{B_z,s}$, and an artificial viscous pressure q_s.

The initial liner density profile is approximated as Gaussian,

$$\rho_l(r) = \rho_{0,l} \exp \left[-\frac{-4\ln(2)(r - r_{0,l})^2}{w_{0,l}^2} \right] \tag{4.22}$$

where $\rho_{0,l}$ is the peak density centered at $r_{0,l}$, and $w_{0,l}$ is the full width at half maximum (FWHM) of the liner.

Since this is a Lagrangian model, the total mass in each shell is conserved. The mass of each shell is then simply the integral of the density profile from the inner interface $r_{i=s}$ to the outer interface $r_{i=s+1}$,

$$m_s = 2\pi\rho_0 h \int_{r_{i=s}}^{r_{i=s+1}} r \exp \left[-\frac{-4\ln(2)(r - r_{0,l})^2}{w_{0,l}^2} \right] dr \tag{4.23}$$

which, since it is only evaluated once to initialize the simulation, is integrated numerically.

Because the liner in the SZP is a noble gas, it is reasonable to model the liner as an ideal monatomic gas, so the material pressure in each liner shell is

$$p_{m,s} = \frac{2}{3} \frac{E_s}{V_s} \tag{4.24}$$

where E_s and V_s are the internal energy and volume of the shell, respectively. The volume of the shell is obviously $V_s = \pi(r_{i=s+1}^2 - r_{i=s}^2)h$.

Because the azimuthal magnetic field is defined on the interfaces, the azimuthal magnetic shell pressure is taken using the average of the B_θ at the interfaces,

$$p_{B_\theta,s} = \frac{1}{2\mu_0}\left[\frac{B_{\theta,i=s} + B_{\theta,i=s+1}}{2}\right]^2 \tag{4.25}$$

As axial magnetic flux is assumed constant in each liner shell, it is simply

$$p_{B_z,s} = \frac{B_{z,s}^2}{2\mu_0} \tag{4.26}$$

Because the azimuthal magnetic field gradient at the target-liner interface can be significantly discontinuous, the azimuthal magnetic pressure is split from the EOM for r_1,

$$\ddot{r}_1 = \frac{p_{m,S} + p_{Bz,S} - p_1}{m_1/2} \cdot 2\pi r_1 h - \frac{\nabla P_{B_\theta}^- + \nabla P_{B_\theta}^+}{2\rho_1} \tag{4.27}$$

where

$$\begin{aligned} \nabla P_{B_\theta}^- &= \frac{B_1^2\beta}{\mu_0(r_1 - r_{SF})}, \\ \nabla P_{B_\theta}^+ &= \frac{B_1(B_2 - B_1)}{\mu_0(r_2 - r_1)}. \end{aligned} \tag{4.28}$$

The equation of motion for the liner-vacuum interface, $r_{N_{LI}}$, is

$$\ddot{r}_{N_{LI}} = \frac{p_{s=N_{LI-1}} - p_{B_\theta,v} - p_{B_z,v}}{m_{s=N_{LI-1}}/2}. \tag{4.29}$$

where subscript v denotes vacuum quantities. The azimuthal magnetic field pressure is obtained

directly from the current,

$$p_{B_\theta,v} = \frac{\mu_0 I^2}{8\pi^2 r_{N_{LI}}^2} \tag{4.30}$$

The vacuum pressure from the axial magnetic field decreases with time, because of the frozen-in flux assumption. The magnetic field B_z decreases with the change in area,

$$B_{z,v} = \frac{\Phi_{z,v}}{\pi(r_C^2 - r_{N_{LI}}^2)} = B_{z,0}\frac{r_C^2 - r_{N_{LI,0}}^2}{r_C^2 - r_{N_{LI}}^2} \tag{4.31}$$

where r_C is the radius of the return current. The pressure is then

$$p_{B_{z,v}} = \frac{B_{z,0}^2}{2\mu_0}\left[\frac{r_C^2 - r_{N_{LI,0}}^2}{r_C^2 - r_{N_{LI}}^2}\right]^2 \tag{4.32}$$

The final remaining quantity to specify is the artificial viscous pressure. The same model is used as in Ref. [77],

$$q_s = \begin{cases} a_q^2 \rho_{l,s}(\dot{r}_{i,s=i+1} - \dot{r}_{i,s=i})^2 & \dot{r}_{i=s} > \dot{r}_{i=s+1}, \\ 0 & \dot{r}_{i=s} \leq \dot{r}_{i=s+1}. \end{cases} \tag{4.33}$$

a_q is an arbitrary quantity of order unity. This model, as is standard in implementations of artificial viscosity, is only positive when the volume of a shell is increasing.

4.2.4 Liner heating and ionization

The final quantity to specify in the liner EOMs is the internal energy of the shell. To model this reasonably well in a semi-analytic model of a SZP, it is necessary to consider the electron and ion internal energies of each shell separately, because (a) significant temperature gradients can develop between shells, and (b) particularly at lower densities, electrons and ions are not in thermal equilibrium. This is because the equilibration time can be of the order of the

implosion time or greater. The internal energy of shell s, E_s, is divided into ion energy ($E_{i,s}$) and electron energy ($E_{e,s}$), where

$$E_{i,s} = \frac{3}{2} N_s q_e T_{i,s}, \tag{4.34}$$

$$E_{e,s} = \frac{3}{2} \bar{Z}_s N_s q_e T_{e,s}. \tag{4.35}$$

where N_s, $\bar{Z}_s$, and $T_{i(e),s}$ are the number of ions, average ionization state, and average ion (electron) temperature (in eV) in shell s, respectively, and $q_e = 1.6 \times 10^{-19}$ J/eV.

It is standard in MHD to use either analytic models (e.g. the Saha equation) or tabular data (e.g. SESAME) to calculate the ionization state as a function of density and electron temperature. In the typical SZP implosion, the liner material is argon or krypton, so for this work it was necessary to obtain ionization models for those materials. Non-LTE simulations using the atomic physics code PrOpacEOS [95] were performed to obtain these tables. In an effort to maintain the transparency and reproducibility of this model, we decided to model the results of these simulations by fitting them to an ad-hoc formulation. It was seen that the average ionization state of these two gases was modeled reasonably well at a particular density as a summation of error functions. The shape of the function also shifts as a function of density, but retained its monotonicity. The model thus had the form

$$\bar{Z} = C_0 + \sum_{i=1}^{n} C_i \operatorname{erf}\left(a_i \left(T_{log} - b_i\right)\right), \tag{4.36}$$

where T_{log} is $\log_{10}(T_e\ [\text{eV}])$, a_i and b_i are fit coefficients given in Table 4.1, $C_0 \approx C_1 + C_2 + \cdots + C_n \approx A/2$ where A is the atomic number of the liner.

While agreement could be improved with a more rigorous fitting, the models are a good approximation of the original function, and an improvement over the model used in SAMM: $\bar{Z} = \min\left[20\sqrt{T\ [\text{keV}]}, A\right]$. Using this model, as shown in a comparison of the three models in

Fig. 4.2, will tend to underestimate $\bar{Z}$ and thus overestimate T_e. This could significantly affect the dynamics and heat conduction in the liner.

Table 4.1: Fit coefficients for the ionization models for argon and krypton, Eq. 4.36. $n \equiv \log_{10}(n_i)\ \left[\text{cm}^{-3}\right]$.

	Argon	Krypton
C_0	9	18
C_1	4	4
a_1	$-0.021875n^2+0.85n-6.4125$	$-0.01875n^2+0.625n-3.175$
b_1	$0.01875n^2-0.65n+6.425$	$0.01875n^2-0.625n+5.875$
C_2	4	9
a_2	2.6	$0.009375n^2-0.225n+2.6125$
b_2	2.2	$-0.00625n^2+0.2n+0.725$
C_3	1	4
a_3	$0.01875n^2-0.625n+7.475$	$-0.071895n^2+2.625n-20.0625$
b_3	$-0.003125n^2+0.075n+3.0625$	$-0.009375n^2+0.3n+1.0375$

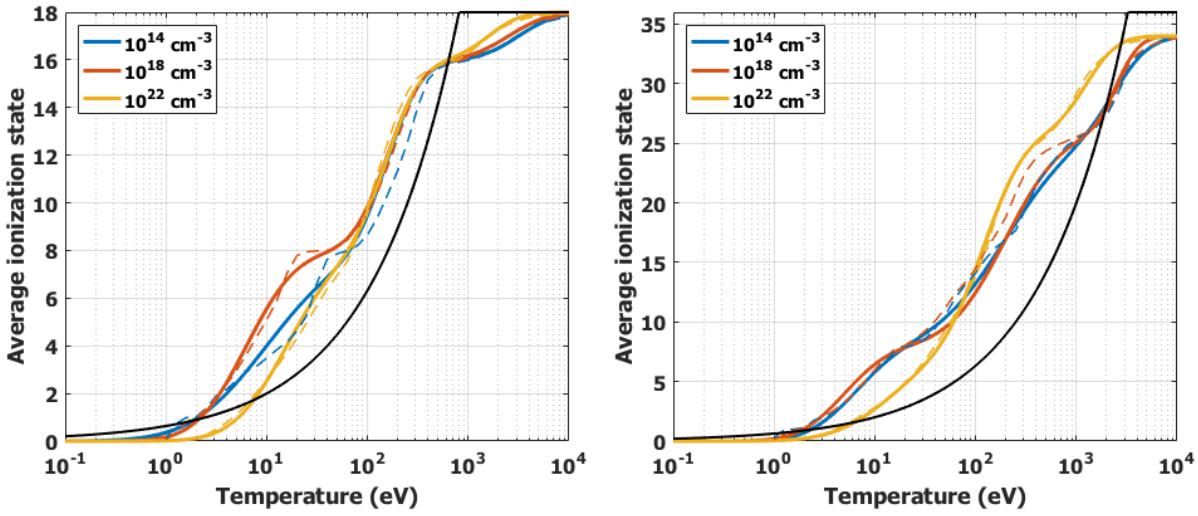

Figure 4.2: Average ionization state of argon (left) and krypton (right) as functions of temperature for $n_i = 10^{14}$,10^{18}, and 10^{22} cm^{-3}. The solid colored lines are from Eq. 4.36, the dashed colored lines are from PrOpacEOS calculations, and the solid black line is $\bar{Z} = \min\left[20\sqrt{T\ [\text{keV}]}, A\right]$.

In this model, the electron and ion electron energies of each shell are the tracked quantities. Both ion and electron temperatures are obtained from the internal energies, but it is more

straightforward to do with the ion equation. Since $\bar{Z}$ is a monotonic function of T_e for a given density, which is known, it is simplest to iteratively guess the correct T_e to obtain the correct $E_{e,s}$ within a small error - here 0.1% is used. The linear bisection method is used to guess the correct ionization method. In this method, the first guess is $\bar{Z} = A/2$ - halfway between 0 and A. If this gives too low a value for $E_{e,s}$, then the new lower limit is A/2, and the next guess is halfway between A/2 and A, $\bar{Z} = 3A/4$.. If the value is too high, then the new upper limit is A/2, and the next guess is halfway between 0 and A/2, $\bar{Z} = A/4$. This process continues until $\bar{Z}$ converges on a value within 0.1%, which takes about 10 iterations. This is certainly computationally inefficient to do for every shell at every timestep, so future implementations of the model will consider more efficient methods to obtain $\bar{Z}$.

Once $\bar{Z}$, T_e, and T_i are obtained, the various heating and loss rates of the liner can be considered. For ions, they are: PdV heating, electron-ion equilibration, and thermal conduction. For electrons, they are PdV Heating, electron-ion equilibration, thermal conduction, Ohmic heating, and radiation - both emission and absorption:

$$\dot{E}_{i,s} = P_{i,PdV,s} + P_{ei,s} + P_{ic,s}, \tag{4.37}$$

$$\dot{E}_{e,s} = P_{e,PdV,s} - P_{ei,s} + P_{ec,s} + P_{\Omega,s} - P_{rad,s} + P_{rad,abs,s} \tag{4.38}$$

The PdV heating term of species p in shell s is

$$P_{p,PdV,s} = -\frac{2}{3}\frac{E_{p,s}}{V_s}\dot{V}_s = -\frac{4E_{p,s}}{3}\frac{r_{i=s+1}\dot{r}_{i=s+1} - r_{i=s} - \dot{r}_{i=s}}{r_{i=s+1}^2 - r_{i=s}^2} \tag{4.39}$$

The negative sign is necessary so that PdV heating is positive when the volume of a shell decreases.

Electron-ion equilibration is calculated by following Ref. [96] and write the change in electron temperature as

$$\dot{T}_e = \frac{(1+\bar{Z})T_{eq}}{\tau_{eq}}\frac{1 - T_e/T_{eq}}{(T_e/T_{eq})^{3/2}}, \tag{4.40}$$

where T_{eq} and τ_{eq} are the equilibration temperature and time, respectively,

$$T_{eq} = \frac{T_i + \bar{Z}T_e}{1+\bar{Z}}, \tag{4.41}$$

$$\tau_{eq} = \frac{3}{8\sqrt{2\pi}} \left(\frac{4\pi\varepsilon_0}{e^2}\right)^2 \frac{m_i^2}{\bar{Z}^2 m_e^{1/2}} \frac{\left(qT_{eq}\right)^{3/2}}{\rho \ln \Lambda_{eq}}, \tag{4.42}$$

where $e = 1.6 \times 10^{-19}$ C is the elementary charge, m_i is ion mass in kg, $m_e = 9.11 \times 10^{-31}$ kg is the electron rest mass, and $\ln \Lambda_{eq}$ is the Coulomb logarithm evaluated at T_{eq}. The change in ion temperature is

$$\dot{T}_i = -\bar{Z}\dot{T}_e \tag{4.43}$$

and the energy gained by the ions in shell s is then

$$P_{ei,i,s} = -\frac{3}{2} N_{i,s} q_e \bar{Z}_s \dot{T}_{e,s} = -P_{ei,e,s} \tag{4.44}$$

Ion thermal conduction, P_{ic}, and electron thermal conduction, P_{ec}, in a particular shell is calculated by estimating conduction across the shell's inner and outer interface. The ion and electron thermal conduction across interfaces $i = 2, \ldots, N_{LI}$, is

$$P_{ic,i} = 2\pi r_i h \frac{\kappa_{i,s=i-1} + \kappa_{i,s=i}}{2} q_e \left[\frac{\partial T_i}{\partial r}\right]_i, \tag{4.45}$$

$$P_{ec,i} = 2\pi r_i h \frac{\kappa_{i,s=i-1} + \kappa_{e,s=i}}{2} q_e \left[\frac{\partial T_e}{\partial r}\right]_i \tag{4.46}$$

where the temperature gradient is approximated as

$$\left[\frac{\partial T_p}{\partial r}\right]_i = \frac{T_{p,s=i} - T_{p,s=i-1}}{r_{c,s=i} - r_{c,s=i-1}}, \tag{4.47}$$

where $r_{c,s} \equiv (r_{i=s} + r_{i=s+1})/2$ and where the thermal conductivity, κ of species p in shell s is

$$\kappa_{p,s} = \frac{n_{p,s} q_e T_{p,s} \tau_{pi}}{m_p} \mathcal{F}_{p,s}(x_{p,s}). \tag{4.48}$$

$\mathcal{F}_{p,s}$ are Braginskii (for ions) and Epperlein-Haines (for electrons) corrections that account for the reduction in thermal conductivity due to magnetization [77]. They are functions of the ion ($x_{i,s} = \omega_{ci,s}\tau_{ii,s}$) and electron ($x_{e,s} = \omega_{ce,s}\tau_{ei,s}$) Hall parameters, respectively,

$$\mathcal{F}_{i,s} = \frac{2.645 + 2x_{i,s}^2}{0.677 + 2.70x_{i,s}^2 + x_{i,s}^4}, \tag{4.49}$$

$$\mathcal{F}_{e,s} = \frac{6.18 + 4.66x_{e,s}}{1.93 + 2.31x_{e,s} + 5.35x_{e,s}^2 + x_{e,s}^3} \tag{4.50}$$

In calculating the Hall parameters, we note that B_θ can be large within the shell, so the magnetic field used to calculate the cyclotron frequencies is the magnitude of the total field, $B_s \equiv (B_{\theta,s}^2 + B_{z,s}^2)^{1/2}$. The collision times are

$$\tau_{ei,s} = \frac{6\sqrt{2}\pi^{3/2}\varepsilon_0^2\sqrt{m_e}(q_e T_{e,s})^{3/2}}{n_{i,s}\bar{Z}_s^2 e^4 \ln\Lambda_s}, \tag{4.51}$$

$$\tau_{ii,s} = \frac{12\pi^{3/2}\varepsilon_0^2\sqrt{m_e}(q_e T_{i,s})^{3/2}}{n_{i,s}\bar{Z}_s^4 e^4 \ln\Lambda_s} \tag{4.52}$$

Across a true liner-vacuum interface, thermal conduction is zero. However, in a SZP load the interface is somewhat diffuse. By design, this model (and any Lagrangian model of the SZP) assumes a sharp liner-vacuum boundary, which will lead to overheating in the outermost shell. This in turn leads to a decrease in resistivity and reduced azimuthal field diffusion into the liner, and greater Ohmic heating (since J_z^2 increases faster than η_s decreases), which strengthens the positive feedback loop. To compensate, we allow for electron thermal conduction into the vacuum region corresponding to a saturated flux, described shortly.

Across the target-liner interface, thermal conduction is written

$$P_{ic,1} = 2\pi r_1 h \frac{\kappa_{i,s=1} + \kappa_{i,S}}{2} q_e \left[\frac{\partial T_i}{\partial r}\right]_1, \tag{4.53}$$

$$P_{ec,1} = 2\pi r_1 h \frac{\kappa_{e,s=1} + \kappa_{e,S}}{2} q_e \left[\frac{\partial T_e}{\partial r}\right]_1, \tag{4.54}$$

where

$$\left[\frac{\partial T_p}{\partial r}\right]_1 = \frac{T_{p,s=1} - T_{p,S}}{r_{c,s=1} - r_{c,s=0}} \tag{4.55}$$

where $\kappa_{i(e),S}, T_{i(e),s}$ are ion (electron) thermal conductivity and temperature in the shock front, if present, and $r_{c,s=0} \equiv r_1 - (r_2 - r_1)/2$. If there is shock present, they are the unshocked values.

In order to model electron thermal conduction as a diffusive process, it is necessary for the electrons to be sufficiently collisional, i.e. that the length scales of the temperature gradient are much larger than the electron mean free path,

$$\lambda_{e,s} = v_{th,e}\tau e = (4\pi\varepsilon_0)^2 \frac{3}{4\sqrt{2\pi}} \frac{m_e^{1/2} v_{th} (q_e T_{e,s})^{3/2}}{n_e q_e^4 \ln\Lambda}, \tag{4.56}$$

where $v_{th} = \sqrt{2qT_e/m_e}$ is the electron thermal velocity.

For the plasmas under consideration, this assumption is often true, but not necessarily. Figure 4.3 shows the electron mean free path as a function of temperature at constant density for several densities that are typically obtained in university-scale SZPs. It is therefore useful to calculate a saturated electron flux, which is standardly taken as a coefficient multiplied by the square root of the thermal velocity times the pressure, e.g. [97–99]. We use the coefficient proposed by Cowie [97],

$$P_{ec,sat} = 2\pi r h \left[0.4 \left(\frac{2q_e T_e}{\pi m_e}\right)^{1/2} n_e q_e T_e\right] \tag{4.57}$$

This ensures that the electrons cannot "diffuse" at a velocity that exceeds their thermal velocity.

A similar limit is used for ions.

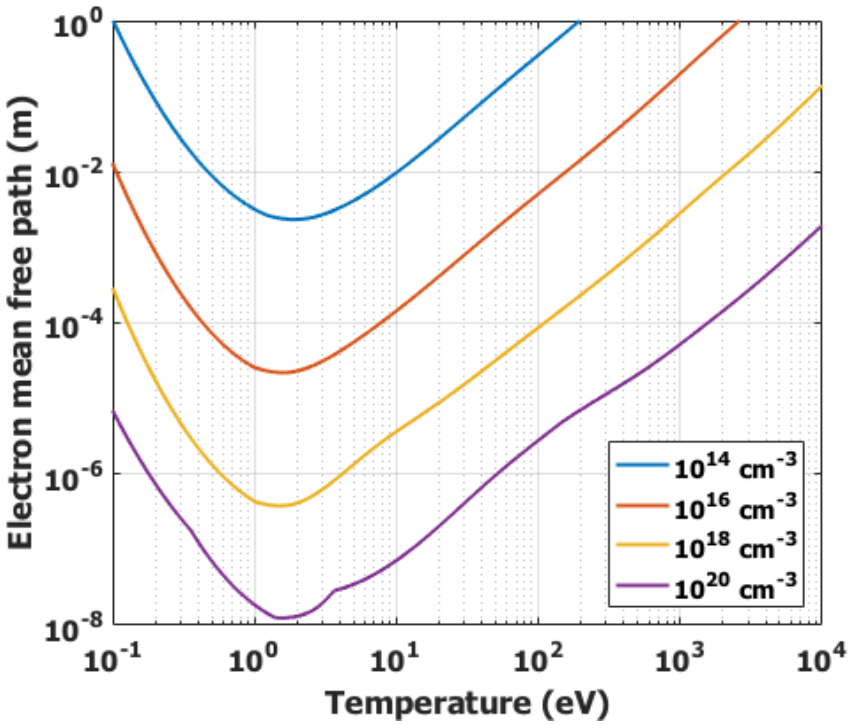

Figure 4.3: Electron mean free path in krypton as a function of temperature for $n_i = 10^{14}$,10^{16}, 10^{18} and 10^{20} cm^{-3}. Ionization level (for n_e) and the Coulomb logarithm are calculated using the models presented elsewhere in this work.

Ohmic heating in each shell is straightforward to calculate, as constant resistivity and constant current density are assumed in each shell,

$$P_{\Omega,s} = \eta_s J_{z,s}^2 V_s \tag{4.58}$$

where

$$J_{z,s} = \frac{1}{\mu_0 r_{c,s}} \frac{(rB_\theta)_{i=s+1} - (rB_\theta)_{i=s}}{r_{i=s+1} - r_{i=s}} \tag{4.59}$$

noting again that $r_{c,s} \equiv (r_{i=s} + r_{i=s+1})/2$.

If only isotopes of hydrogen are used in the model, it would be appropriate to assume that the dominant radiation losses are due to bremsstrahlung and use only that model. However,

particularly for higher-Z materials like a SZP liner, calculating only bremsstrahlung will underestimate the total radiation losses because line radiation can be comparable or larger. To account for this in our simple model, we have relied again on PrOpacEOS simulations, which output the total radiation cooling (here, $\xi_L(\rho, T_e)$, where L is the liner material) as a function of density and temperature. The function output has units W/g, so to obtain the power we write

$$P_{rad,s}\ [\mathrm{W}] = 10^3 \xi_L(\rho, T_e)(\rho_s V_s). \tag{4.60}$$

As with the model for ionization, formulaic approximations for the cooling function are developed. For details on the formulation, see Appendix D of [100]. A comparison of the formulaic approximations to PrOpacEOS simulations are shown in Figure 4.4. Due to the irregular shape of the cooling functions, it was difficult to generate an approximation that agreed very well for all temperatures and densities. However, calculating radiation cooling by interpolating lookup tables was found, peculiarly, to drastically increase the run-time of the simulation. This could be a consequence of the rapidly varying, non-monotonic nature of the cooling tables.

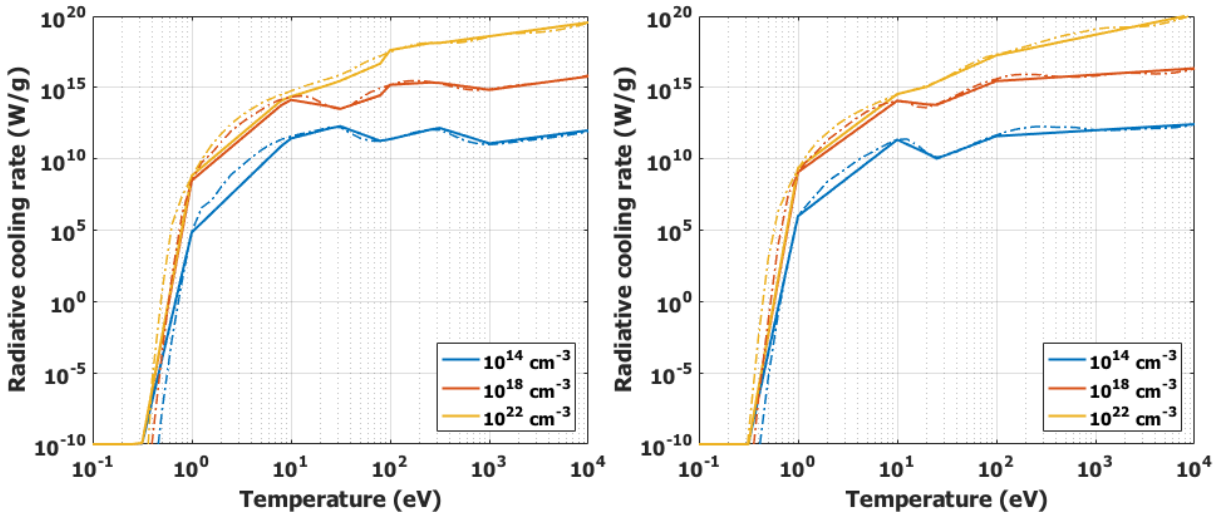

Figure 4.4: Radiative cooling functions for argon (left) and krypton (right) as a function of temperature for $n_i = 10^{14}$, 10^{18} and 10^{22} cm^{-3}. Solid lines are from Ref. [100] and dashed lines are from PrOpacEOS simulations.

The last term in Eq. 4.38 is radiation absorption. One of the inherent challenges in modeling a SZP implosion is that the liner transitions from optically thin to (potentially) optically thick as its converges on the axis. The diffusion approximation for radiation is only valid when the liner is optically thick, meaning that the mean free path of a photon is small relative to the liner thickness. If the liner is optically thin, then all radiation emitted escapes, but if the liner is optically thick, a fraction of the emitted radiation is reabsorbed. Furthermore, we account for radiation that is lost to the electrodes, which can be significant for large aspect ratio liners - but is typically not for a SZP liner.

The radiation absorption equation is discussed more in detail in §4.2.7, here we summarize the model as

$$P_{rad,s} = P_{rad,end,s} + P_{rad,abs,s} + P_{rad,esc,s}. \tag{4.61}$$

That is to say, the total radiation emitted of shell s is either lost to the ends ($P_{rad,end,s}$), absorbed ($P_{rad,abs,s}$), or escapes the system ($P_{rad,esc,s}$).

4.2.5 Target heating

Target heating occurs in three phases that are separated by either the appearance or disappearance of a shock front. A shock front will not be present in the target while the velocity of the target/liner interface ($\dot{r}_1$) is below the sound speed, c_S, of the target. Any heating during this phase is essentially negligible, but the relevant heating rates are calculated for completeness.

Once $|\dot{r}_1| > c_S$, the shock jump conditions are solved for so that the Rankine-Hugoniot relations derived in §2.3 are satisfied. In comparing the results of this model with HYDRA simulations, we concluded that accounting for effects due to cylindrical convergence do not significantly affect the overall results or conclusions made by using this model.

Following the shock arrival on axis, the target is assumed isobaric and isothermal and undergoes only PdV heating.

Compression and heating by shock

The shock jump conditions in a SZP target have already been derived in §2.3, so the complete derivation will not be presented here. However, there are some differences that should be noted. First, the shock jump conditions are typically solved in the reference frame of the fluid, but the conditions here are solved in the laboratory frame, because we know the upstream and downstream velocities, but do not know the velocity of the shock front. The jump conditions are then written

$$\rho_S(\dot{r}_S - \dot{r}_{SF}) = \rho_U(\dot{r}_U - \dot{r}_{SF}), \tag{4.62}$$

$$B_{zS}(\dot{r}_S - \dot{r}_{SF}) = B_{zU}(\dot{r}_U - \dot{r}_{SF}), \tag{4.63}$$

$$\rho_S(\dot{r}_S - \dot{r}_{SF})^2 + p_S + \frac{B_{zS}^2}{2\mu_0} = \rho_U(\dot{r}_U - \dot{r}_{SF})^2 + p_U + \frac{B_{z,U}^2}{2\mu_0}, \tag{4.64}$$

$$\begin{aligned} &\frac{1}{2}\rho_S(\dot{r}_S - \dot{r}_{SF})^3 + \frac{\gamma_S}{\gamma_S - 1}p_S(\dot{r}_S - \dot{r}_{SF}) + \frac{(\dot{r}_S - \dot{r}_{SF})B_{zS}^2}{\mu_0} \\ &= \frac{1}{2}\rho_U(\dot{r}_U - \dot{r}_{SF})^3 + \frac{\gamma_U}{\gamma_U - 1}p_U(\dot{r}_U - \dot{r}_{SF}) + \frac{(\dot{r}_U - \dot{r}_{SF})B_{zU}^2}{\mu_0} \end{aligned} \tag{4.65}$$

where the subscript U denotes an unshocked quantity, the subscript S denotes a shocked quantity, and r_{SF} is the location of the shock front. The known quantities are $\dot{r}_S,\ \dot{r}_U, \rho_U,\ B_{zU}$, and p_U, and γ_U and γ_S are the unshocked and shock adiabatic indices - if one were to account for, for example, the dissociation of deuterium by a shock. The four unknown quantities are $\rho_S,\ \dot{r}_{SF},\ B_{zS}$, and p_S, which are solved for algebraically in a similar fashion as outlined in §2.3. The value of ρ_U is known by assuming that the initial density profile is a Gaussian,

$$\rho_s = \rho_{0,t} \exp\left[\frac{-4\ln(2)r_{SF}^2}{w_{0,t}^2}\right] \tag{4.66}$$

where again $w_{0,t}$ is the FWHM. The value of the shock front is known at the beginning of each timestep. Since the velocity of the shock front is assumed stationary, $\dot{r}_U = 0$. The post-shock

velocity $\dot{r}_S \equiv \dot{r}_1$, and B_{zU} is the initial value B_{z0} - or close to it, if the interface has shifted slightly.

It is important to note that these equations only satisfy the jump conditions across the shock front. To conserve axial magnetic flux and mass within the target, there has to be some sort of post-shock density and B_z profile. Mass is conserved by explicitly tracking the number of shocked and unshocked target particles. The post-shocked density profile can be characterized by an average density, $\bar{\rho}_S$. Similarly, axial magnetic flux is conserved by writing the flux in the post-shock region as

$$\Phi_{zS} = \Phi_{zT} - \Phi_{zU} = \pi(r_{T0}^2 B_{z0} - r_{SF}^2 B_{zU}), \tag{4.67}$$

which has an average field

$$\bar{B}_{zS} = \Phi_{zS}/(\pi(r_1^2 - r_{SF}^2)) \neq B_{zS} \tag{4.68}$$

These quantities are used when a post-shock quantity is necessary, e.g. in the equation of motion for r_1.

As in the liner, it is potentially necessary to allow for the pre- and (particularly) the post-shock electron and ion temperatures to be different. The total energy of the fuel is divided into four categories: unshocked ion and electron energies, and shocked ion and electron energies:

$$E_{Ui} = \frac{3}{2} N_{Ui} q_e \bar{T}_{Ui}, \tag{4.69}$$

$$E_{Ue} = \frac{3}{2} N_{Ue} q_e \bar{T}_{Ue}, \tag{4.70}$$

$$E_{Si} = \frac{3}{2} N_{Si} q_e \bar{T}_{Si}, \tag{4.71}$$

$$E_{Se} = \frac{3}{2} N_{Se} q_e \bar{T}_{Se}. \tag{4.72}$$

By including the factor of $\frac{3}{2}$, we have inherently assumed $\gamma = 5/3$ for both materials. For deuterium fuel, this means that we have assumed the deuterium has completely dissociated. Deuterium dissociates at 4.6 eV and is fully dissociated and ionized at 15.5 eV [101], so this is an incorrect assumption. However, typically, much more energy is added by shock preheating so

this is an acceptable inaccuracy that does not affect the final results.

The total number of unshocked ions and its time derivative are, noting again that the target is assumed to have a Gaussian profile,

$$N_U = \frac{1}{m_{iT}} \int_0^{r_{SF}} 2\pi r_* \rho_{0,t} h \exp\left[\frac{-4\ln(2) r_*^2}{w_{0,t}^2}\right] dr_* = \frac{\pi \rho_{0,t} w_{0,t}^2 h}{4\ln(2) m_{iT}} \left(1 - \exp\left[\frac{-4\ln(2)}{w_{0,t}^2} r_{SF}^2\right]\right), \tag{4.73}$$

$$\dot{N}_U = \frac{2\pi r_{SF} \dot{r}_{SF} \rho_{0,t} h}{m_{iT}} \exp\left(\frac{-4\ln(2)}{w_{0,t}^2} r_{SF}^2\right). \tag{4.74}$$

The average shocked target temperature, $\bar{T}_S$ is not necessarily the post shock temperature as determined by solving for the jump conditions. This is because the shock jump conditions are instantaneous, and only apply to particles travelling through (i.e. being heated) the shock front. In addition, losses will lower the average post-shock temperature, and those losses may be different in ions and electrons. The set of evolution equations for the target energies is

$$\dot{E}_{Ui} = \frac{3}{2} \dot{N}_U q_e \bar{T}_{Ui} + P_{ei,U} + P_{ic,1\to U}, \tag{4.75}$$

$$\dot{E}_{Ue} = \frac{3}{2} \dot{N}_U q_e \bar{T}_{Ue} - P_{ei,U} + P_{ec,S\to U} - P_{rad,U} + P_{ec,1\to U} + P_{\Omega,U}, \tag{4.76}$$

$$\dot{E}_{Si} = \frac{3}{2} \dot{N}_S q_e T_S + P_{ei,S} + P_{ic,1\to S} + P_{PdV,i}, \tag{4.77}$$

$$\dot{E}_{Se} = \frac{3}{2} \dot{N}_S q_e T_S - P_{ei,S} - P_{ec,S\to U} - P_{rad,s} + P_{PdV,e} + P_{ec,1\to S} + P_{\Omega,S}. \tag{4.78}$$

$P_{ei,(U,S)}$ is electron-ion equilibration,

$$\dot{T}_{i,(U,S)} = \bar{\nu}_{(U,S)}^{i\backslash e} (T_{e,(U,S)} - T_{i,(U,S)}) \tag{4.79}$$

where the frequency $\bar{\nu}^{i\backslash e}_{(U,S)}$ is [49]

$$\bar{\nu}^{i\backslash e}_{(U,S)} = 5.7\times10^{-27}\frac{\left(m_{i(U,S)}m_e\right)^{1/2}\bar{Z}^2_{i,(U,S)}n_{e,(U,S)}\ln\Lambda_{(U,S)}}{\left(m_{i,(U,S)}T_{e,(U,S)}+m_eT_{i,(U,S)}\right)^{3/2}} \tag{4.80}$$

where all quantities are in MKS and T is in eV. This is equivalent to Eqs. 4.41-4.42 for $\bar{Z}=1$.

The thermal velocity of electrons is typically greater than the velocity of the front itself, so electrons are free to conduct ahead of the front [81], whereas ions cannot. To account for this, electron conduction ahead of the shock front is approximated as

$$P_{ec,S\rightarrow U} = 2\pi r_{SF}h\kappa_{Se}q_e\frac{\partial T_e}{\partial r} \tag{4.81}$$

where the temperature gradient is

$$\frac{\partial T_e}{\partial r} = \frac{\bar{T}_{Se}-\bar{T}_{Ue}}{(r_1+r_{SF})/2-r_{SF}/2} \tag{4.82}$$

Thermal conduction is calculated and limited as in §4.2.4. Because the target is D or DT, radiation losses are primarily due to bremsstrahlung,

$$P_{rad,(U,S)}\ [W] = 1.5\times10^{-36}V_{(U,S)}\ [m^3]\left(T_{(U,S)e}\ [\mathrm{eV}]\right)^{1/2}\left(n_{(U,S)e}\ [m^{-3}]\right)^2\bar{g}_B \tag{4.83}$$

where $\bar{g}_B$ is the frequency average of the velocity-averaged Gaunt factor, which ranges from 1.1-1.5. It is typical to assume a constant value of $\bar{g}_B = 1.2$, which is accurate to within 20% [47].

In the post-shock region of the target, compression is subsonic, so it is necessary to account for the PdV heating there,

$$P_{PdV,i(e)} = \frac{-2}{3}\frac{E_{Si(e)}}{V_S}\dot{V}_S = \frac{-4}{3}E_{S,i(e)}\frac{r_1\dot{r}_1-r_{SF}\dot{r}_{SF}}{r_1^2-r_{SF}^2} \tag{4.84}$$

While at first it may seem counterintuitive, the post-shock PdV heating is actually negative at larger radii. This is because the volume of the shocked target is actually increasing, i.e. $|r_1\dot{r}_1| < |r_{SF}\dot{r}_{SF}|$.

Thermal conduction across the interface is partitioned into conduction into the shocked region and unshocked regions. This is because, when the shock first forms, the width of the shock front can be comparable to or smaller than the respective conduction mean free path. The conductions are divided as

$$P_{(i,e)c,1\to S} = P_{(i,e)c,1}\left[1 - e^{-(r_1 - r_{SF})/\lambda_{(i,e)}}\right], \tag{4.85}$$

$$P_{(i,e)c,1\to U} = P_{(i,e)c,1} - P_{(i,e)c,1\to S}. \tag{4.86}$$

The axial current density in the target is needed to calculate Ohmic heating in the target, but it has already been defined in §4.2.1 as

$$J_z(r) = \begin{cases} 0 & r \le r_{SF}, \\ \frac{1}{\mu_0 r}\left[B_1\left(\frac{r - r_{SF}}{r_1 - r_{SF}}\right)^{\beta}\right] + \frac{B_1\beta}{\mu_0(r_1 - r_{SF})^{\beta}}(r - r_{SF})^{\beta-1} & r_{SF} < r < r_1 \end{cases} \tag{4.87}$$

Because the second term scales as $r_1 - r_{SF}$ when $r_1 \approx r_{SF}$, the value of J_z diverges regardless of the value of β when the shock has just formed. To circumvent this nonphysicality, we replace r_{SF} with $\hat{r}_{SF} \equiv \min(r_{SF}, r_1 - \lambda_{eS})$ in $J_z(r)$ and in the Ohmic heating calculation,

$$P_{\Omega,target} = 2\pi\eta_S h \int_{\hat{r}_{SF}}^{r_1} r J_z(r)^2 dr. \tag{4.88}$$

The various heating terms for the target have now been defined.

Adiabatic target heating

When the shock front arrives on the axis, the target c_S is less than the implosion velocity. This means that any perturbations to the target will dissipate on a sufficiently short timescale that the subsequent target compression can be considered isentropic. To switch from shock heating to adiabatic heating, the MATLAB ODE solver is terminated and reinitialized, combining the shocked and unshocked target energies into one value each for electrons and ions. The liner equations remain the same.

The justification for this is due to numerical errors inherent in the MATLAB ODE solver. When the shock front r_{SF} reaches the axis, the total number of unshocked particles and the corresponding unshocked ion and electron energies are all identically zero. However, in testing the model this was found not to occur. Some quantities would approach zero and go negative, and simply preventing the relevant quantities from being negative is not viable, because the quantities would perpetually approach zero without reaching it. To avoid these complications, the shock heating phase is ended when one of the following conditions is met: $r_{SF} < 10\ \mu$m, $N_U < 0$, $E_{Ue} < 0$, or $E_{Ui} < 0$.

Furthermore, the number of deuterons and tritons is now tracked separately for fusion calculations. The total ion energy is the summation of shocked and unshocked ion energy, and the same is true for electron energy.

The energy evolution equations for the target are now

$$\dot{E}_i = \frac{-4}{3}\frac{\dot{r}_1}{r_1}E_i + P_{ei} - P_{ic}, \tag{4.89}$$

$$\dot{E}_e = \frac{-4}{3}\frac{\dot{r}_1}{r_1}E_e - P_{ei} - P_{ec} - P_{rad} + P_{\Omega} + P_{dep}. \tag{4.90}$$

where all the quantities are the same as before, but the shock front and unshocked quantities are zero. A new quantity related to the energy deposition of charged fusion byproducts is also included, and described in the following section.

4.2.6 Fusion reactions and byproduct deposition

The SZP can either have deuterium or deuterium-tritium fuel, so as in SAMM [77] fusion reaction rates for D-D and D-T fusion are calculated:

$$\mathrm{D}+\mathrm{D} \rightarrow 50\%(\mathrm{T}+\mathrm{p})+50\%(\mathrm{He}^3+\mathrm{n}),$$

$$\mathrm{D}+\mathrm{T} \rightarrow \mathrm{He}^4+\mathrm{n}.$$

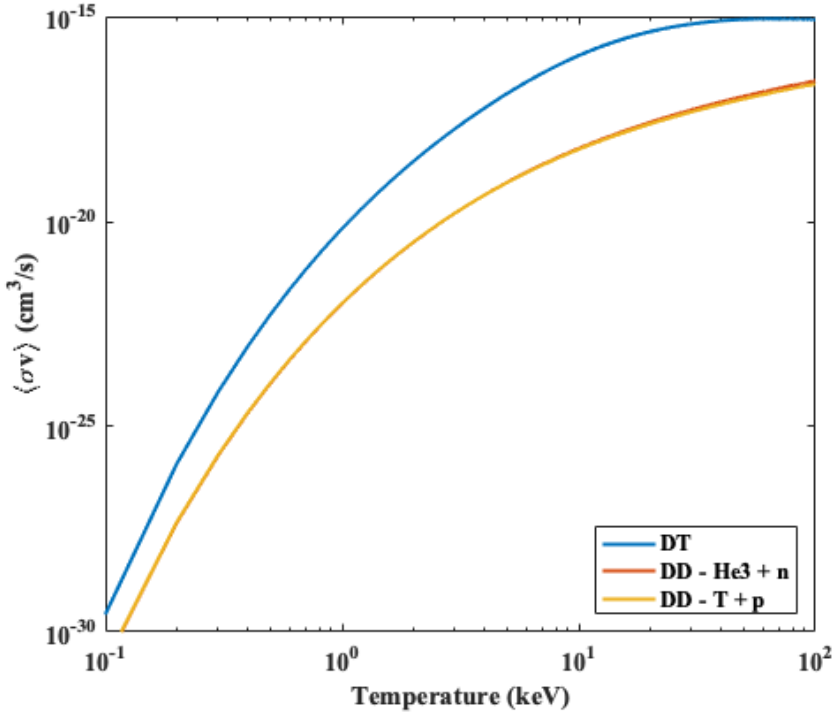

Figure 4.5: Reactivities for DD and DT reactions versus temperature. The reactivities for the two possible DD reactions are nearly equal for most cases studied with the model.

The corresponding reaction rates are

$$\dot{N}_{\mathrm{DD,T}} = \frac{\pi r_1^2 h}{2} n_{\mathrm{DD}}^2 \langle\sigma v\rangle_{\mathrm{DD,T}}, \tag{4.91}$$

$$\dot{N}_{\mathrm{DD,He^3}} = \frac{\pi r_1^2 h}{2} n_{\mathrm{DD}}^2 \langle\sigma v\rangle_{\mathrm{DD,He^3}}, \tag{4.92}$$

$$\dot{N}_{\mathrm{DT}} = \pi r_1^2 h n_{\mathrm{D}} n_{\mathrm{T}} \langle\sigma v\rangle_{\mathrm{DD,He^3}} \tag{4.93}$$

where the reactivities have the form [102, 103]

$$\langle \sigma v \rangle = c_1 \zeta^{-5/6} T_i^{-2/3} \exp\left(-c_2 \zeta^{1/3} T_i^{-1/3}\right), \tag{4.94}$$

$$\zeta = 1 - \frac{c_3 T_i + c_4 T_i^2 + c_5 T_i^3}{1 + c_6 T_i + c_7 T_i^2 + c_8 T_i^3}, \tag{4.95}$$

and are plotted for reference in Fig. 4.5.

The byproducts of these reactions that are not neutrons are charged particles that can deposit their energy into the target. If the stopping time of the fusion byproducts is small relative to the hydrodynamic timescales, then the energy of these particles can be absorbed by Coulomb collisions. If the magnitude of the magnetic field in the target is sufficiently large, such that the gyroradius of a particular byproduct is smaller than the radius of the target, then the particle is trapped and has a greater chance of depositing its energy in the fuel. In ICF, when α-particle (He^4) energy deposition exceeds energy losses by radiation and conduction, the target "ignites" and undergoes runaway heating. This is generally considered necessary to reach breakeven in an ICF-type reactor, but it is not strictly necessary for the entire magnetized target fusion parameter space [26].

In order to calculate the energy deposition by charged fusion particles, it is necessary to either explicitly track their populations and calculate some form of coupling with the target, or more simply, to calculate the instantaneous energy deposition and assume the remainder escapes. SAMM and this model both use the latter approach. However, in this model, it is necessary to consider the charged particle deposition from DD fusion reactions, because most if not all near-future experimental work on SZPs will use deuterium fuel.

For simplicity, the formulation of deposition for any charged particle follows the model developed for α-particle deposition developed by Basko [104]. Each charged byproduct particle

b has an associated energy Q_b and birth velocity v_{b0},

$$Q_b = (E_b\ [\text{eV}])q_e, \tag{4.96}$$

$$v_{b0} = \sqrt{\frac{2Q_b}{m_b}}, \tag{4.97}$$

as well as an ionization level $\bar{Z}_b$ and mass m_b. The relevant values are listed in Table 4.2.

Table 4.2: Relevant quantities for estimating the deposition of energy into the fuel by charged fusion byproducts.

b	E_b [MeV]	$\bar{Z}_b$	m_b (amu)
T	1.01	1	3.016
p	3.02	1	1.007
He^3	0.82	2	3.016
He^4	3.5	2	4.002

The fraction of particle energy that is deposited into the fuel is given by

$$f_b = \frac{x_b + x_b^2}{1 + 13x_b/9 + x_b^2}, \tag{4.98}$$

where x_b is

$$x_b = \frac{8}{3}\left(\frac{r_1}{l_b} + \frac{y^2}{\sqrt{9y^2 + 1000}}\right). \tag{4.99}$$

These two terms can be thought of as the unmagnetized and magnetized contributions to the energy deposition. In the first term, l_b is the electron-ion mean free path of particle b,

$$l_b = (4\pi\varepsilon_0)^2 \frac{3}{4\sqrt{2\pi}} \frac{m_b v_{b0}(q_e T_e)^{3/2}}{n_e \bar{Z}_b^2 e^4 m_e^{1/2} \ln\Lambda} \tag{4.100}$$

That is to say, in even the event that there is zero magnetic field in the target, some α-particle deposition can occur. As the density of the target increases, the mean free path decreases and the fraction of energy deposited increases. This is what occurs in conventional ICF. When a magnetic field is present in the fuel, the charged particles can be trapped in the fuel if the magnetic field is

strong enough. In Eq. 4.99, y is the ratio of the fuel radius to the gyroradius of particle b,

$$y \equiv \frac{r_1}{r_{bL}} = r_1 \left[\frac{m_b v_{b0}}{\bar{Z}_b q_e \left(B_{zt}^2 + \bar{B}_{\theta t}^2 \right)^{0.5}} \right]^{-1} \tag{4.101}$$

The azimuthal magnetic field is non-uniform, so a volume average is used

$$\bar{B}_{\theta t} = \frac{1}{\pi r_1^2 h} \int_0^{r_1} 2\pi r_1 h B_1 \left(\frac{r}{r_1} \right)^{\beta} dr = \frac{2B_1}{\beta + 2} \tag{4.102}$$

The total fusion power, accounting for byproduct deposition and secondary neutron yield is

$$P_{\mathrm{DD,total}} = \dot{N}_{\mathrm{DD,T}}[(1 - f_T)Q_T + (1 - f_p)Q_p] + \dot{N}_{\mathrm{DD,He^3}}[(1 - f_{\mathrm{He^3}})Q_{\mathrm{He^3}} + Q_{\mathrm{n,DD}}], \tag{4.103}$$

$$P_{\mathrm{DT,total}} = (\dot{N}_{\mathrm{DT,prmy}} + \dot{N}_{\mathrm{DT,sndy}})[(1 - f_{\mathrm{He^4}})Q_{\mathrm{He^4}} + Q_{\mathrm{n,DT}}]. \tag{4.104}$$

and the total power redeposited into the fuel is

$$P_{\mathrm{dep}} = \dot{N}_{\mathrm{DD,T}}(f_T Q_T + f_p Q_p) + \dot{N}_{\mathrm{DD,He^3}} f_{\mathrm{He^3}} Q_{\mathrm{He^3}} + \dot{N}_{\mathrm{DT}} f_{\mathrm{He^4}} Q_{\mathrm{He^4}} \tag{4.105}$$

Finally, the total neutron yields are

$$Y_{\mathrm{DD,n}} = N_{\mathrm{DD,He^3}}, \tag{4.106}$$

$$Y_{\mathrm{DT,n}} = N_{\mathrm{DT,prmy}} + N_{\mathrm{DT,sndy}} \tag{4.107}$$

4.2.7 Radiation emission and transport

Modeling of radiation transport in MHD codes is typically done using some form of diffusion equation, where the diffusion coefficient is a function of the photon mean free path. This approach is only valid in the optically-thick limit, i.e. the photon mean free path is comparable or smaller to the relevant system scale lengths. It is often the case that in a SZP implosion,

particularly on university-scale machines, that the liner is initially optically thin, meaning all produced emission escapes, and becomes optically thick as the load converges on axis. In most cases, the load is optically thin. If the optical depth of the liner is not accounted for, then the liner may over-compress, which can over-predict the amount of target heating and yield.

An additional challenge with modeling radiation transport is how to discretize it. In the simplest approach, we can treat it as an evenly distributed (in space and solid angle) photon flux originating in a cylinder (if it is target radiation) or in an annular shell (if it is liner radiation). All the produced radiation is either lost to the ends, or assumed to propagate radially - half in the positive direction and half in the negative direction.

Radiation production in the target

In modeling target radiation, we assume for simplicity that (even if a shock front is present), it is emitted uniformly throughout the target volume. A photon can originate anywhere within the cylinder, described in cylindrical coordinates as $P_{0,cyl} = (r_0, z_0, \theta_0)$, and in spherical coordinates as $P_{0,sph} = (\sqrt{r_0^2 + z_0^2}, \theta_0, \tan^{-1}(r_0/z_0))$. This photon can have any direction, and the surface it passes through - the top, bottom, or side, depends on the solid angle subtended by each surface at P_0. Consider first the top surface, located at $z = Z$, where the solid angle subtended by P_0 is

$$\Omega_t = \int_0^{2\pi} \int_0^{\phi_{\max}(\theta)} sin\phi d\phi d\theta \tag{4.108}$$

where the maximum polar angle, $\phi_{\max}$ is a function of θ, schematically shown in Figure 4.6. If the cylinder has radius R, then it follows that

$$\phi_{\max} = \tan^{-1}\left[\frac{\sqrt{R^2 + r_0^2 - 2Rr_0\cos(\theta - \theta_0)}}{Z - z_0}\right] \tag{4.109}$$

Since the integral is performed about 2π, the value of θ_0 is arbitrary, so it can be set to zero.

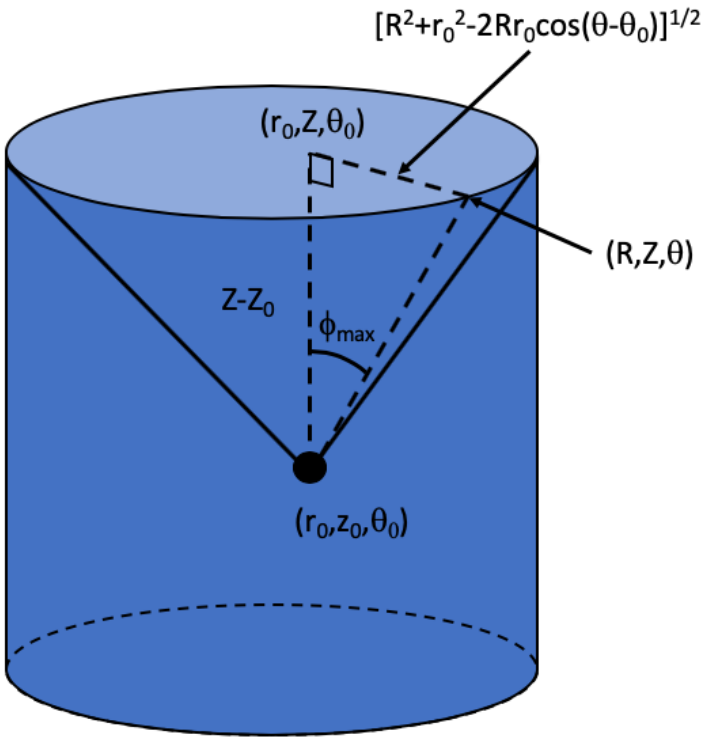

Figure 4.6: Schematic of the solid angle subtended by the top of a cylinder at a point in the cylinder. The limits of the integration for the subtended angle are 0 to 2π for θ, and 0 to $\phi_{\max}$ for ϕ, which is a function of θ.

Completing the integral in ϕ gives

$$\Omega_t = \int_0^{2\pi} \cos(0) - \cos(\phi_{\max}) d\theta = \int_0^{2\pi} 1 - \frac{Z - z_0}{\sqrt{R^2 + r_0^2 \cos\theta + (Z - Z_0)^2}} d\theta, \tag{4.110}$$

where the identity $\cos\left(\tan^{-1}(x)\right) = 1/\sqrt{x^2+1}$ has been used. The solid angle subtended by the bottom surface is simply

$$\Omega_b = \int_0^{2\pi} \cos(0) - \cos(\phi_{\max}) d\theta = \int_0^{2\pi} 1 - \frac{Z - z_0}{\sqrt{R^2 + r_0^2 \cos\theta + (Z - Z_0)^2}} d\theta, \tag{4.111}$$

These two expressions are equal if the photon is at the center of a cylinder, and equal to the standard formula for a solid angle subtended by a cone with apex angle 2θ and radius 1,

$$\Omega = 2\pi(1-\cos(\theta),$$

where here $\theta \equiv \tan^{-1}(2R/Z)$.

The solid angle subtended by the side surface at P_0 is simply

$$\Omega_{s,P_0} = 4\pi - \Omega_{t,P_0} - \Omega_{b,P_0}, \tag{4.112}$$

The fact that the photon can originate anywhere in the cylinder is addressed by considering the relevant volume-averaged solid angles,

$$\bar{\Omega}_{(b,t),P_0} \frac{1}{\pi R^2 Z} \int_0^R \int_0^Z 2\pi r \Omega_{(b,t),P_0} dz dr, \tag{4.113}$$

where by symmetry, $\bar{\Omega}_b = \bar{\Omega}_p$. The quantity Ω_b can be expressed as a function of the nondimensional ratio R/Z, which here we will call ζ. Therefore a new function $\bar{\Omega}(\zeta) = 2\bar{\Omega}_b$ can be evaluated once, and the resulted stored for any simulation. A plot of this function is shown in Figure 4.7. Also shown in this figure is the average solid angle estimated by a ratio of surface areas,

$$\bar{\Omega}_{\text{approx}} = 4\pi \frac{2\pi R^2}{2\pi R^2 + 2\pi RZ} = 4\pi \frac{R}{R+Z} = 4\pi \frac{\zeta}{\zeta+1} \tag{4.114}$$

The radiation lost to the ends and transported to the liner, respectively, are

$$P_{Br\to end} = \frac{\bar{\Omega}}{4\pi} P_{Br}, \tag{4.115}$$

$$P_{Br\to liner} = \frac{4\pi - \bar{\Omega}}{4\pi} P_{Br}. \tag{4.116}$$

For simplicity, it is assumed that the radiation travelling through the liner is either lost to the ends

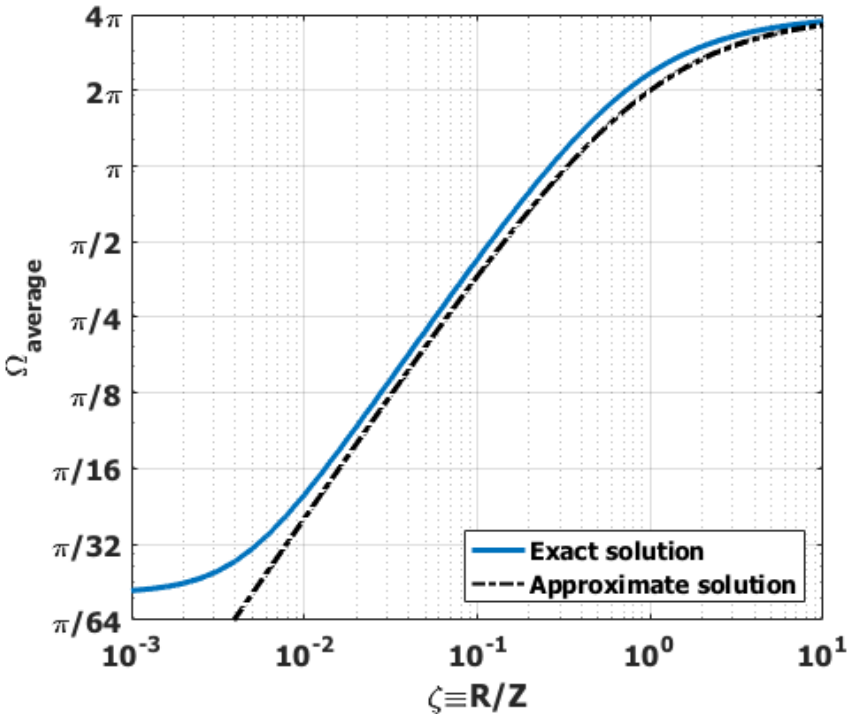

Figure 4.7: The volume-averaged subtended angle of a point in a cylinder by either the top or bottom surface as a function of the non-dimensional coordinate $\zeta = R/Z$. The dashed line is the approximate solution (Eq. 4.114) that is obtained by a ratio of surface areas.

or propagates purely in the radial direction, and that it is approximately described by the ratio of surface areas of the annular liner:

$$P_{Br\rightarrow liner,lost} = P_{Br,liner}\frac{(r_{N_{LI}}^2 - r_1^2)}{(r_{N_{LI}}^2 - r_1^2) + r_{N_{LI}}h} \tag{4.117}$$

so the actual target radiation that could be absorbed by an optically thick liner is

$$P_{Br,t} = \left[\frac{4\pi - \bar{\Omega}}{4\pi}\frac{r_{N_{LI}}h}{r_{N_{LI}}}\right]P_{Br} \tag{4.118}$$

Radiation production in the liner

To accurately model the radiation originating within the liner, a similar calculation would have to be performed for radiation produced in each shell, which is somewhat cumbersome.

Therefore, two simplifying assumptions are made: first, that the fraction of radiated liner energy lost to the ends is proportional to the sum of the end surface areas to the total surface area,

$$P_{rad,l,lost} = P_{rad,l,total} \frac{r_{N_{LI}}}{r_{N_{LI}} + h} \tag{4.119}$$

The second assumption, like with target radiation, radiation that is not lost to the ends propagates purely in the radial direction.

Radiation transport

Both the liner and target radiation that is not lost to the ends is assumed to propagate radially, with 50% traveling in the $-\hat{r}$ direction, and 50% traveling in the $\hat{r}$ direction. Furthermore, it is assumed that liner radiation originates as a point source at the center of the shell of origin, r_c. Radiation is attenuated (absorbed) according to

$$P_{Br,att} = 0.5 P_{Br,0} \int_{r_c}^{r_{N_{LI}}} e^{-r/\lambda(r)} dr + 0.5 P_{Br,0} \int_{r_c}^{-r_{N_{LI}}} e^{-r/\lambda(r)} dr \tag{4.120}$$

It is assumed that absorption is due to inverse bremsstrahlung and $\lambda(r) \equiv (\chi_{Ross}\rho)^{-1}$ is the photon mean free path, where χ_{Ross} is the Rosseland mean opacity of a particular shell. Target radiation is transported in a similar fashion, except it all propagates in the $\hat{r}$ direction, and originates at r_1. Furthermore, liner radiation propagates freely through the target, which is almost always optically thin. Rosseland mean opacities and photon mean free paths were obtained in tabular form from PrOpacEOS simulations, and as with ionization level and radiation cooling, formulaic approximations were made, shown here in Fig. 4.8, with details provided in Appendix C of [100].

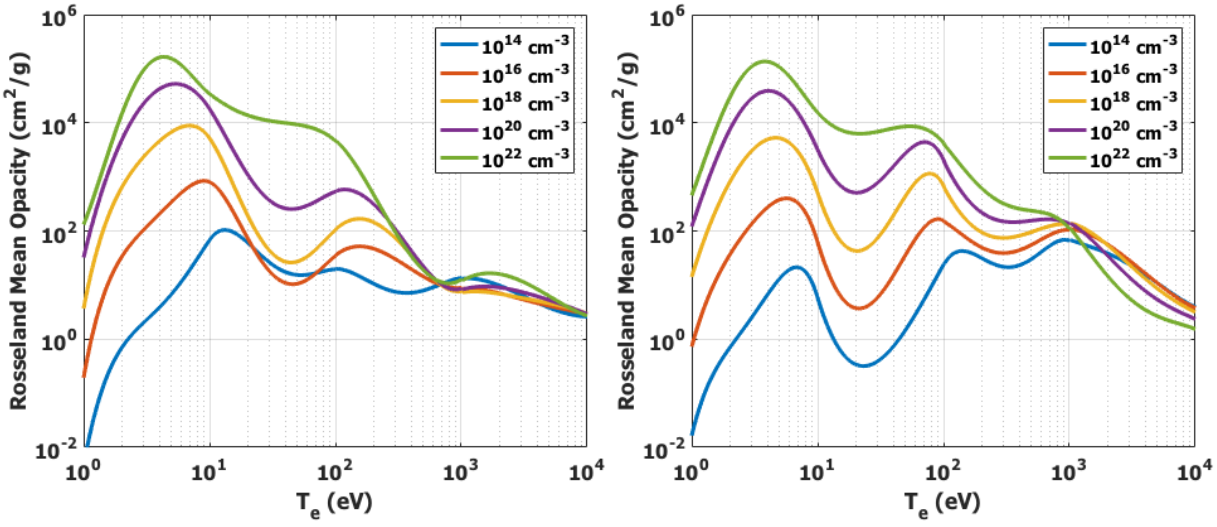

Figure 4.8: Rosseland mean opacities for argon (left) and krypton (right) for $n_i = 10^{14}$, 10^{16}, 10^{18}, 10^{20}, 10^{22} cm^{-3} as functions of temperature. These are formulaic approximations that have been fit to match with PrOpacEOS simulations. See Appendix C of [100] for details.

4.3 Model testing

The model developed in the previous section contains the relevant sets of physics to model a single-liner SZP implosion in 1-D. In order to have confidence in the predictions of the model, it should be demonstrated that the model reasonably captures the behavior of more detailed, 1-D radiation MHD simulations. Toward this end, two sample problems are considered. First, the dynamics of an Ar/D implosion on the Zebra ($\sim$ 1 MA, 100 ns) driver with initial conditions comparable to those used in recent experiments [54, 105] are modeled and compared with a 1-D HYDRA simulation. Second, the dynamics of a MagLIF-type implosion with initial conditions comparable to the point design [15] are compared between this model and SAMM.

The goal in comparing these two problems is not to reproduce the results exactly. Rather, it is to obtain high-level agreement in the important relevant parameters, e.g. implosion time, final target radius and temperature, and neutron yield. These two problems were chosen because they are (a) experimentally achievable and (b) occupy the upper and lower limits of what is

currently feasible for near-future SZP implosions. Furthermore, reasonable agreement between this model and SAMM for the MagLIF problem would give us some confidence that the changes implemented to the code to account for physics relevant to gas-puff implosions do not prevent the model from recovering the results of SAMM.

4.3.1 1-MA Zebra SZP test problem

The first test problem is an argon liner on deuterium SZP implosion on the 1-MA Zebra driver. The liner has mass-per-unit-length (M/L) of 12 μg/cm and FWHM 7 mm, centered at r = 1.3 cm, and the target is deuterium with M/L 2 μg/cm centered on axis. The initial axial magnetic field is 0.15 T. These initial conditions are comparable to those used in recent experiments.

Implosion dynamics are compared between the model and HYDRA simulations by comparing the temporal evolution of three characteristic radii: the radius of the shock front, the radius of the target, and the radius of the liner. Extracting these quantities is straightforward in our model because they are explicitly solved for at each timestep: they are r_{SF}, r_1, and $r_{N_{LI}}$, respectively. Extracting this information from HYDRA or any other multi-material MHD code is straightforward for the target radius, but requires some effort to obtain the other two.

Obtaining the target radius is straightforward in these simulations because there is a cell quantity that dictates the material comprising the fluid in the cell. In MACH2 this parameter is called "conimat," so for example, regions where conimat= 1 would describe the target, and regions where conimat= 2 would describe the liner. If the simulation is either Eulerian or arbitrary-Lagrangian-Eulerian (ALE), then there can also be mixed cells. In these cells, the mass (or number density) fractions are indicated by an interpolation in the material specification parameter. For example, if conimat=1 is deuterium and conimat=2 is argon, then conimat=1.75 would indicate a cell that is 75% argon and 25% deuterium. So, to obtain target radius in a 1-D simulation at a particular time is as simple as plotting the material specification parameter as a function of radius.

Extracting the location of the shock front in the target is, in theory, also very straightforward. Ideally, there is a single, large, density and pressure discontinuity in the target that denotes the shock front. However, in order to conserve the appropriate quantities and maintain a stable, non-oscillatory solution, the front is diffused over multiple cell widths. The standard approach is called van Leer advection [106], though other models exist. For our purposes, an ad-hoc method is employed to find the shock front. At the base of the shock front, there is typically a local density minimum, due to the initially Gaussian profile of the target. So, the evolution of the shock front is reasonably approximated as the evolution of a particular density minimum. This approach has its limitations, as oscillations in density will obfuscate the location of the front. However, the general trajectory of the shock front is obtained, and for our purposes it is sufficient to manually select the correct minima that reflect the actual location of the shock front, which is easily verified by plotting the density profile of interest.

Extracting the location of the liner radius in a gas-puff Z-pinch first necessarily requires defining the interface between the vacuum and the liner. In a simulation that is not strictly Lagrangian, this interface is not explicitly defined. There is typically a density-floor limit, below which the resistivity is set to a vacuum value - so one approach could be to track the interface between physical resistivity and vacuum resistivity. However, this will tend to overestimate liner radius in a gas-puff Z-pinch because there is a low-density, coronal plasma on the outer surface of the plasma. Another approach is to consider the location of maximum density. This approach only works for gas-puff liners that are significantly snow-plowed. A final approach, which has been used here, is to assume the outer liner radius is the location at which the azimuthal magnetic field is maximum. By definition, the azimuthal magnetic field is highest at $r_{N_{LI}}$, so this is our preferred method. For a qualitative comparison, however, any method is sufficient.

The trajectories of r_{SF}, r_1, and $r_{N_{LI}}$ of the model are compared with the equivalent quantities of a HYDRA simulation in Fig. 4.9. General good agreement is obtained for all three quantities, those there is a time shift of$\sim$ 3 ns.

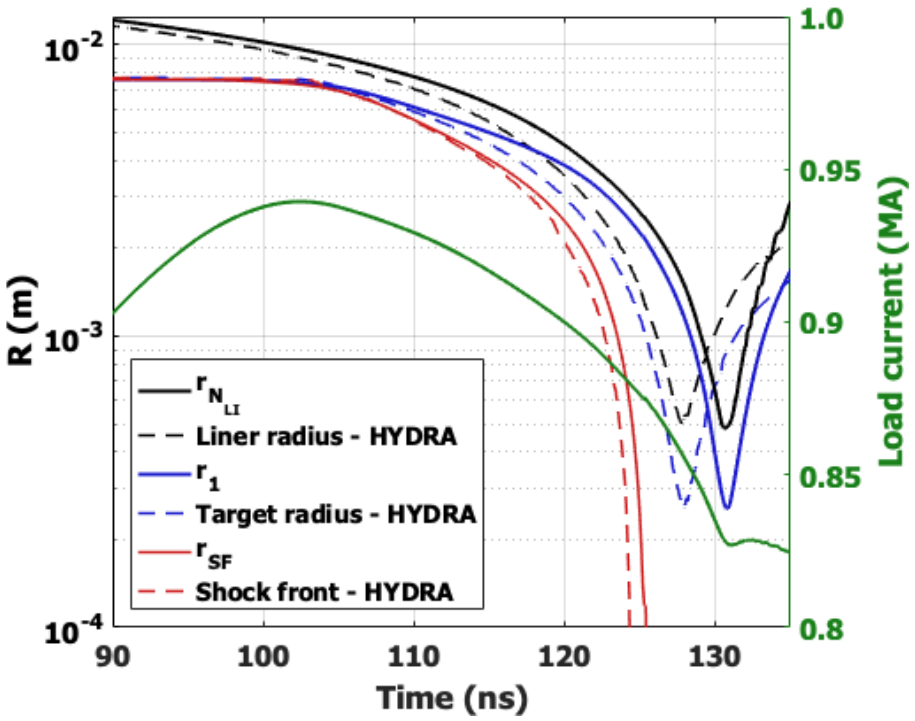

Figure 4.9: Liner and target radii for the 1-MA Zebra test problem. Solid lines are from the model, and dashed lines are from HYDRA simulations. The current trace from the model simulation is overlaid to illustrate that peak compression occurs 30 ns after peak current.

Despite the agreement in front location, there is notable disagreement observed in the evolution of mass-averaged target temperature versus time, shown in Fig. 4.10, even after accounting for the apparent 3-ns shift in implosion time. This can be partially explained by the presence of a thin layer of high-T_i, low density liner plasma that develops between the bulk of the liner and the liner/target radius. In the original simulation of this problem, it was found that this heating corresponded with large values of artificial viscous pressure relative to the plasma pressure in the low-density region. The significant artificial heating is amplified as the bulk of the liner snowplow compresses onto the low-density interior of the liner.

This hypothesis was confirmed by limiting the artificial viscous pressure to 10% of the total plasma load, which saw a marked decrease in the temperature of the low-density plasma region. See, for example, Fig. 4.11, a comparison of p, q, and T_{ion} at 90 ns of identical simulations,

with and without the artificial viscosity limiter.

The development of this layer has a material-dependence, as demonstrated by a comparison between the model and HYDRA of the same Zebra test problem, but the liner material is hydrogen instead of argon. As shown in Fig. 4.12, there still is some disagreement between codes, but much less so than in the Ar/D case. Because the HYDRA code is export-controlled and the source code is not available, it is challenging to investigate whether this anomalous heating is physical and suggests a shortcoming of our model, or it is nonphysical, suggesting that the artificial viscosity model in a low-density plasma (well below the ICF regime) in HYDRA is introducing substantial artificial heating. This is one topic that is left to future work.

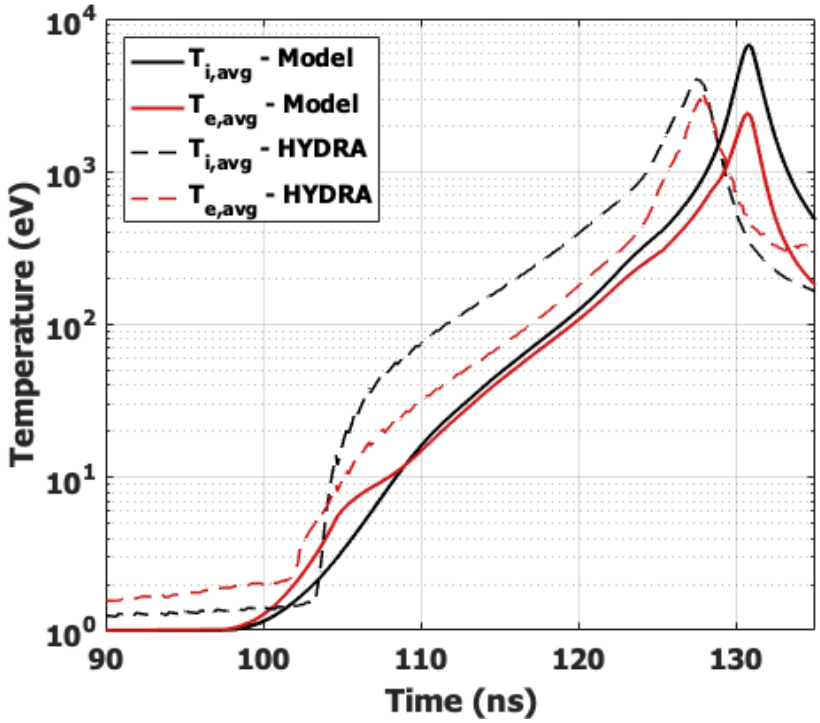

Figure 4.10: Average target ion (solid) and electron (dashed) temperature versus time in the Ar/D Zebra test problem from the model (black) and a 1-D HYDRA simulation (red).

While the final target radii are very similar in the model and HYDRA: 485 μm and 495 μm, peak ion temperatures differed significantly (6.7 keV and 4.0 keV, respectively). Better agreement was found in peak electron temperatures, 3.2 keV and 2.4 keV.

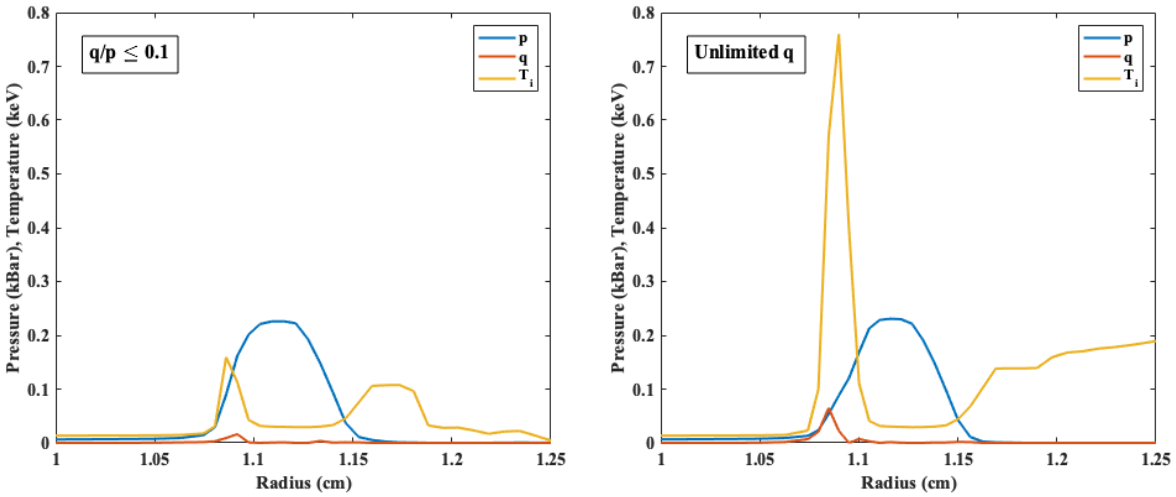

Figure 4.11: Plasma pressure (p), artificial viscous pressure (q), and ion temperature radial profiles at t = 90 ns in the Ar/D Zebra test problem for limited and unlimited artificial viscous pressure. Artificial viscous pressure was limited by preventing the ratio q/p from exceeding 0.1. Note that for the radii shown, only the Ar liner is visible.

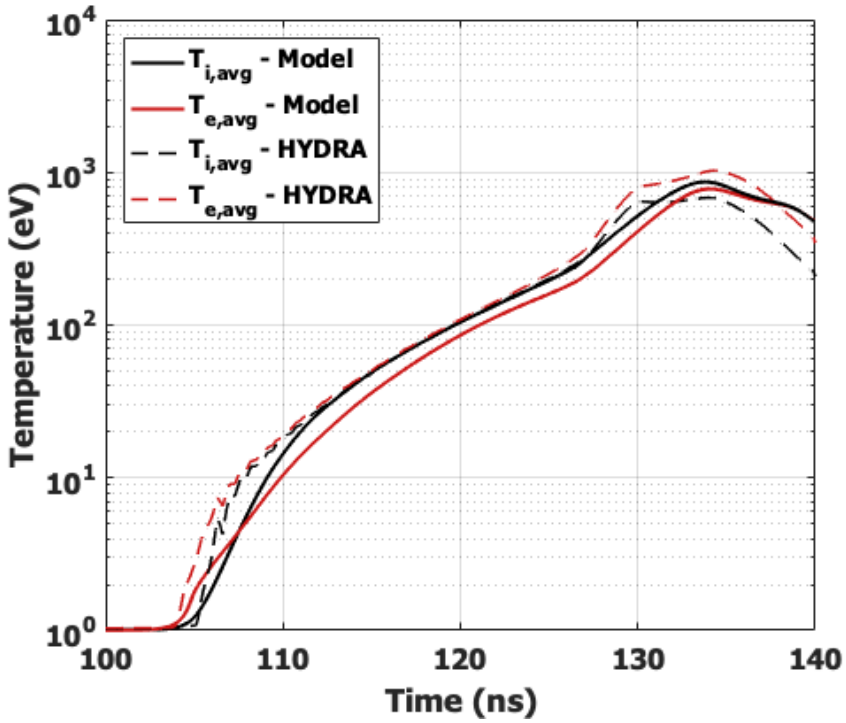

Figure 4.12: Average target ion (solid) and electron (dashed) temperature versus time in the H/D Zebra test problem from the model (black) and a 1-D HYDRA simulation (red).

In the context of magneto-inertial fusion, one of the significant advantages to a semi-analytic model like the one developed here over conventional MHD simulations is that the relevant heating and loss rates are explicitly calculated. This has two advantages - first, as a sanity check, and second, to assist in experimental design via parameter scans. For example, it is particularly useful for the SZP to establish how much energy is provided to the fuel by shock heating, because that is a quantity that is not presently well-established. The energy quantities that provide the temperatures presented in Fig. 4.10 are shown in Fig. 4.13 for ions (left) and electrons (right). In these figures, dashed lines represent net-negative quantities.

As would be expected, shock heating (shown in red) is the dominant target heating mechanism prior to the shock front arriving on axis at $\sim$ 125 ns, after which time adiabatic heating is the dominant mechanism. In this problem, shock preheating provides $\sim$ 40 J of energy to the ions, whereas PdV heating provides the remaining 1 kJ. In terms of fusion-relevant parameters, this is equivalent to shock heating the target to $\sim$ 270 eV (from an initial temperature of 1 eV) and a convergence ratio of $\sim$ 3.5, following by PdV compression to a final temperature of 6.7 keV and an overall convergence ratio of $\sim$ 30.

Target ions can lose their energy by either thermal conduction to the liner or by equilibration with electrons, which are usually colder. However, these losses are insignificant relative to the PdV heating, showing that ions undergo quasi-adiabatic compression after the shock arrives on axis. In the case of target electrons, the predominant heating loss is by thermal conduction. It is well known (e.g. [28]) that at low target density, electron conduction losses exceed radiation losses, and that this reverses at higher densities. Losses by electron thermal conduction are usually (though not always, see e.g. [77]) much higher than ion conduction losses. As an additional sanity check, we see that net losses due to thermal conduction are much higher for than ions - 200 J vs. 5 J, respectively. For completeness, Ohmic heating and byproduct deposition have been include in the plot, but are negligible relative to shock and PdV heating.

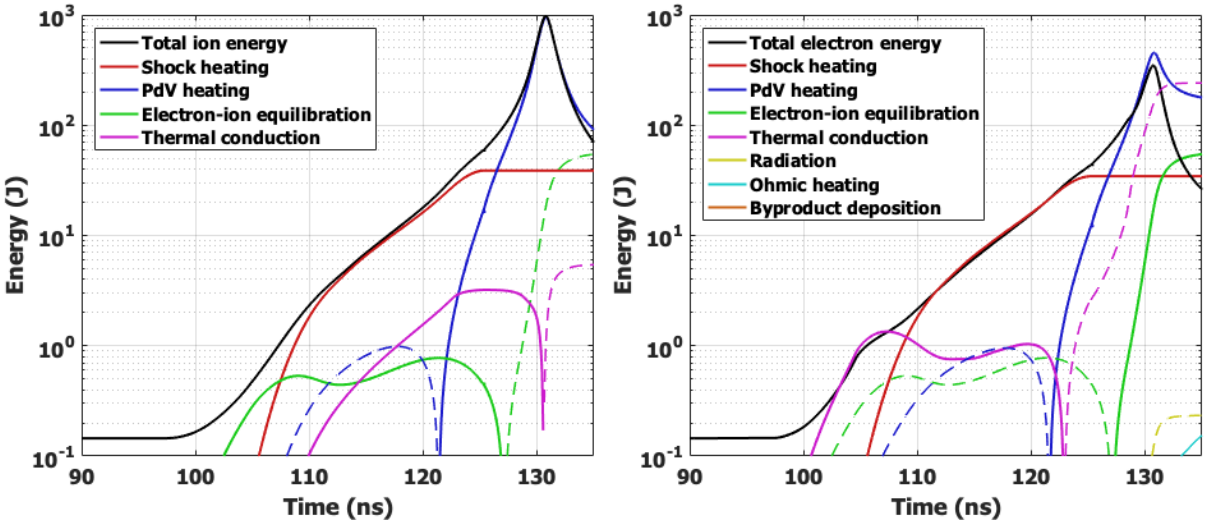

Figure 4.13: Target ion (left) and electron (right) heating for the Ar/D Zebra test problem from t = 90 ns to t = 135 ns. Negative quantities are denoted by dashed lines. The shock front arrives on axis at approximately 125 ns, during which time the dominant heating mechanism transitions to PdV heating.

4.3.2 25-MA Z MagLIF test problem

The second test problem is comparable to the point design of MagLIF on Z [15]. The goal of this test problem is not to reproduce the exact results of SAMM, but rather to demonstrate qualitatively that the changes implemented to SAMM to develop this model do not prevent the model from recovering the original SAMM results. This requires including some additional simple models that are important for MagLIF, but not for a gas-puff SZP.

The original MagLIF point design uses a solid beryllium liner ($\rho_0 = 1850$ kg/m^3). As in SAMM, it is necessary to augment the liner EOS with a cold curve pressure, otherwise the liner will overcompress considerably. The Birch-Murnaghan formula is used, which for shell s has the form

$$p_{0,s} = \frac{3\mathcal{A}_1}{2}\left[\left(\frac{\rho_s}{\rho_0}\right)^{\gamma_1} - \left(\frac{\rho_s}{\rho_0}\right)^{\gamma_2}\right]\left\{1 + \frac{3}{4}\left[\mathcal{A}_2 - 4\right]\left\{\left(\frac{\rho_s}{\rho_0}\right)^{2/3} - 1\right]\right\} \tag{4.121}$$

where, for beryllium, the bulk modulus is $\mathcal{A}_1 = 130$ GPa, $\rho_0 = 1845$ kg/m^3, $\gamma_1 = 1.85$, $\gamma_2 = 1.18$,

and $\mathcal{A}_2 = 3.9993$ [77].

A constant resistivity of 36 nΩm is used, and the circuit and voltage model are modified as described in [77] - approximately 20 MA is delivered to the load in 140 ns. To approximate laser preheating, the target is heated to 200 eV over a 5-ns period, shortly before the liner begins to implode. Because the implosion is subsonic, the shock heating routine is bypassed, and the problem is initialized and run using only the routine for the adiabatic heating phase. End losses (i.e. mass flux) has been included using the same model as SAMM, assuming fully open ends. Mass flux out the ends is important to include in a MagLIF implosion, because by design it is necessary for a laser beam to enter the fuel, heat the fuel, and exit into some sort of reservoir to prevent backscatter. It is implemented by assuming mass flows out due to thermal expansion, i.e. mass flux is approximately the product of target radius and target sound speed.

Fig. 4.14 shows the radial compression, target ion temperature, and load current versus time for the MagLIF test problem, which should be compared with Fig. 1 of [15] and Fig. 4a of [77]. There is good agreement, particularly in the EOM between SAMM and this model. This is to be expected, as they are essentially solving the same equations. The observed yield from this model is 1.2 MJ, which is higher than 1.0 MJ reported in [77] and 0.5 MJ reported in [15], however, it is the same order of magnitude. The increased yield relative to [77] is consistent with greater liner and target compression in the model, with minimum radii of 165 μm and 67 μm, respectively, relative to ~ 100 μm and ~ 325 μm from SAMM.

As in the Zebra problem, ion heating losses are shown in Fig. 4.15. Thermal conduction losses have been significantly mitigated by liner magnetization, those it is important to note that the Nernst effect has not been implemented in this model. Unlike in the Zebra problem, charged particle deposition is the dominant heating mechanism, though much of the heating is lost due to our implementation of end losses. This somewhat agrees with SAMM, c.f. Fig. 4f-4g of [77]. When end losses are neglected, the discrepancy is much larger. In this instance, including charged particle heating increases the total yield by a factor of 4.

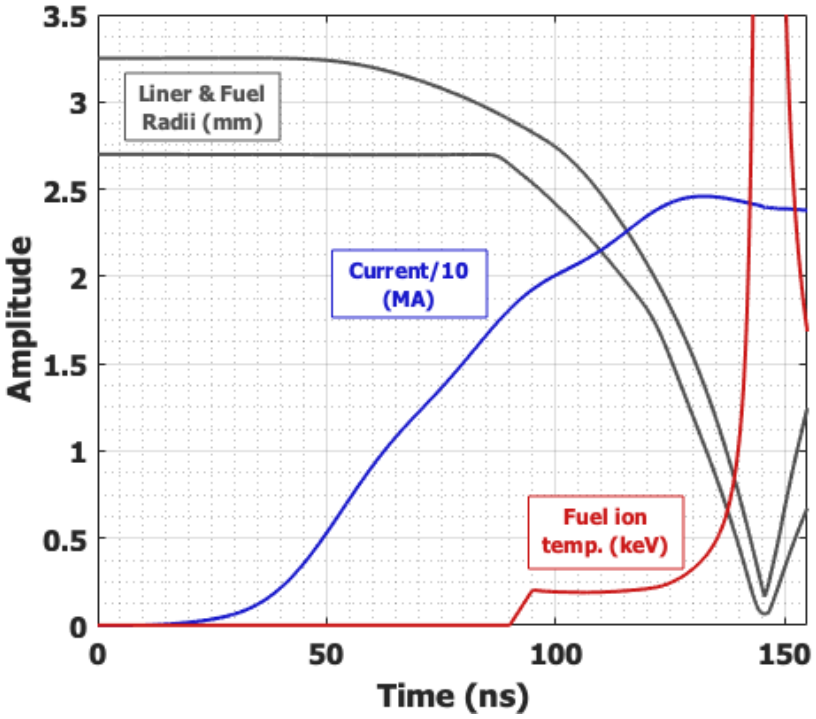

Figure 4.14: Liner and fuel radii (mm), liner current (MA/10), and fuel ion temperature (keV) for the MagLIF test problem, cf. Fig. 1, [15], Fig. 4a, [77].

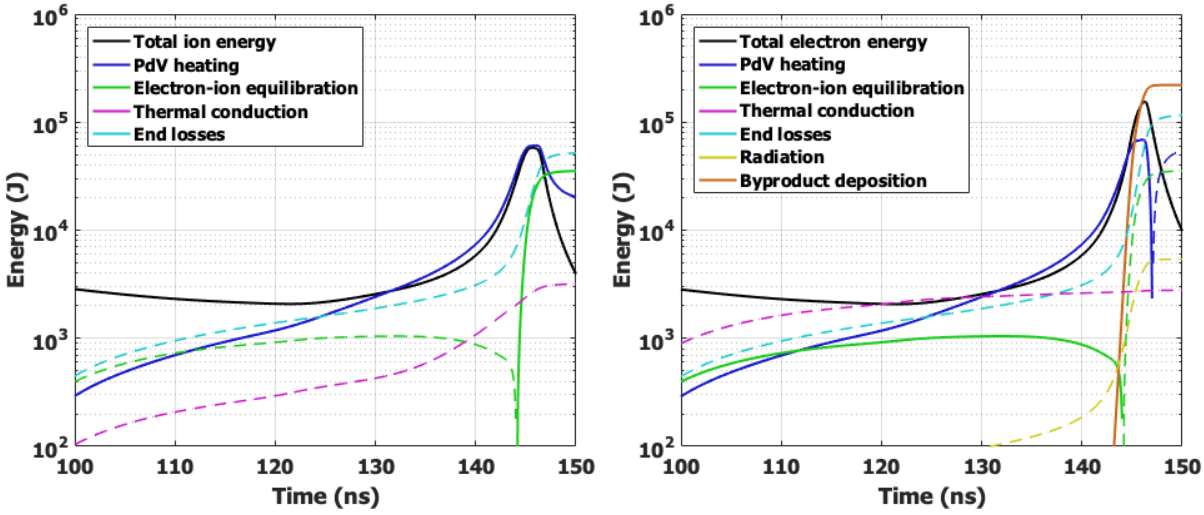

Figure 4.15: Ion and electron heating mechanisms for the MagLIF test problem. Negative quantities (loss terms) are shown as dotted lines.

Given the goal of this problem is not to reproduce the results of SAMM, but to show that the model behaves well for the MagLIF problem, we can proceed with scaling the SZP problem into the multi-MA regime.

4.4 Optimization and scaling for Kr/D SZP on LTD-III

In the previous section, it was shown that the model behaves reasonably well compared to other established models and codes for SZP-type implosions over the relevant density regimes - ranging from university-scale, MA drivers to drivers with peak current in excess of 20 MA. This naturally leads to the two-part question: (a) how can neutron yield be maximized for a certain load geometry on a university-scale driver, and (b) how does that neutron yield scale with peak current? Additionally, it would be useful to test the radiation model qualitatively by investigating whether there is an increase in radiation absorption on higher current machines, which necessary require higher density, more optically-thick liners.

4.4.1 Optimization study

The first objective of this study is to maximize deuterium neutron yield of a Kr/D SZP implosion on the 850-kA linear transformer driver (LTD) at UC San Diego, LTD-III. The circuit delivers approximately 850 kA in 160 ns to a short-circuit load with radius of 1 cm, and is modeled reasonably well as an RLC circuit with $R_0 = 47.5$ mΩ, $L_0 = 19$ nH, $C_0 = 580$ nF, and $V_0 = 200$ kV. To limit the scope of the initial study, the following quantities are held fixed: the load length is 1 cm, the return current radius is 5.974 cm, the target radius is 0.75 cm, and the initial liner radius is 2.25 cm - so that the center is at 1.5 cm. Furthermore, the liner and target geometries are held constant, with FWHM of 7.5 mm for both.

In addition to maximizing neutron yield, the SZP load must be sufficiently robust against MRTI growth. This is difficult to assess in a 1-D simulation, but a reasonable criterion can be

established based on linear growth of a characteristic wavelength. As was shown in the derivation in §2.4, application of an axial magnetic field mitigates MRT growth, and that this affect is greater for shorter wavelengths. The dominant MRT wavelength in SZP simulations tends to be of order 1 mm, with shorter wavelength growth mitigated by B_z (or diffused away, as described in §2.5), and longer wavelengths are unable to grow simply due to the shortness of the pinch. Furthermore, the MRT instability growth rate does not have to be zero, but rather slow enough that it does not disrupt the target heating.

With these observations in mind, the MRTI stability criterion is taken as limiting growth of the $\lambda = 1$ mm mode to $\bar{\gamma} = (10\text{ ns})^{-1}$, i.e. the instability amplitude increases by a factor of e every 10 ns. For a given acceleration and density, there is threshold B_z value that gives this growth rate according to the simple planar growth rate,

$$\gamma_{MRT} = \sqrt{2\pi g/\lambda - (2\pi B_z/\lambda)^2/\mu_0\rho}. \tag{4.122}$$

Solving this expression for B_z, this gives

$$B_z > \sqrt{\frac{\mu_0\rho\lambda^2}{4\pi^2}\left(\frac{2\pi g}{\lambda} - \bar{\gamma}^2\right)} \tag{4.123}$$

Because axial magnetic flux is assumed frozen into the liner, $B_{z0} = B_z A(t)/A_0$, where A is area, this gives a requirement for the initial axial magnetic field for shell s:

$$B_{z0} > \frac{r_{s+1}^2 - r_s^2}{r_{0,s+1}^2 - r_{0,s}^2}\sqrt{\frac{\mu_0\rho_s\lambda^2}{4\pi^2}\left(\frac{2\pi\ddot{r}_{s+1}}{\lambda} - \bar{\gamma}^2\right)} \tag{4.124}$$

Unless artificial viscosity is very large, there are high-frequency oscillations in the temporal profiles of the interface velocities, so to estimate acceleration, a fourth-order polynomial fit is performed on $r_{N_{LI}}(t)$, which gives a parabolic approximation for acceleration versus time. The acceleration of internal interfaces is approximated by scaling the polynomial fit self-similarly,

which does not capture the initial snowplow acceleration very well, but does agree well with the interface EOMs closer to peak compression, when MRT growth is the highest.

The threshold $B_{z,0}$ for a particular simulation is then simply the maximum required B_{z0} value over all interfaces and all time. To consider this properly, one would have to perform an N_{LS}-interface MRTI growth analysis of the form of the derivation in §2.4, which would be quite tedious and beyond the scope of this simple design study. Ideally, one would conduct 2-D and 3-D simulations of the point design to determine the validity of the MRTI stability criterion. It is particularly important to conduct 3-D simulations, because axial pre-magnetization does not mitigate $m = 1$ growth.

Thus far, there are three free parameters, liner mass, target mass, and degree of axial pre-magnetization. For simplicity, this initial study will assume that $B_{z,0} = 0.2$ T, and constrain the point design to configurations in which the threshold $B_{z,0}$ is at or below this value. This then leaves the liner mass and target mass as the parameters over which to scan. For a given vacuum magnetic field, the acceleration and the threshold B_{z0} values are higher for undermassed loads and lower for overmassed loads. However, the machine inductance is small, so load inductance can significantly alter the load current profile and therefore the acceleration and threshold B_{z0}.

Another important limit to consider is target convergence ratio (CR). Although higher values have been reported and could be attainable, the conventional upper limit for CR for cylindrical fusion targets is $\sim$30, e.g. [107], so that is also the value taken here.

Fig. 4.16 summarizes the results of the parameter scan, plotting the threshold B_{z0}, neutron yield, and convergence ratio as a function of liner mass and target mass. For this scan, liner masses ranging from 3-24 μg/cm were considered in increments of 1 μg/cm, and target masses ranging from 0.5-5 μg/cm were considered, in increments of 0.5 μg/cm. First, consider the threshold B_{z0} contour. The greatest MRT growth tends to occur closes to stagnation, when acceleration is largest. As intuition might suggest, the undermassed loads generally undergo higher acceleration, where as overmassed loads tend to be slower. It is interesting to note that this is only true when

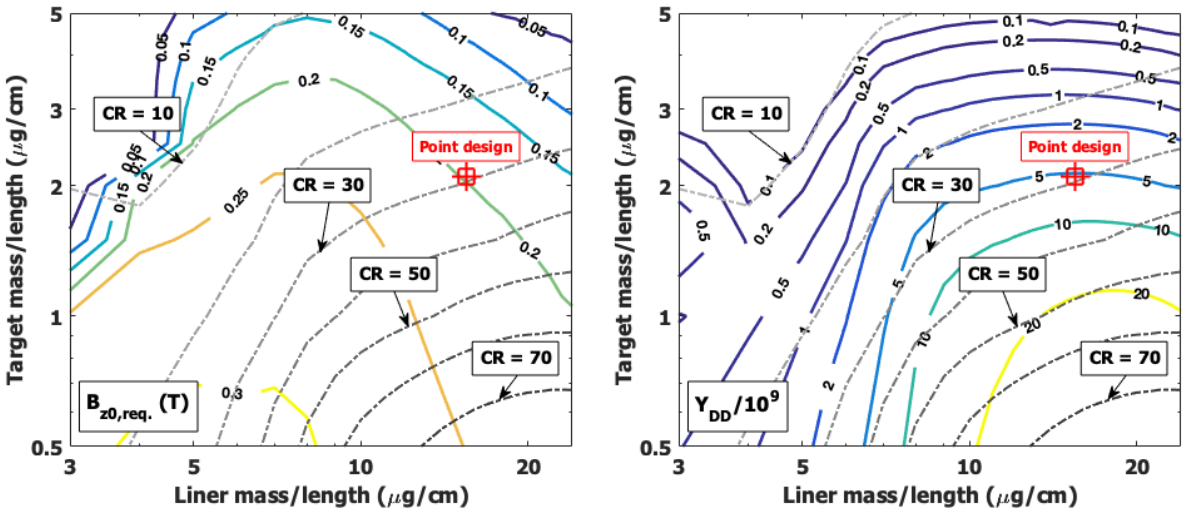

Figure 4.16: (left) Threshold magnetic field values for limiting the instantaneous linear growth rate of the $\lambda = 1$ mm, $(m = 0)$ mode to $(10\text{ ns})^{-1}$ on any interface and (right) DD neutron yield for the LTD test problem as a function of liner and target M/L. Target convergence ratio is overlaid in increments of 10. The selected point design of 15.5 μg/cm liner and 2.1 μg/cm target is also shown.

the liner mass is larger than the load mass. When the load is overmassed, its compression is reduced and the liner does not undergo the rapid acceleration that occurs at high CRs.

Second, consider the yield as a function of liner and target mass. Because this is a 1-D simulation, there is no strict upper limit on target CR, so undermassed targets confined by overmassed liners will reach very high CR - in excess of 70. Though losses will be higher, greater yield with higher CR is not a surprising result.

The constraints of maximum yield, $CR \leq 30$, and threshold $B_{z0} \leq 0.2$ leads to the point design shown in Fig. 4.16: liner mass 15.5 μg/cm and target mass 2.1 μg/cm. The other parameters, including $B_{z0} = 0.2$, complete the specification for the point design.

4.4.2 Scaling study

With the point design selected, it is now of interest to investigate how the results change for larger current drivers. In order to this, we hold all circuit parameters constant except for the

charging voltage, which scales linearly with peak current. Since 200 kV delivers approximately 850 kA to the load, 235 kV delivers 1 MA and 2.35 MV delivers 10 MA. This is likely not practical in an actual experiment, but redesigning an appropriate at each current level is beyond the scope of this initial study.

In addition to scaling the driver, it is also necessary to properly scale the load so that the dynamics remain comparable. For simplicity, we will assume the same load geometry - in practice it might be necessary to redesign an injector system that would create the desired profile, but again this is beyond the scope of this work. To ensure the dynamics are relatively unchanged, consider that the vacuum $\mathbf{J} \times \mathbf{B}$ force is $\mu_0 I^2/8\pi r^2$ - to maintain the approximate same acceleration, liner and target density must be scaled as V^2 (I^2). With other parameters held constant, Eq. 4.123 shows that $B_z \propto \rho^2$, so it is necessary to scale B_{z0} linearly with V (I) to maintain approximately the same level of MRTI mitigation.

There are two objectives of the scaling study. First, the model should qualitatively capture the increasing optical thickness of the liner as the liner density increases. This should occur during an implosion as the liner converges on axis, and as the initial density is scaled on higher current drivers. The first hypothesis is tested by plotting the emitted liner and target radiation as functions of time for a particular configuration, and compare those quantities with the radiation that is absorbed by the liners. This is shown in Fig. 4.17 for the point design at the original scale. Prior to shock arrival on axis, the liner reabsorbs $\sim 1\%$ of the total emitted radiation. As the liner converges on axis, it becomes optically thick, absorbing in excess of 70% of the total emitted radiation. This confirms our hypothesis that the liner does transition from optically thin to optically thick at peak compression, demonstrating the need for MHD simulations of SZP implosions to have the capability to properly treat radiation in both limits.

The second hypothesis, namely that the liner should become optically thick at higher densities, is evaluated by considering the ratio of emitted to absorbed radiation at a characteristic time in the implosion. Since it is convenient to extract, we chose to consider the radiation

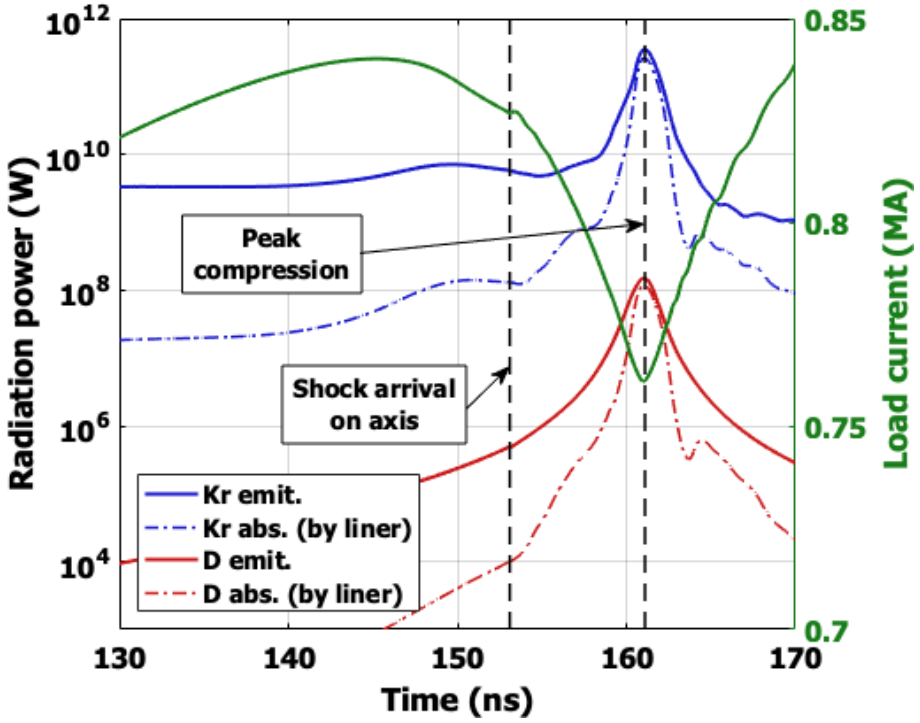

Figure 4.17: Temporal evolution of target (D) and liner (Kr) radiation emission (solid) and absorption (dotted) for the LTD point design. Because the liner is assumed optically thin, absorption refers to absorption by the liner, regardless of origin.

absorption fraction at peak compression. Since the liner absorbs a significant fraction of radiation at this time in the unscaled simulation, it is also useful to consider how this fraction changes at an earlier time, when the liner is still optically thin. Again for convenience, this earlier time is selected as the time of shock arrival on axis. As shown in Fig. 4.18, as the design is scaled to higher densities, the initial values of 1 and 70% increase to $\gtrsim 60\%$ and $\gtrsim 90\%$, respectively.

Finally, it is particularly useful to consider how the neutron yield of a fusion concept scales with peak current. Fig. 4.19 shows the neutron yield scaling with peak current for the point design up to peak currents of ~ 20 MA. This scaling is compared with 1-D HYDRA simulations of the point design where the peak current has been scaled to 1, 2, 5, 7, and 10 MA. There is a near order of magnitude difference in yield at lower densities near the original point design. This is qualitatively consistent with the simulation from the Zebra problem, in which

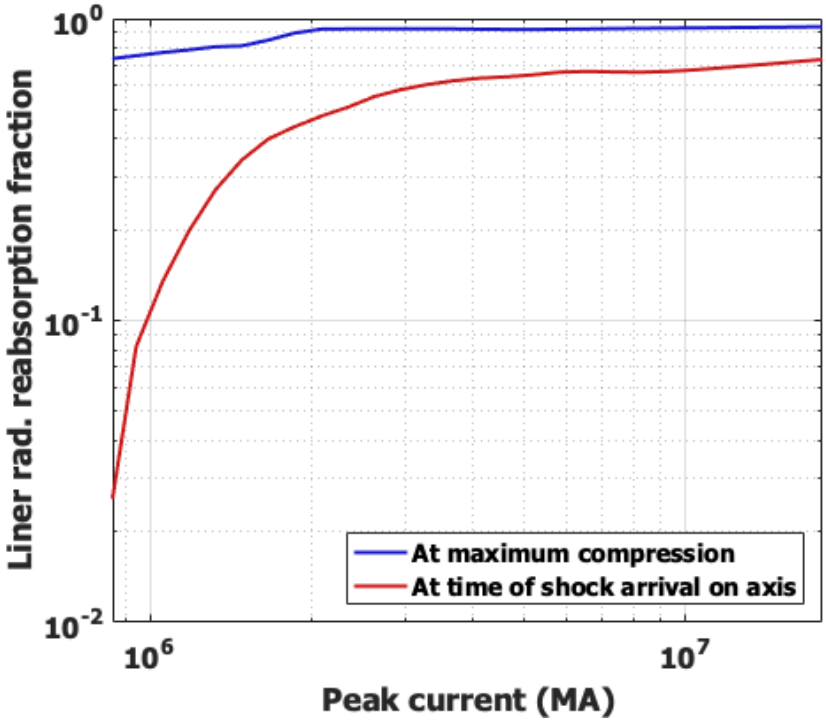

Figure 4.18: The fraction of emitted liner radiation that is reabsorbed as a function of liner peak current at two times at the time of shock arrival on axis, and at the time of peak compression.

higher ion peak temperatures by nearly a factor of 2 were predicted by the model relative to the HYDRA simulation. However, agreement improves considerably at higher peak currents, beginning with the 2 MA simulation. In addition, other models from the literature are included for comparison [21, 23, 108]. These models are for deuterium pinches, which may be more likely to produce yield from beam-target effects rather than from thermonuclear fusion - particularly at lower currents. However the conventional I^4 scaling with peak current is independent of the origin of the neutrons [109].

4.5 Conclusion

In this chapter, a semi-analytic model for SZP-like magneto-inertial fusion based on SAMM [77] is presented. While similar in many aspects, there are key modifications made to

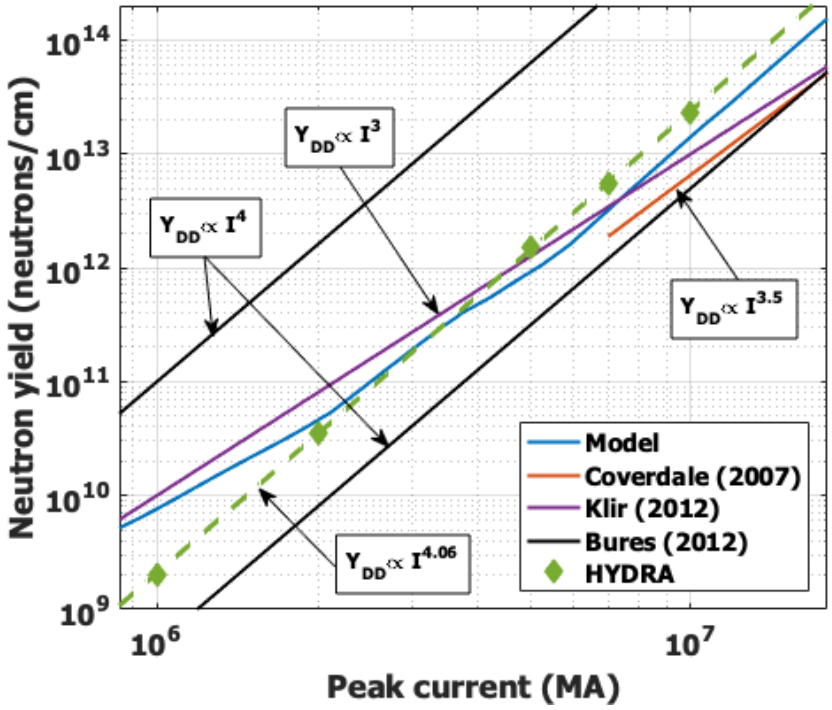

Figure 4.19: Y_{DD} scaling as a function of peak current for the LTD test problem from the original point design up to $\sim$ 20 MA. HYDRA simulations at 1, 2, 5, 7, and 10 MA of the same problem are indicated by the green diamonds, and solid lines are empirical scaling laws for DD neutron yield found in the literature.

the model to account for the different set of physics in a SZP implosion: namely, magnetic field diffusion, separate ion and electron heating and conduction, shock heating of the target/fuel, and radiation transport that transitions from the optically thin to the optically thick regime.

The model is tested in two different regimes: first an SZP implosion on the Zebra (1-MA, 100 ns) driver is compared with an identical simulation using the radiation-MHD code HYDRA. While the implosion dynamics were consistent, there was non-negligible disagreement in the final peak ion temperature. It was demonstrated that in the HYDRA simulation, that this was affected in part by the implementation of artificial viscosity in the liner. Due to this observation, future work will include similar comparisons with other codes, and, provided more access to the code, a more detailed investigation of artificial viscosity in the HYDRA code.

The second test problem was a MagLIF-type implosion comparable to the original point

design [15]. The goal of this study was to demonstrate qualitative agreement in the implosion dynamics and final yield relative to the results in the original paper, and, more particularly, to the results presented in SAMM. The justification for this test problem is to demonstrate that the changes implemented in this model do not prevent us from, at a high-level, recovering the original results of SAMM. For example, the electron-ion equilibration time in the liner should be low enough in MagLIF that having separate ion and electron temperatures is inconsequential.

Finally, a two-part design study was conducted for an SZP-type load on LTD-III (850 kA, 160 ns). In the first part of the study, DD neutron yield was optimized for a specified load geometry and initial axial magnetic field by varying liner and target mass per unit length. A point design was selected that satisfied three constraints: maximum neutron yield, robustness against MRTI growth, and target CR at or below the maximum allowable value. In the second part of the study, it was shown that the model qualitatively captures the transition of the liner from optically thin to optically thick, both during a single implosion, and as the design is scaled to higher current drivers. Furthermore, it was shown that the presented model predicts neutron yield scaling of the point design that is both consistent with 1-D HYDRA simulations and other reported scaling models in the literature.

Future iterations of this model will include the effects of axial magnetic flux loss, both by diffusion and by the Nernst effect. These effects are not particularly relevant for university-scale machines, but are significant in MagLIF-type problems. This will likely include rewriting the model so that it functions as a standalone code, due to the inherent limitations of using the built-in ode solvers in MATLAB. Future work will also assess the degree to which our simplified MRT stabilization criterion predicts 2-D and 3-D stability in full-fledged radiation-MHD simulations.

4.6 Acknowledgments

Chapter 4, in part, contains material as it appears in “A semi-analytic model of gas-puff liner-on-target magneto-inertial fusion”, J. Narkis, H. U. Rahman, J. C. Valenzuela, F. Conti, R. D. McBride, D. Venosa, and F. N. Beg, Phys. Plasmas **26**, 032708 (2019). J. Narkis was the primary author of this paper.

Chapter 5

Dynamics and MRT growth of magnetized and double liner-on-target Z-pinch implosions

5.1 Introduction

In the third chapter, it was shown that in the case of a single liner-on-target, gas-puff Z-pinch that diffusion of azimuthal magnetic field through the liner affected both the dynamics and magneto-Rayleigh-Taylor instability growth. It was found that the overall shock heating of an SZP-like load is predominantly governed by liner inertia, and that there was some, but insufficient mitigation due to material resistivity. In the previous chapter, a simple estimate of MRT growth by axial premagnetization was made in the SZP optimization scaling study on the UC San Diego LTD. Additional, experimental and computational studies in the literature on the mitigation of MRT growth demonstrate that using a tailored density profile, or more practically for SZP-like loads, a double liner configuration, has been shown to substantially mitigate MRT growth. These observations provide substantial motivation for extending the study

of implosion dynamics, namely shock heating, and MRT mitigation, of liner-on-target gas-puff Z-pinches to include loads that have varying degrees of axial premagnetization, loads with a double liner-on-target geometry, and loads with both features.

The simulations presented in this chapter are conducted with the HYDRA radiation-MHD code, rather than with the MHD code MACH2. The difficulty with HYDRA is highlighted in the previous chapter in §4.3.1, in which it was shown that the artificial viscosity model can introduce excessive anomalous heating in low-density regions. However, there are multiple approaches that can be used to circumvent this heating. The challenge in MACH2 occurs when the axial premagnetization is present. Unlike in HYDRA and other MHD codes, MACH2 does not solve the magnetic field using a vector potential.

The equations that are solved are largely the same, but each has its challenges in modeling university-scale gas-puff Z-pinches. In the case of MACH2, the code as currently written solves the magnetic diffusion equation directly, rather than the vector potential, so the solenoidal constraint $\nabla \cdot \mathbf{B} = 0$ is not identically satisfied. The vector potential $\mathbf{A}$ is defined as

$$\mathbf{B} = \nabla \times \mathbf{A}, \tag{5.1}$$

$$\frac{\partial \mathbf{A}}{\partial t} = -\mathbf{E} - \nabla \phi \tag{5.2}$$

so by default $\nabla \cdot \mathbf{B} = 0$ since the divergence of a curl is zero. To reduce the divergence of $\mathbf{B}$, MACH2 employs a subroutine that adds a potential ϕ such that

$$\mathbf{B}_{\text{new}} = \mathbf{B}_{\text{old}} + \nabla \phi, \tag{5.3}$$

$$\nabla^2 \phi = -\nabla \cdot \mathbf{B}_{\text{old}}, \tag{5.4}$$

$$\nabla \cdot \mathbf{B}_{\text{new}} = 0. \tag{5.5}$$

It has been observed that disabling this routine renders the simulations unstable, and that employ-

ing the routine in two-dimensional simulations tends to add axial magnetic flux to the simulation. This is problematic when considering MRT instability mitigation by axial magnetic field because it may overestimate the values of $\mathbf{B}_z$ on the surface of the liner, which could overestimate the amount of mitigation observed.

There are of course, other considerations that we are neglecting due to computational limitations in either code. First, the geometry of the simulations does not extend into 3-D. This means that the present study does not address instability growth for modes $m > 0$. Second, it has been hypothesized that certain effects that manifest in low-density plasma like the helical perturbations in MagLIF [70] require extended-MHD physics, which are not included in the work presented here. However, the $m = 0$ MRT instability tends to grow faster than $m > 0$ [59] and an axial magnetic field tends not to stabilize the $m = 1$ MRT instability [84], so for our purposes 2-D simulations will suffice. This should be confirmed in future 3-D HYDRA simulations.

5.2 MRT growth mitigation by axial magnetic field in single-liner implosions

5.2.1 With no axial magnetic field

It was shown in Chapter 3 that MRT instability growth could be somewhat mitigated in identically massed loads by increasing the atomic number of the liner material. Because the implosion trajectory and initial perturbation was the same among the configurations, the observed decrease in sub-mm mode growth was attributed to liner material properties, namely resistivity. However, the acceleration of a gas-puff SZP load is typically too large for that mechanism to stabilize the pinch alone. If an axial magnetic field is present, tension in the field lines can reduce instability growth. If the plasma can be described by ideal MHD equilibrium, it was shown in §2.4 that, assuming the liner has constant density and no target is present, growth of the most

unstable MRTI mode is represented by

$$\omega^2 = \left(\frac{(\mathbf{k}\cdot\mathbf{B}_{0l})^2}{\mu_0\rho_0} + \frac{(\mathbf{k}\cdot\mathbf{B}_{0v})^2}{2\mu_0\rho_0}\coth(2ka) \right) - \left(\left[\frac{(\mathbf{k}\cdot\mathbf{B}_{0v})^2}{2\mu_0\rho_0}\coth(2ka) \right]^2 + (gk)^2 - gk\frac{(\mathbf{k}\cdot\mathbf{B}_{0v})^2}{\mu_0\rho_0} \right)^{1/2} \quad (5.6)$$

where, because we are considering the $m = 0$ modes, $\mathbf{k}\cdot\mathbf{B} = kB_z$ and a is the liner thickness. Recall that $\xi \propto \exp(i\omega t)$, so modes are unstable when $\omega^2 < 0$. If $B_{0v} = 0$, this reduces to the familiar growth rate ($\gamma \equiv i\omega$),

$$\gamma^2 = \left(gk_z - \frac{(k_z B_z)^2}{\mu_0\rho_0} \right)$$

that was used for the simple MRT stability criterion in Chapter 4. If no axial magnetic field is present, the growth rate is the classical RT growth rate, $\gamma = \sqrt{gk_z}$.

In this section, the implosion of a Ne/D gas-puff SZP target is considered using the same circuit parameters as outlined in §4.4: an RLC circuit with $R_0 = 47.5$ mΩ, $L_0 = 19$ nH, $C_0 = 580$ nF, and $V_0 = 200$ kV. The target is centered on axis with FWHM 1 cm and peak density 10^{-3} kg/m^3, and the liner is centered at 2.5 cm, with FWHM 0.5 cm and peak density 10^{-3} kg/m^{-3}. As in Chapter 3, an axial resolution of 100 μm is used and a $\pm 1\%$ density perturbation is used to seed instability growth. The initial test problem will have zero axial magnetic field to establish whether the instability growth can be adequately predicted using classical planar RT growth estimates.

MRT growth is negligible through 130 ns, as shown by the density contours in Fig. 5.1. Here the red lines indicate the liner radius as a function of axial position as determined by a cutoff density of 10^{15} cm^{-3}, or 3×10^{-5} kg/m^3 for Ne. The corresponding discrete Fourier transforms are shown for 140, 150, and 160 ns in Fig. 5.2. Again, they are shown as functions of wavelength rather than wavenumber. Wavelengths under 1 mm do not grow significantly, and a dominant wavelength of 1.667 mm has emerged by 150 ns.

It is useful to assume that the WKBJ approximation is applicable, i.e., that each mode

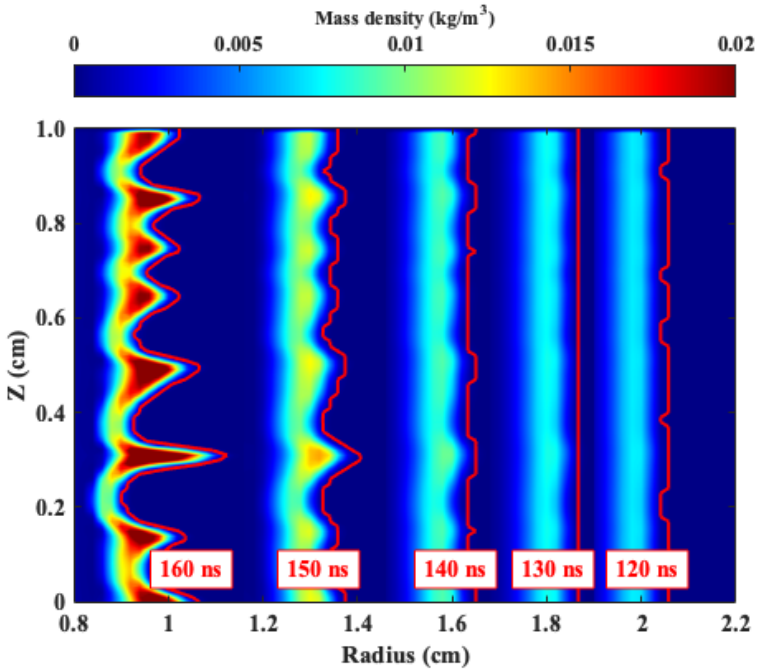

Figure 5.1: 2-D mass density contours for the Ne/D LTD problem with $B_{z0} = 0$ T from 120-160 ns. The red overlays indicate the liner radius as determined by a cutoff density of 10^{15} cm^{-3}.

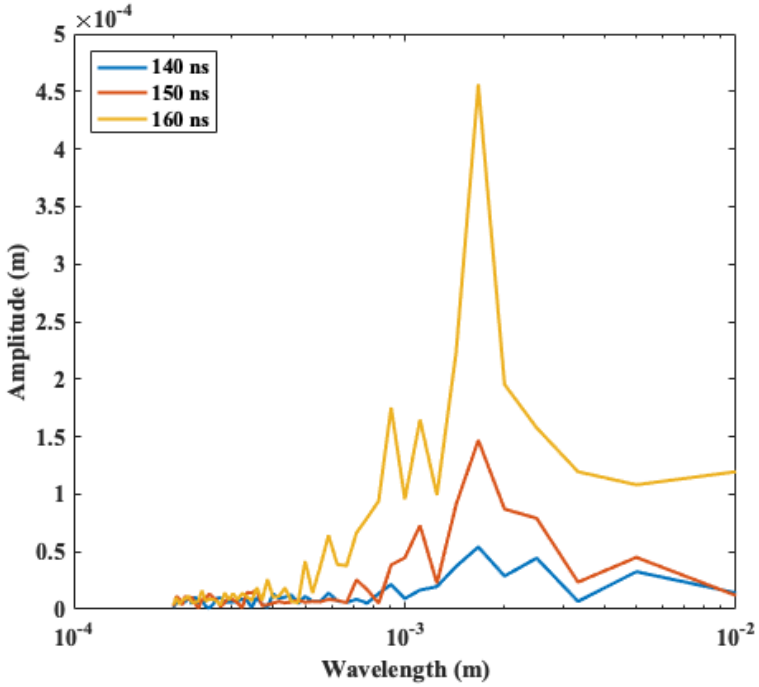

Figure 5.2: Discrete Fourier transform of the outer liner surface as a function of axial position at 140, 150, and 160 ns for the Ne/D LTD problem with $B_{z0} = 0$ T.

evolves independently of the others according to its instantaneous growth rate,

$$\Gamma(\lambda, t) = e^{\int_{t_0}^{t} \gamma(\lambda,\tau) d\tau} \tag{5.7}$$

because this allows us to consider the growth of a particular mode over time. Here the dominant mode, $\lambda = 1.667$ mm is of interest. The amplitude of this mode over the time period 130 ns to 170 ns is shown in Fig. 5.3, and it is compared with two growth estimates. To obtain these estimates, a fourth-order polynomial fit is applied to the temporal profile of radius, where the axially-averaged liner radius is used. The acceleration is quadratic in time, and Eq. 5.7 is invoked with $t_0 = 130$ ns to give the amplitude. The function is multiplied by a constant value such that the simulated and theoretical amplitudes are equal at 150 ns.

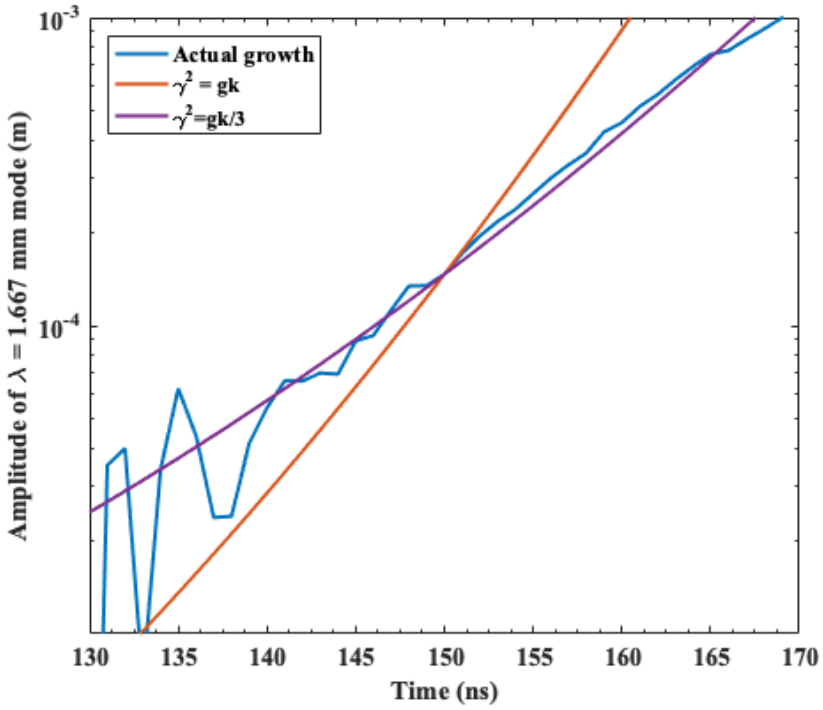

Figure 5.3: Amplitude of the $\lambda = 1.667$ mm MRT mode as a function of time for the Ne/D LTD problem with $B_{z0} = 0$ T. Also shown are the growth rates assuming $\gamma = \sqrt{gk}$ and $\gamma/\sqrt{3}$, where the amplitudes have been adjusted to match with the observed amplitude at 150 ns.

The classical MRT growth rate overestimates the observed growth rate of the $\lambda = 1.667$

mm mode in simulation by a factor of 1.6-1.7, as shown by the curve $\gamma^2 = gk/3$. The growth rate of other modes in the 1-2 mm range is overestimated by a factor of (approximately) $\sqrt{6}$, $\sqrt{4.5}$, $\sqrt{3}$, 2, and $\sqrt{3}.25$ for the 1, 1.111, 1.25, 1.429, and 2 mm modes, respectively, shown in Fig. 5.4. The greater overestimate of MRT growth suggests there is some sort of nonideal MRT mitigation mechanism that is not accounted for in obtaining the classical growth rate. One possibility could be that, due to the diffuse density profile, there is not a sharp boundary between the vacuum and the liner. This could result in an effective non-zero Atwood number, which would lower the growth rate. However, there is a wavelength dependence on the overestimate of MRT growth that would not be accounted for by introducing an effective Atwood number.

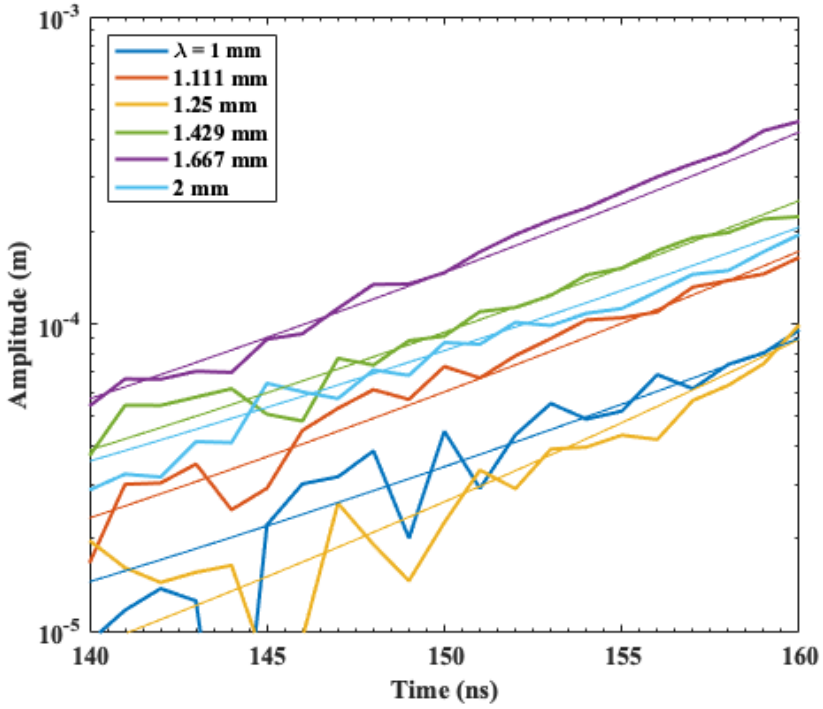

Figure 5.4: Amplitudes of the $\lambda = 1-2$ mm MRT mode as a function of time for the Ne/D LTD problem with $B_{z0} = 0$ T. Also shown are the growth rates assuming $\gamma = \sqrt{gk/S}$, where $S = 6, 4.5, 3, 4, 3$, and 3.25 for $\lambda = 1, 1.111, 1.25, 1.429, 1.667$, and 2 mm, respectively. The initial amplitudes of each fit curve have been adjusted so that amplitudes at 150 ns approximately match those observed in simulation.

A more plausible explanation is that non-ideal, i.e. resistive effects provide some degree

of growth mitigation of the 1-2 mm wavelength modes. The effective minimum allowable wavelength, according to the estimate in Eq. 2.58, is approximately 525-660μm at 160 ns, noting resistivity is approximately 3×10^{-5} Ωm inside the liner and acceleration is approximately 10^{13} m/s^2. Resistivity is higher on the surface of the liner, and increases rapidly into the vacuum. It would be useful to verify this sub-classical MRT growth in a future experiment.

5.2.2 With axial magnetic field

The inclusion of an axial magnetic field can reduce MRT growth on both the inner and outer surfaces of the liner. Even though, in this test problem, the target mass on the inner surface of the liner is negligible, the axial magnetic field is snowplow-compressed ahead of the liner. The solution presented in §2.4 assumes there is no field ahead of the liner. To account for this field, $\mathbf{B}_{0t}$, the equation at $x = a$ is modified to give

$$\xi^+\left(gk\rho_0+\frac{(\mathbf{k}\cdot\mathbf{B}_{0t})^2}{\mu_0}+\left[-\rho_0\omega^2+\frac{(\mathbf{k}\cdot\mathbf{B}_{0l})^2}{\mu_0}\right]\coth(2ka)\right) = \xi^-\left(\left[-\rho_0\omega^2+\frac{(\mathbf{k}\cdot\mathbf{B}_{0l})^2}{\mu_0}\right]\operatorname{csch}(2ka)\right) \quad (5.8)$$

and the equation at $x = -a$ stays the same,

$$\xi^-\left(-gk\rho_0+\frac{(\mathbf{k}\cdot\mathbf{B}_{0v})^2}{\mu_0}+\left[-\rho_0\omega^2+\frac{(\mathbf{k}\cdot\mathbf{B}_{0l})^2}{\mu_0}\right]\coth(2ka)\right) = \xi^+\left(\left[-\rho_0\omega^2+\frac{(\mathbf{k}\cdot\mathbf{B}_{0l})^2}{\mu_0}\right]\operatorname{csch}(2ka)\right) \quad (5.9)$$

Combining these gives

$$\omega^4 + \left(-2\frac{(\mathbf{k}\cdot\mathbf{B}_{0l})^2}{\mu_0\rho_0} - \left[\frac{(\mathbf{k}\cdot\mathbf{B}_{0v})^2}{\mu_0\rho_0} + \frac{(\mathbf{k}\cdot\mathbf{B}_{0t})^2}{\mu_0\rho_0} \right] \coth(2ka) \right) \omega^2 - (gk)^2$$
$$+ gk \left[\frac{(\mathbf{k}\cdot\mathbf{B}_{0v})^2}{\mu_0\rho_0} - \frac{(\mathbf{k}\cdot\mathbf{B}_{0t})^2}{\mu_0\rho_0} \right] + \frac{(\mathbf{k}\cdot\mathbf{B}_{0v})^2}{\mu_0\rho_0} \frac{(\mathbf{k}\cdot\mathbf{B}_{0t})^2}{\mu_0\rho_0}$$
$$+ \left[\frac{(\mathbf{k}\cdot\mathbf{B}_{0v})^2}{\mu_0\rho_0} + \frac{(\mathbf{k}\cdot\mathbf{B}_{0t})^2}{\mu_0\rho_0} \right] \frac{(\mathbf{k}\cdot\mathbf{B}_{0l})^2}{\mu_0\rho_0} \coth(2ka) + \left[\frac{(\mathbf{k}\cdot\mathbf{B}_{0l})^2}{\mu_0\rho_0} \right]^2 = 0 \quad (5.10)$$

which has the solution

$$\omega^2 = \left(\frac{(\mathbf{k}\cdot\mathbf{B}_{0l})^2}{\mu_0\rho_0} + \left[\frac{(\mathbf{k}\cdot\mathbf{B}_{0v})^2}{2\mu_0\rho_0} + \frac{(\mathbf{k}\cdot\mathbf{B}_{0t})^2}{2\mu_0\rho_0} \right] \coth(2ka) \right)$$
$$\pm \left(\left\{ \left[\frac{(\mathbf{k}\cdot\mathbf{B}_{0v})^2}{2\mu_0\rho_0} + \frac{(\mathbf{k}\cdot\mathbf{B}_{0t})^2}{2\mu_0\rho_0} \right] \coth(2ka) \right\}^2 + (gk)^2 \right.$$
$$\left. - \frac{(\mathbf{k}\cdot\mathbf{B}_{0v})^2}{\mu_0\rho_0} \frac{(\mathbf{k}\cdot\mathbf{B}_{0t})^2}{\mu_0\rho_0} + gk \left[\frac{(\mathbf{k}\cdot\mathbf{B}_{0t})^2}{\mu_0\rho_0} - \frac{(\mathbf{k}\cdot\mathbf{B}_{0v})^2}{\mu_0\rho_0} \right] \right)^{1/2} \quad (5.11)$$

Here, four values of axial premagnetization are considered: B_{z0} = 0.1, 0.2, 0.5, and 0.7 T. Fig. 5.5 shows density contours of each configuration, as well as the initial unmagnetized case, when the axially-averaged radius is approximately 1 cm. As before, the red overlays indicate the liner radius as a function of axial location using a cutoff density of 10^{15} cm^{-3}, with the corresponding DFTs shown in Fig. 5.6.

It is clear qualitatively from Fig. 5.5 and quantitatively from Fig. 5.6 that there is a negligible difference in either the dominant MRT wavelength(s) or the amplitude when the liner has a radius of 1 cm. Consider the $B_{z0} = 0.2$ T case, when the radius is $\sim$1 cm at 160 ns. The acceleration at this time (from the polynomial fit) is -9.4$\times 10^{12}$, the liner is approximately $\sim$ 1.5 mm thick, and the average density (noting the liner M/L of 8.4 μg/cm), is 10^{-2} kg/m^3. A significant axial magnetic field gradient is present in the liner region; for the sake of argument,

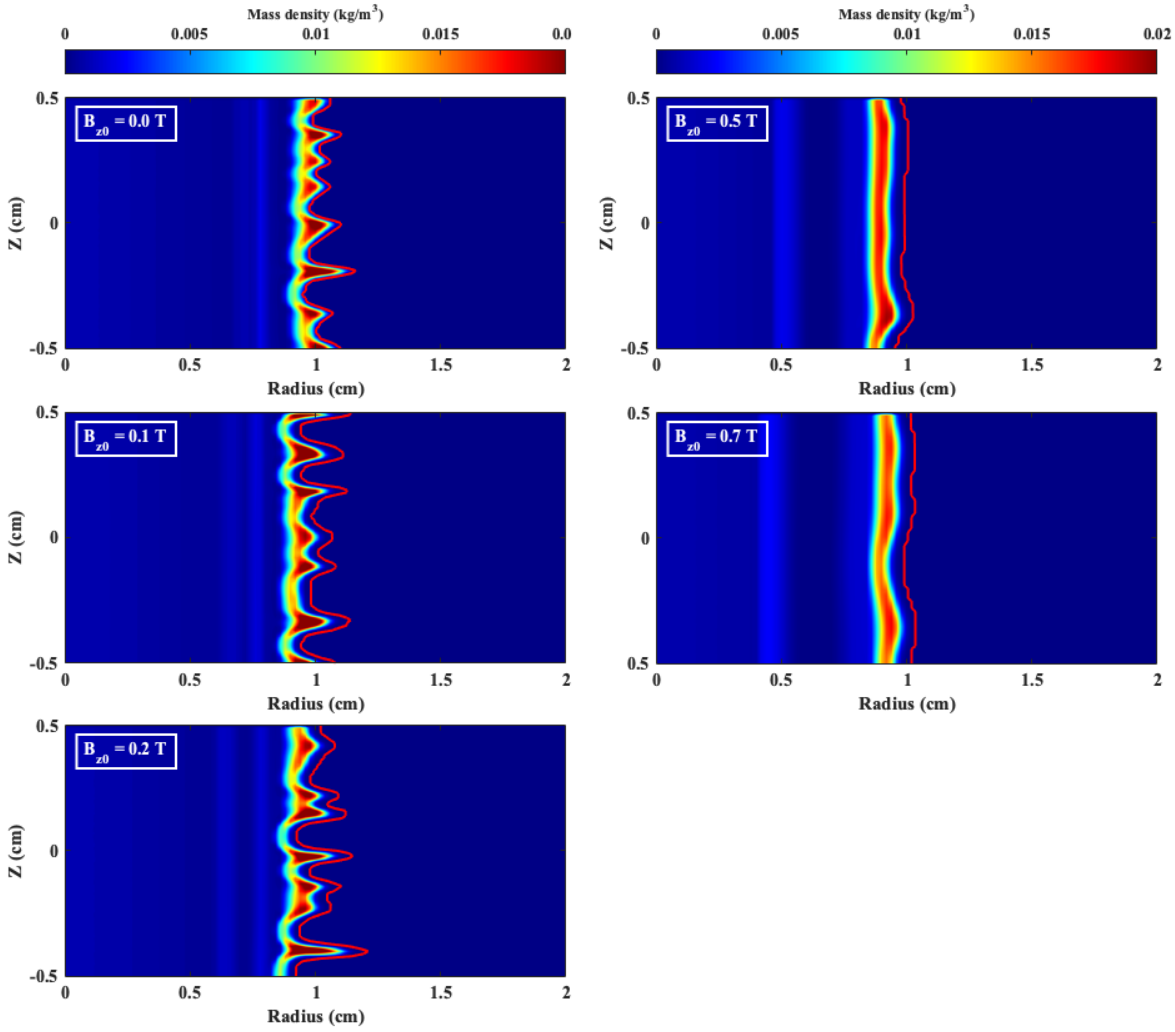

Figure 5.5: Density contours for the Ne/D LTD problem with $B_{z0} = 0$, 0.1, 0.2, 0.5, 0.7 T when the average liner radius is 1 cm. The red overlays indicate the liner radius as determined by a cutoff density of 10^{15} cm^{-3}.

let B_{0l} be defined as the average field in the liner region, 0.63 T, B_{0v} is 0.17 T, and $B_{0t} = 1.88$ T, the average value of B_z at $r = 0.85$ cm. The relevant quantities for estimating the growth rate from Eq. 5.11 are shown in Table 5.1. From these estimates, an instantaneous growth rate of 1.87×10^8/s is predicted, whereas the classical growth rate $\sqrt{gk}$ is 1.88×10^8/s. This indicates that, with a B_{z0}=0.2 T field, there is negligible MRT stabilization by axial magnetic field line tension.

It is interesting to note that, holding other parameters constant, the value of B_{0t} has no impact on this growth rate. This is because the feedthrough factor, $2ka$, is 5.65 - greater than one.

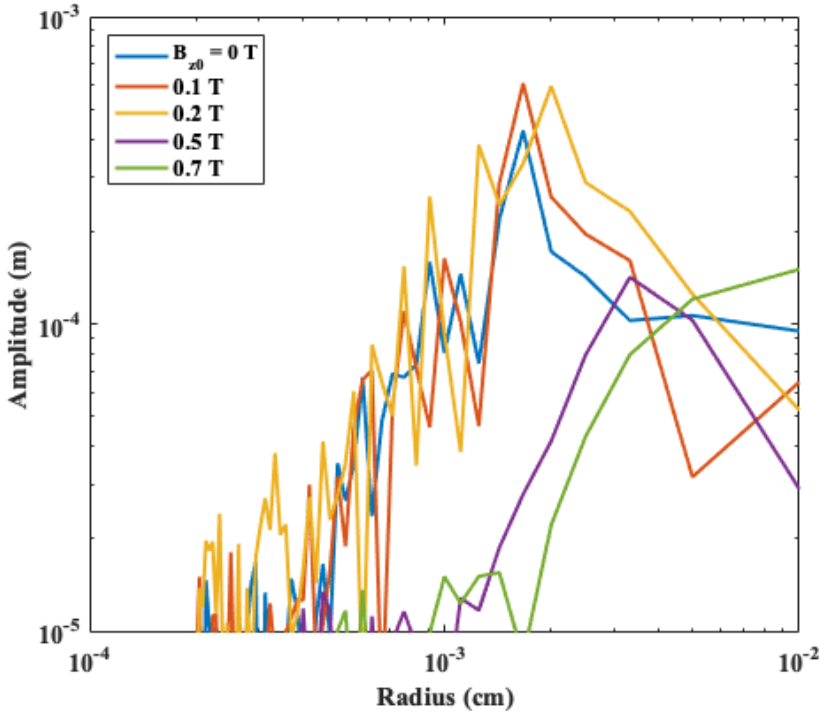

Figure 5.6: DFTs of liner radius for the Ne/D LTD problem for $B_{z0} = 0$, 0.1, 0.2, 0.5, 0.7 T when the average liner radius is 1 cm.

Table 5.1: Relevant quantities in calculating the instantaneous growth rate of the $\lambda = 1.667$ mm mode in the B_{z0} = 0.2 T Ne/D LTD test problem when the average liner radius is 1 cm.

B_{z0} (T)	g (m/s^2)	a (m)	ρ_0 (kg/m^3)	B_{0t} (T)	B_{0l} (T)	B_{0v} (T)
0.2	9.4×10^{12}	7.5×10^{-4}	9.6×10^{-3}	1.88	0.63	0.17
γ [s^{-1}]	-ω^2 [s^{-2}]	gk [s^{-2}]	$\coth(2ka)$	$\frac{(\mathbf{k}\cdot\mathbf{B}_{0t})^2}{\mu_0\rho_0}$ [s^{-2}]	$\frac{(\mathbf{k}\cdot\mathbf{B}_{0l})^2}{\mu_0\rho_0}$ [s^{-2}]	$\frac{(\mathbf{k}\cdot\mathbf{B}_{0v})^2}{\mu_0\rho_0}$ [s^{-2}]
1.87×10^{8}	3.49×10^{16}	3.54×10^{16}	1.00	4.18×10^{15}	4.73×10^{14}	3.41×10^{13}

For these parameters, it is also noted that the lowest possible wavelength (due to axial resolution), 200 μm has only a $\sim 6\%$ reduction from the classical growth.

This is contrasted with the growth estimate in Table 5.2 for the 0.5 B_{z0} T test case. There is a 10-fold increase in the average magnetic field in the liner B_{0l} relative to the 0.2 T case, and the value of B_{0t} is proportionally much lower - i.e. the axial magnetic field is snowplowed with the liner, as opposed to ahead of it. It is also interesting to note that, while total flux in the entire

simulation region is conserved, 83% is between $r = 1$ and the return current radius in the 0.2 T case, whereas this value is only 68% in the 0.5 T case. This is an interesting phenomenon that requires further study. Here we note, as is clear from the values in Table 5.2, that there is no growth of the 1.667-mm mode at 160 ns. Growth over time of the 1.667-mm mode is shown in Fig. 5.7 to be negligible for the 0.5 T and 0.7 T modes, and approximately the same for the 0, 0.1, and 0.2 B_z cases.

Table 5.2: Relevant quantities in calculating the instantaneous growth rate of the $\lambda = 1.667$ mm mode in the B_{z0} = 0.5 T Ne/D LTD test problem when the average liner radius is 1 cm.

B_{z0} (T)	g (m/s^2)	a (m)	ρ_0 (kg/m^3)	B_{0t} (T)	B_{0l} (T)	B_{0v} (T)
0.5	8.5×10^{12}	7.8×10^{-4}	0.008	8.86	6.41	0.35
γ [s^{-1}]	-ω^2 [s^{-2}]	gk [s^{-2}]	$\coth(2ka)$	$\frac{(\mathbf{k}\cdot\mathbf{B}_{0t})^2}{\mu_0\rho_0}$ [s^{-2}]	$\frac{(\mathbf{k}\cdot\mathbf{B}_{0l})^2}{\mu_0\rho_0}$ [s^{-2}]	$\frac{(\mathbf{k}\cdot\mathbf{B}_{0v})^2}{\mu_0\rho_0}$ [s^{-2}]
–	-1.7×10^{16}	3.20×10^{16}	1.00	9.24×10^{16}	4.85×10^{16}	1.44×10^{14}

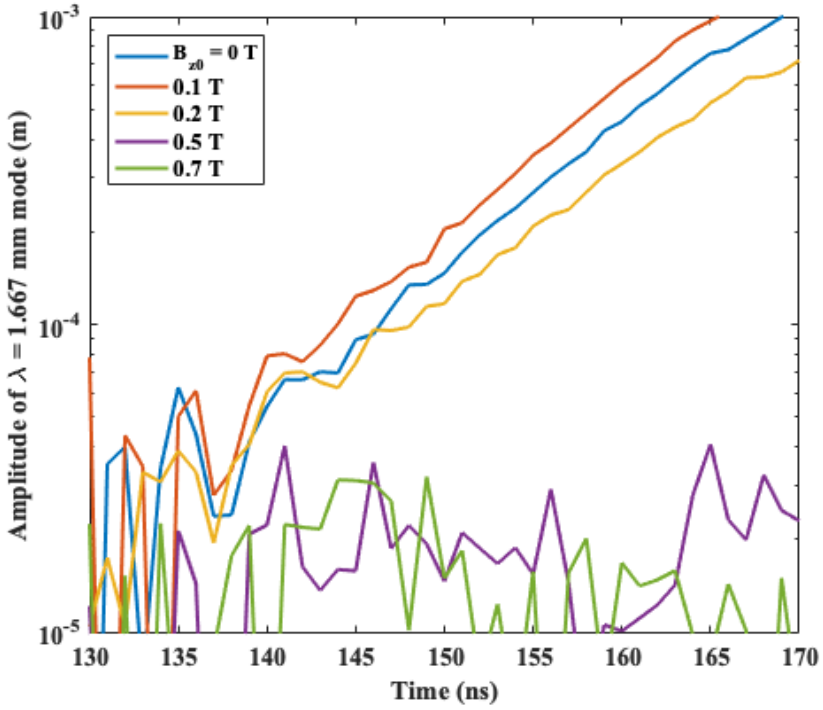

Figure 5.7: Amplitude of the $\lambda = 1.667$ mm MRT mode as a function of time for the Ne/D LTD problem with $B_{z0} = 0$, 0.1, 0.2, 0.5, and 0.7 T.

5.3 MRT mitigation in double-liner implosions

It was shown in the previous section that, due to the large (10^{13}) accelerations and initial radius (2.5 cm) of the Ne/D test problem, a field of 0.5 T was required to stabilize the implosion. As will be discussed in the next section, this method of MRT stabilization reduces the deuterium yield in excess of two orders of magnitude from 1-D, 0-B_z simulations - from $\sim 10^9$ to $\sim 10^7$. It is therefore useful to consider another form of MRT mitigation: density profile tailoring.

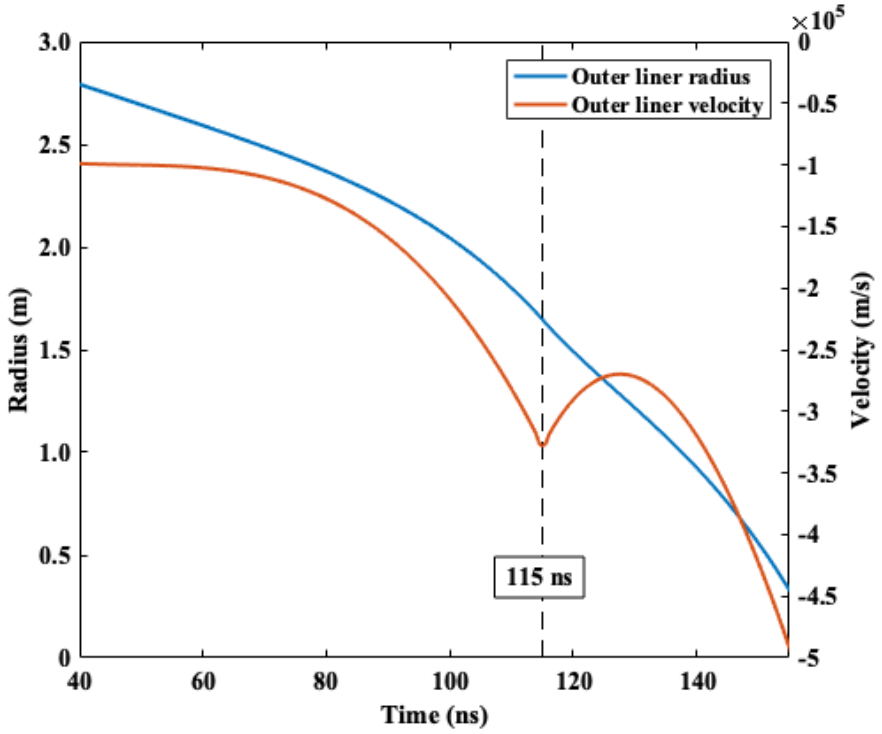

Figure 5.8: Outer liner radius and velocity as a function of time for the Ne/Ne/D LTD problem with $B_{z0} = 0$ T. The outer liner merges with the inner liner at approximately 115 ns.

The concept is simple: the MRT instability is an acceleration-driven - if the liner is imploded at a constant (or decreasing) velocity, then the MRT instability does not develop. An early (theroetical) example of this in a single gas-puff is Ref. [64], in which a density profile that scaled as r^{-3} was shown to stabilize the pinch until the entire load was swept up by the magnetic piston. This requires designing a customized nozzle that can provide the desired profile,

which may not be practically feasible. Another approach is to simply increase the number of liners from one to two. Of course, more liners can be used, but this increases the initial load radius. Sze. et al [65] have demonstrated successful experimental implementation of what the authors call a ”pusher-stabilizer-radiator” gas-puff Z-pinch, in which the pusher and stabilizer are the liners and the radiator is the target, but yield is measured in X-ray energy rather than neutrons. This configuration has been used regularly and recently on the COBRA generator (0.9 MA, 200 ns) [110] but has yet to be implemented on any platform (to our knowledge) in which the radiator is replaced with fusion fuel or with any degree of axial premagnetization - in essence, a double-liner SZP load.

5.3.1 With no axial premagnetization

In the previous section, recall that the single liner has peak density 10^{-3} kg/m^3 centered at 2.5 cm with FWHM 0.5 cm, and the target is centered on axis with FWHM 1 cm. In this section, the liner is divided into two - the inner liner is centered at 1.25 cm and the outer at 2.5 cm, both with FWHM 0.5 cm. To keep the total M/L the same, the inner liner has peak density 10^{-3} kg/m^3 and the outer liner has peak density 5×10^{-4} kg/m^3.

The trajectory of the liner is well-modeled by two 4th-order polynomial fits, with the transition over 114-116 ns - the approximate time the outer liner merges with the inner liner. There is a period of deceleration through 128 ns, after which time the liners have merged into one liner, which converges on axis. The trajectory of liner radius and velocity is summarized in Fig. 5.8, and corresponding density contours of the liner at 105-155 ns in increments of 10 ns is shown in Fig. 5.9.

DFTs of liner radius after the outer liner has merged with the inner liner, shown on the left in Fig. 5.10, indicate that the dominant modes are in the wavelength range 1.667-3.333 mm, with the mode $\lambda = 2.5$ mm having the greatest amplitude. There is clear indication of amplitude non-growth and/or decrease during the period of positive acceleration, as shown on the right side

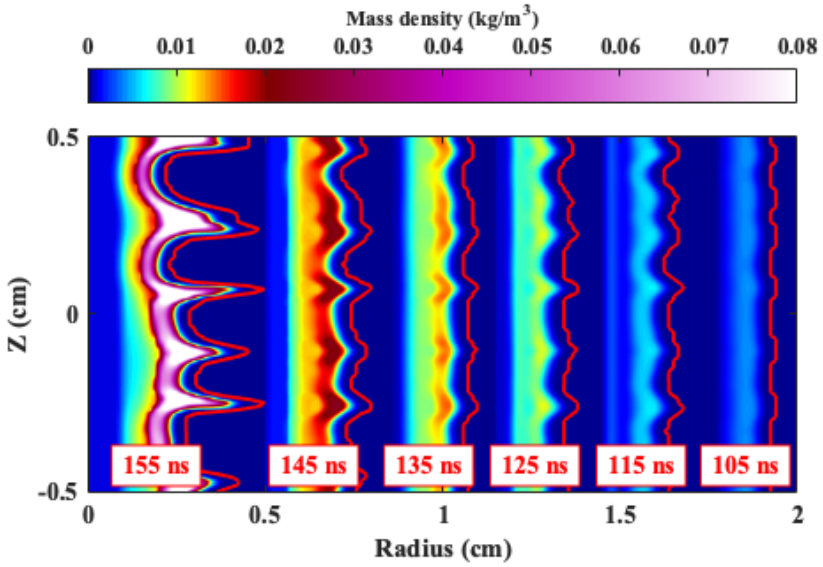

Figure 5.9: 2-D mass density contours for the Ne/Ne/D LTD problem with $B_{z0} = 0$ T from 105-155 ns. The red overlays indicate the liner radius as determined by a cutoff density of 10^{15} cm^{-3}.

of Fig. 5.10, followed by linear growth after 140 ns until saturation and pinch disruption after 155 ns.

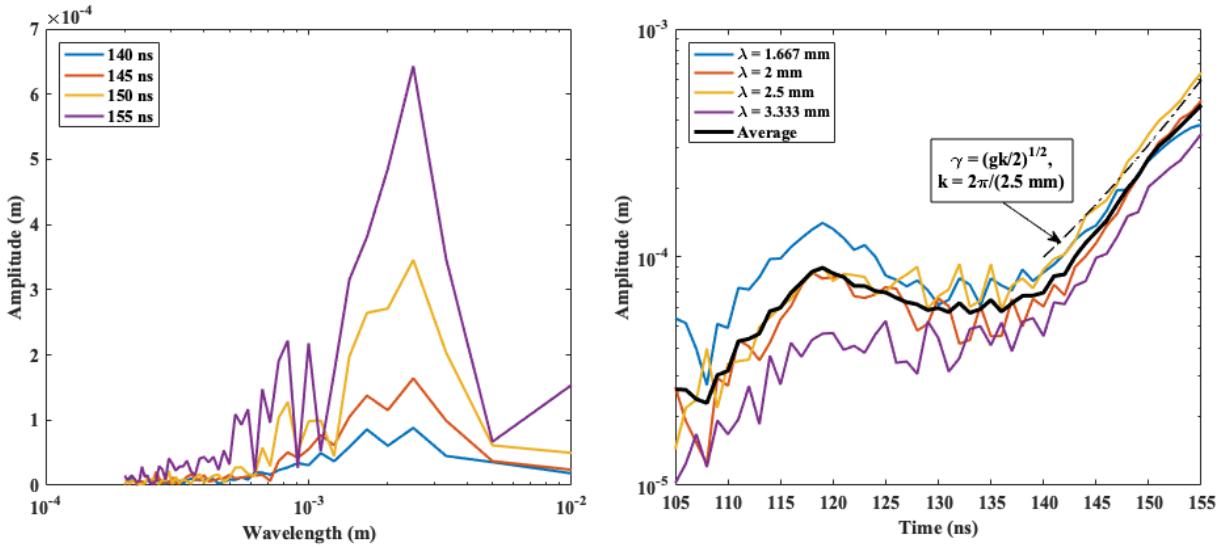

Figure 5.10: (Left) DFTs of outer liner radius at 140, 145, 150, and 155 ns, and (right) amplitude of the $\lambda = 1.667$ - 3.333 mm modes as a function of time for the Ne/Ne/D LTD problem with $B_{z0} = 0$ T. The average amplitude of the four modes is shown in black.

5.3.2 With axial premagnetization

Due to the large acceleration ($> 10^{13}$) m/s^2 near the end of implosion, large growth rates ($\gtrsim 10^8$/s) are expected regardless of the liner geometry. The target in an SZP-like load is typically a small fraction ($\sim 1-10\%$) of the total load mass and can only reduce MRT growth in the few ns prior to peak compression. To stabilize the load therefore requires some degree of axial premagnetization. In this section, the Ne/Ne/D implosion is considered using the same degrees of axial pre-magnetization as in the single-liner case: 0.1, 0.2, 0.5, and 0.7 T.

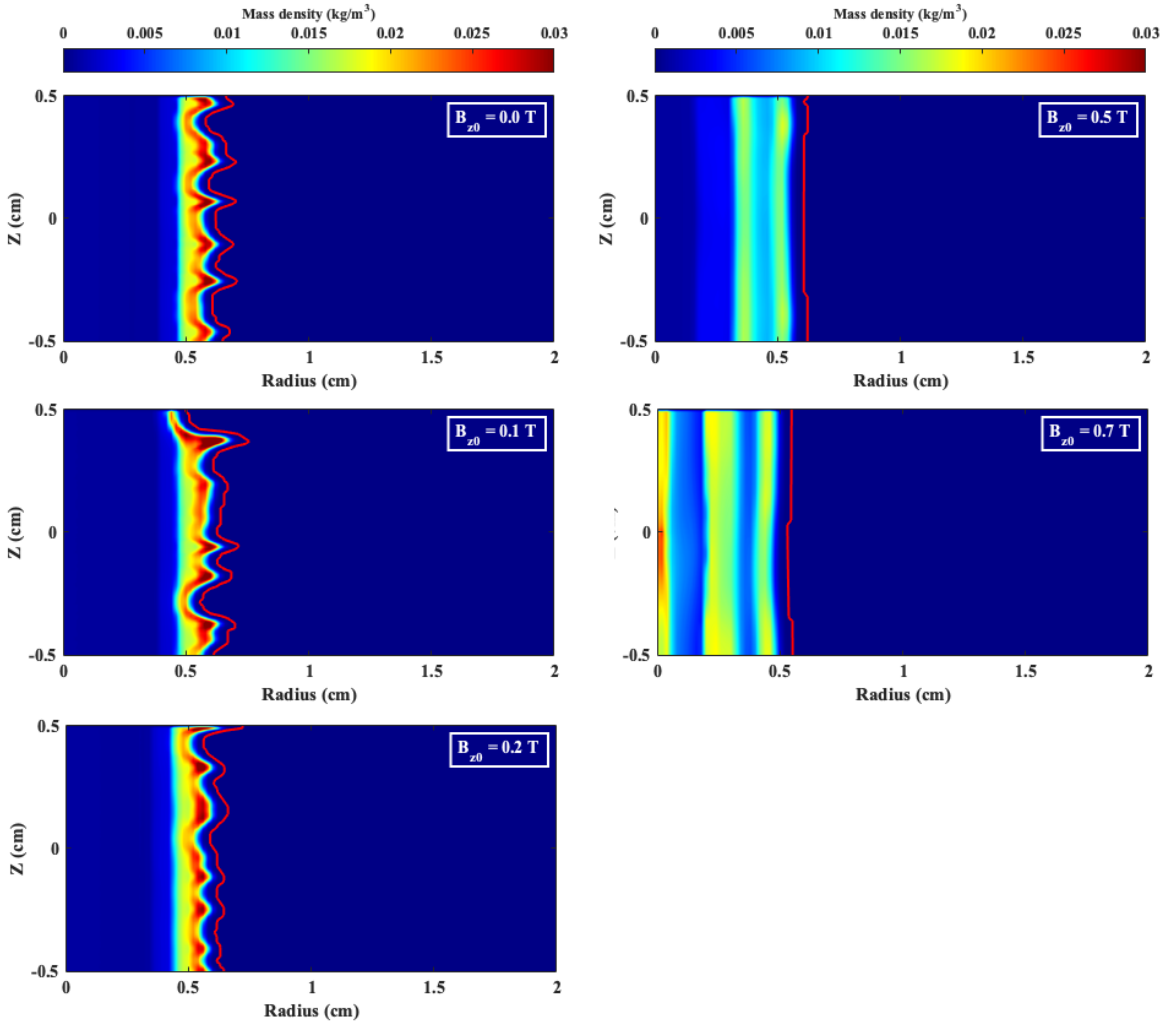

Figure 5.11: Density contours for the Ne/D LTD problem with $B_{z0} = 0$, 0.1, 0.2, 0.5, 0.7 T when the average liner radius is 6 mm. The red overlays indicate the liner radius as determined by a cutoff density of 10^{15} cm^{-3}.

Shown in Fig. 5.11 are density contours after the liners have merged, and the average outer radius is 6 mm. For reference, this is at 148 ns for the 0 T B_{z0} case, approximately halfway between peak compression and the start of linear MRT growth after the liners have merged. As shown by the corresponding DFTs in Fig. 5.12, there is negligible MRT mitigation in the cases of $B_{z0} = 0.1$ T or 0.2 T, when the liner has radius 6 mm. As in the single-liner case, the same dominant wavelengths emerge (1.667-3.333) mm. and there is no significant MRT growth for any

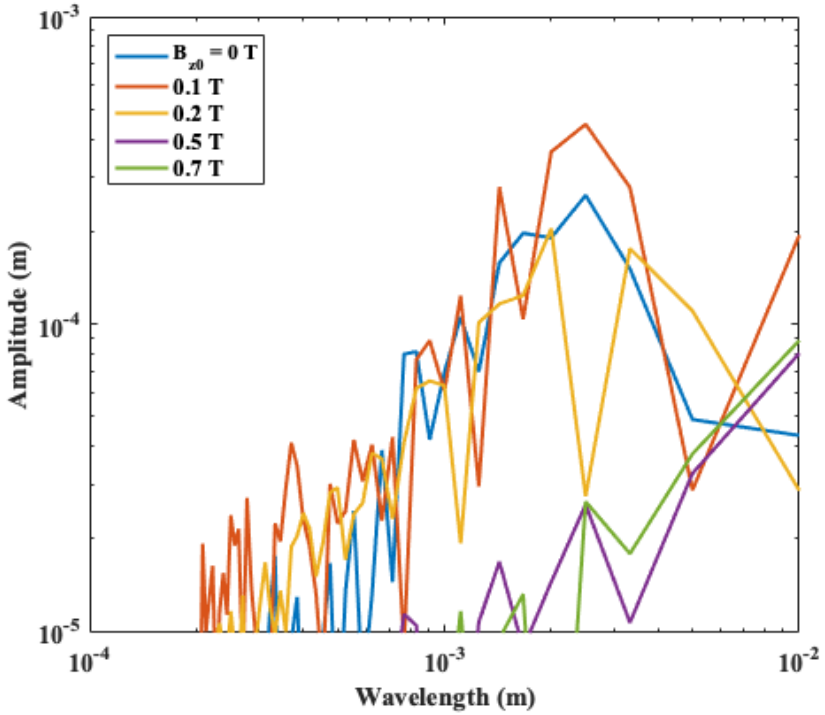

Figure 5.12: DFTs of liner radius for the Ne/Ne/D LTD problem for $B_{z0} = 0$, 0.1, 0.2, 0.5, 0.7 T when the average liner radius is 6 mm.

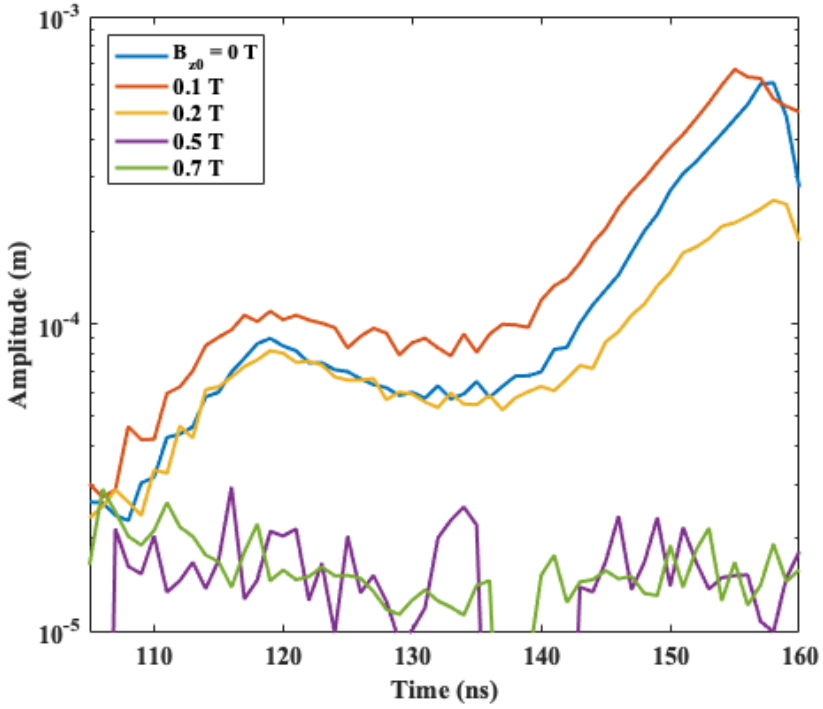

Figure 5.13: Mode-averaged (1.667-3.333 mm) amplitude of MRTI as a function of time for the Ne/Ne/D LTD problem for $B_{z0} = 0$, 0.1, 0.2, 0.5, and 0.7 T cases.

wavelength when $B_{z0} = 0.5$ or 0.7 T. It is interesting to note that, in the 0.5 and 0.7 T B_{z0} cases, the compressed axial magnetic flux is large enough that the liners do not actually merge.

The mode-averaged MRT amplitude as functions of time for the 1.667-3.333 mm modes are shown in Fig. 5.13. There is negligible mode growth in the 0.5 T and 0.7 T for the duration of the implosion, and most notably a significant decrease in average amplitude between the 0/0.1 T cases and the 0.2 T case. The trajectory of liner radii among these three cases between 150 and 160 ns is similar enough that the decrease in growth cannot be attributed to deceleration.

To determine whether this deceleration can be attributed to magnetic field line tension, estimates of the relevant quantities for calculating ω^2 for the most unstable mode for the 2-mm mode using Eq. 5.11. While these estimates, shown in Table 5.3, are approximate averages because B_z and ρ are highly non-uniform, it is clear that the reduction in MRT growth observed in the 0.2 T case after 150 ns can be attributed to tension in the axial magnetic field lines. As

Table 5.3: Relevant quantities in calculating the instantaneous growth rate of the $\lambda = 2$ mm mode in the B_{z0} = 0.2 T Ne/Ne/D LTD test problem when the average liner radius is 3.6 mm.

B_{z0} (T)	g (m/s^2)	a (m)	ρ_0 (kg/m^3)	B_{0t} (T)	B_{0l} (T)	B_{0v} (T)
0.2	1.0×10^{13}	7.5×10^{-4}	0.031	12.4	13.5	0.6
γ [s^{-1}]	-ω^2 [s^{-2}]	gk [s^{-2}]	$\coth(2ka)$	$\frac{(\mathbf{k}\cdot\mathbf{B}_{0t})^2}{\mu_0\rho_0}$ [s^{-2}]	$\frac{(\mathbf{k}\cdot\mathbf{B}_{0l})^2}{\mu_0\rho_0}$ [s^{-2}]	$\frac{(\mathbf{k}\cdot\mathbf{B}_{0v})^2}{\mu_0\rho_0}$ [s^{-2}]
–	-1.5×10^{16}	3.14×10^{16}	1.00	3.9×10^{16}	4.62×10^{16}	9.1×10^{13}

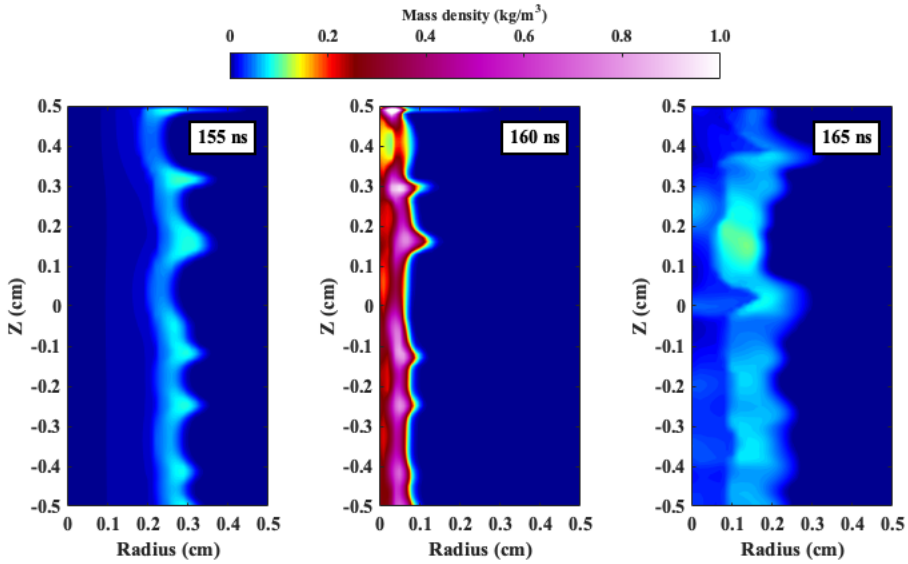

Figure 5.14: Density contours for the Ne/Ne/D LTD problem with $B_{z0} = 0.2$ T at 155, 160, and 165 ns. Peak compression occurs at 160-161 ns, but the pinch remains intact due to stabilization by B_z.

a consequence of the reduced growth, the pinch remains intact through peak compression (at 160-161 ns), as shown in Fig. 5.14.

Reducing the required axial magnetic field to MRT-stabilize an SZP-like load has significant implications for performance, because it allows the target to stably reach higher convergences, and therefore produce higher temperatures, densities, and greater yield.

5.4 Comparison of dynamics between single and double-liner implosions

It has been demonstrated throughout this work that the majority of target heating and compression in a gas-puff SZP is done by the inertia of the liner, i.e. the liner mass distribution ultimately controls the dynamics of the implosion. It is therefore useful to consider whether target heating is affected by partitioning the single-liner mass into two.

As the single liner is more massive, it is slower to initially accelerate than the outer liner in the Ne/Ne/D configuration. Though the outer liner decelerates as it merges with the inner liner, the net result is that the double liner configuration implodes approximately 20 ns earlier than the single liner. With B_{z0} = 0 T, in 1-D the implosion times are $\sim$ 160 ns and $\sim$ 180 ns for the double and single liner configurations, respectively. However, the terminal liner velocities are comparable: $\sim$ 560 km/s when the liner radius is $\sim$ 1 mm.

Any disparity in target heating between the single and double liner configurations would be apparent in a plot of target ion temperature as a function of target convergence ratio (CR), shown in Fig. 5.15. Recall that in a purely adiabatic implosion, temperature will increase proportionally to $CR^{4/3}$, and shock heating and ohmic heating can result in super-adiabatic heating, whereas thermal conduction and radiation losses can result in sub-adiabatic heating. Also recall that it was shown in the preceding chapter that the predominant heating mechanism (excluding PdV heating) is shock heating, and that Ohmic heating of the target is negligible. There is greater shock heating of the target when a double liner is used, though the additional heating is offset by greater losses. The net result is that, for the unmagnetized, 1-D cases, there is negligible difference in final target conditions - a maximum CR of $\sim$ 50 and a peak temperature of 3.6 keV and 4.0 keV for the single and double configurations, respectively. This suggests that the 1-D target dynamics are unaffected when a single liner is replaced with the double liner, provided the overall mass of the load is held constant.

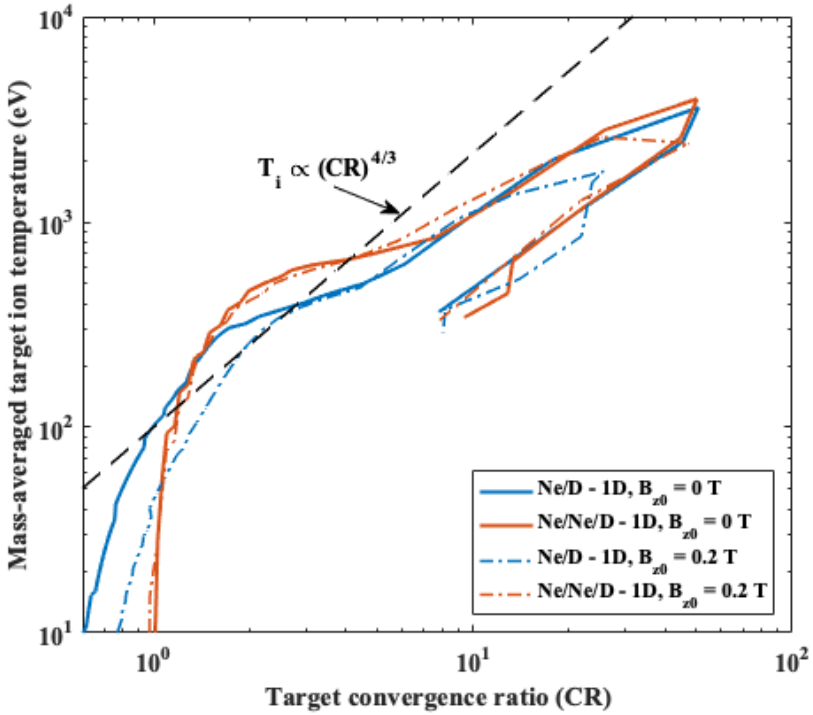

Figure 5.15: Mass-averaged target ion temperature as a function of target convergence ratio for the 1-D Ne/D and Ne/Ne/D, $B_{z0} = 0$ and 0.2 T LTD problems. In a purely adiabatic compression in cylindrical geometry, temperature increases as $\mathrm{CR}^{4/3}$, shown for reference as the dashed line.

Also shown in Fig. 5.15 are the same simulations conducted with $B_{z0} = 0.2$ T. There is a negligible change in dynamics due to the additional axial magnetic flux in the target with regard to shock heating. However, the maximum target convergence ratio achieved does decrease, particularly for the single liner case. There is a corresponding decrease in DD neutron yield by an order of magnitude in the single liner case from 0 to 0.2 T B_{z0}, whereas the reduction in yield is only a factor of two in the case of the double-liner implosion. The reduction in peak temperature/yield is due to axial flux compression - both plasma pressure and magnetic pressure are of order 10^{10} Pa, or 0.1 Mbar. For reference, a 160 T has pressure of ~ 0.1 Mbar. Recalling that $B_z = B_{z0}(\mathrm{CR})^2$, a 160 T field is achieved at CR of 28, which is below the target CR observed in Fig. 5.15. The maximum axial magnetic fields are ~ 320 T and ~ 250 T for the single and double-liner configurations, respectively, which is consistent with the lower maximum target CR

seen in the single liner relative to the double liner.

The results of this study are summarized in Tables 5.4-5.6, which show the DD neutron yield, peak average target ion temperature, and minimum average liner and target radius for the Ne/D and Ne/Ne/D configurations in 1-D and 2-D, and for B_{z0} values of 0, 0.1, 0.2, 0.5, and 0.7 T. Conventionally, neutron yield is expected to decrease when the dimensionality of the problem is increased. This is because instabilities that develop in higher dimensions and disrupt the implosion cannot develop in lower dimensions. The most relevant to our discussion is the $m = 0$ MRT instability, which will appear in 2-D but not 1-D.

A significant increase in the average minimum liner radius is indicative of a highly-MRT unstable implosion due to the large radii of the spikes in the spike-bubble structure of the liner. This is mostly clearly seen in the single-liner cases for $B_{z0} \leq 0.2$ T, where the average minimum liner radius increases by a factor of three in 2-D simulations relative to 1-D. This is also observed in the double liner cases for $B_{z0} = 0$ T and 0.1 T, but a significant increase is notably absent for $B_{z0} = 0.2$ T.

There is a marked increase in liner and target compression for the $B_{z0} = 0.5$ T and $B_{z0} = 0.7$ T cases from 1-D to 2-D. The implosion times are significantly earlier, and there is a substantial increase in yield - particularly for B_{z0}=0.7 T. Though the yields are far too low to be of any practical use, this is an interesting phenomenon that we have not observed in previous work. A qualitative comparison of the azimuthal current density, J_θ, and B_z within the load suggests that, during the implosion of "over-magnetized" loads, the $\mathbf{J}_\theta \times \mathbf{B}_z$ force is comparable to the $\mathbf{J}_z \times \mathbf{B}_\theta$ force at the interface between the liner and target. In 2-D simulations, this force is 2-4 times larger, which would contribute to target acceleration and result in an earlier implosion.

For the cases studied here, neutron yield and peak average target temperature are generally higher in 2-D than in 1-D. The higher temperatures and yields for the $B_{z0} = 0.5$ and 0.7 T cases can be explained by greater target compression, but this is not the case in the 2-D simulations for $B_{z0} \leq 0.2$. In these cases, the higher average temperatures can be attributed to instability-driven,

Table 5.4: Deuterium-deuterium neutron yield for the 1-D and 2-D Ne/D and Ne/Ne/D problems with $B_{z0} = 0$, 0.1, 0.2, 0.5, and 0.7 T.

	Ne/D		Ne/Ne/D	
B_{z0} (T)	1-D	2-D	1-D	2-D
0	1.4×10^{9}	2.8×10^{8}	1.9×10^{9}	1.6×10^{9}
0.1	3.1×10^{8}	6.7×10^{8}	4.9×10^{8}	1.0×10^{9}
0.2	4.0×10^{7}	1.6×10^{8}	2.2×10^{8}	8.3×10^{8}
0.5	7.5×10^{4}	8.9×10^{6}	2.4×10^{7}	8.9×10^{7}
0.7	2.8×10^{3}	4.4×10^{5}	4.6×10^{6}	3.6×10^{7}

Table 5.5: Peak average target ion temperature (keV) for the 1-D and 2-D Ne/D and Ne/Ne/D problems with $B_{z0} = 0$, 0.1, 0.2, 0.5, and 0.7 T.

	Ne/D		Ne/Ne/D	
B_{z0} (T)	1-D	2-D	1-D	2-D
0	3.6	3.3	4.0	4.4
0.1	2.5	4.0	3.0	4.4
0.2	1.8	2.8	2.6	3.8
0.5	0.7	1.5	2.0	2.7
0.7	0.4	1.0	1.4	2.2

Table 5.6: Minimum average liner and target radius (mm) for the 1-D and 2-D Ne/D and Ne/Ne/D problems with $B_{z0} = 0$, 0.1, 0.2, 0.5, and 0.7 T..

	Ne/D				Ne/Ne/D			
	1-D		2-D		1-D		2-D	
B_{z0} (T)	Liner	Target	Liner	Target	Liner	Target	Liner	Target
0	0.95	0.16	3.24	0.79	0.96	0.16	1.69	0.28
0.1	1.04	0.16	3.21	0.73	0.96	0.16	2.08	0.41
0.2	1.18	0.31	3.35	0.95	1.18	0.17	1.40	0.29
0.5	3.52	1.45	2.43	0.96	2.54	0.64	2.40	0.64
0.7	4.08	1.91	3.03	1.27	3.70	0.94	3.09	0.86

localized hot regions that develop in the target that then heat the remaining portion by thermal conduction. The higher yields observed in 2-D are not only due to the higher temperatures. Because the pinches are highly unstable, the effective dwell time can be significantly larger. For example, in the Ne/D $B_{z0} = 0.2$ T case, the yield rose from 5% to 95% of the overall yield in 1.9 ns in 1-D, whereas in 2-D the middle-90% of yield was produced over 6.7 ns. It would be unlikely

to demonstrably observe this effect in experiment, as it would be expected that a highly-unstable implosion would either disrupt, undergo significant mixing, or produce significant yield due to beam-target effects. None of these physics are properly treated in MHD, so future work must be conducted with kinetic codes.

5.5 Conclusion

In this chapter, two methods of MRT instability mitigation were implemented in a Ne/D test problem: axial premagnetization and density profile tailoring. These two approaches have been tested successfully in Z-pinch experiments, but not studied in combination or in detail in SZP-type loads, where the target is fusion fuel. To simulate these problems, it was necessary to use the MHD code HYDRA rather than the MHD code MACH2, because the latter does not explicitly enforce the divergence-free magnetic field constraint and introduces a correction term that violates flux conservation.

It was shown that, for the selected initial geometry - a gas-puff liner centered at $r = 2.5$ cm of length 1 cm driven by a circuit that delivers ~ 850 kA in ~ 160 ns to a short circuit, that the dominant MRT wavelengths are of order 1 mm. A fourth-order polynomial fit to liner radius as a function of time provided acceleration and an estimate of classical RT growth, $\sqrt{gk}$. This method was shown to overestimate γ^2 by a factor of 2-6 for the dominant wavelengths, suggesting that non-ideal effects, e.g. resistivity, provide some degree of MRT mitigation, but not enough to stabilize the pinch.

The first mitigation mechanism considered is axial premagnetization. Simulations of the original problem were altered to consider B_{z0} of 0.1, 0.2, 0.5, and 0.7 T. From density contours and DFTs of liner radius when the average was ~ 1 cm, it was concluded that the same dominant wavelengths for the unmagnetized case were also present when $B_{z0} = 0.1$ and 0.2 T, and grew at the same rate. The solution in Chapter 2 which assumed the axial magnetic field in the target

was zero was extended to allow it to be nonzero. A growth rate estimate for the $B_{z0} = 0.2$ T with liner radius 1 cm for the $\lambda = 1.667$ mm mode predicted virtually no mitigation, consistent with observations. A similar estimate for the $B_{z0} = 0.5$ T case predicted growth of the same mode is suppressed, again consistent with what was observed in simulations.

In addition to axial premagnetization, MRT instability growth is reduced by dividing the single liner into two less massive liners. Since the outer liner is less massive, greater acceleration in the liner is observed. However, the instability amplitude is not large enough to feed through the outer liner by the time it collides with the inner liner, during which time the liner undergoes positive acceleration and the average amplitude of the dominant modes decreases. In the final ~ 20 ns of the implosion, liner acceleration was in excess of 10^{13} m/s^2 and the pinch ultimately disrupted as it converged on axis. However, a similar sub-classical growth rate was observed.

It was found that a 0.2 T B_{z0} led to marginal liner stability for the double-liner implosion, whereas a larger 0.5 T field was found to be required to adequately stabilize a single-liner implosion. Here marginal stability means that, while a bubble-spike structure was evident on the liner surface, growth was mitigated such that the liner remained intact though peak compression and expansion. This is particularly relevant for a SZP implosion because it increases the likelihood that neutrons produced are of thermonuclear origin, and not instability-driven, i.e. beam target.

Finally, the effect of axial premagnetization on target heating, compression, and yield was found to be negligible in the cases of 0.1 and 0.2 T B_{z0}, except at peak compression when the magnetic pressure inside the load is comparable to or larger than the plasma pressure. In 1-D simulations, a decrease in yield corresponded to lower target compression and peak temperatures. The expected neutron yield decrease from 1-D to 2-D simulations was observed only in the 0 B_{z0} T case for both configurations - the 2-D yield was higher for all other test cases.

For the 0.1-0.2 T cases, this can be attributed to higher overall target temperatures. This occurs due to the presence of localized hot regions that form due to liner instability, which then thermally conduct throughout the target and raise the average temperature. In addition, the

effective dwell time for unstable implosions is significantly longer. For the 0.5-0.7 T cases, both the liner and target are compressed more in 2-D than in 1-D. This appears to be caused by a significant $\mathbf{J}_\theta \times \mathbf{B}_z$ force that is stronger in 2-D than in 1-D.

In this chapter it was demonstrated that a Ne/D liner-on-target gas puff implosion can be stabilized by a sufficiently large axial magnetic field (0.5 T), but at a cost of significantly reduced yield. Addition of a second liner significantly mitigated MRT growth during the implosion, but due to the large acceleration ($> 10^{13}$ m/s^2) prior to peak compression after the liners merge, cannot prevent pinch disruption alone. A 0.2 T field was required to stabilize the implosion, with an observed neutron yield reduction of only 2.5x from the unmagnetized, 1-D simulation - 2.0×10^9 vs. 8.3×10^8. This is a significant improvement over the yield reduction of ~ 150 for the single liner - 1.4×10^9 for $B_{z0} = 0$ T, 1-D vs. 8.9×10^6 for $B_{z0} = 0.5$ T, 2-D.

Chapter 6

Conclusions and Future Work

6.1 Conclusions

In this thesis, the dynamics and stability of liner-on-target, gas-puff Z-pinches were considered in the context of magneto-inertial fusion. Particular emphasis was placed on shock heating and growth of the magneto-Rayleigh-Taylor instability, topics that have received some, but insufficient attention in the Staged Z-pinch literature. Conventional Z-pinch, shock and stability theory assuming ideal MHD were reviewed and developed in Chapters 1 and 2. The snowplow and slug models gave approximate dynamics of single- and double-liner-on-target implosions, and from the planar Rankine-Hugoniot relations for ideal MHD it was shown that the shock jump conditions with B_z were similar to purely hydrodynamic shocks. Linear MHD stability analysis in planar geometry showed that tension in axial magnetic field lines within the liner could provide mitigation against MRT instability growth. Mitigation from non-ideal effects was briefly discussed, particularly resistivity. Finally, a planar Korteweg-de Vries-Burgers equation was obtained for a magnetosonic wave to describe how a perturbation could evolve into a shock. In Chapter 3 the importance of accurate liner resistivity in modeling shock formation in the target was demonstrated, and it was shown that MRT growth can be mitigated by increasing

the atomic number of the liner. Though the timing of shock formation was affected by liner material, a significant difference in final target adiabat was not observed by changing the liner material. In Chapter 4, a semi-analytic model for liner-on-target, gas-puff magneto-inertial fusion is developed. A significant portion of the model is based on a similar one developed for MagLIF, but additional physics are included that are necessary for a SZP implosion. Test problems are considered and compared with other, well-established codes, and a simple two-part design study is conducted that considered optimization and scaling of a SZP load to high current. Finally, the work in Chapter 5 expands on the work in Chapter 3 by investigating how target dynamics and MRT stability are affected by axial premagnetization, density profile tailoring (by introducing a second liner), and both mechanisms simultaneously.

6.1.1 Unmagnetized single liner-on-target implosions

When the width of a gas-puff liner is comparable to the skin depth, the strength of the diffused $\mathbf{J} \times \mathbf{B}$ force can initiate target compression rather than the liner inertia. Under identical conditions for an Ar/D implosion on Zebra (1 MA, 100 ns) using the MHD code MACH2, the onset of target compression varied by 10s of ns by simply varying the resistivity table used from SESAME 25171 to SESAME 25174. Both tables are poorly resolved at low temperatures and densities, thus motivating the production of a new table. The new table was found, for the parameter regime of interest, to agree with the conventional Spitzer resistivity times a multiplicative factor of 0.5-0.7 - between SESAME 25171 and 25174. The onset of target compression was in between these two cases, lending credence to the observation that target compression for this test problem is initiated by a magnetically diffused $\mathbf{J} \times \mathbf{B}$ force rather than liner inertia.

However, it was found by multiple metrics - the ratio of the magnetic and inertial forces at the interface between the liner and target, and the mass-averaged target ion temperature, that the final conditions of the target are controlled primarily by liner inertia. While shock compression of

the target is initiated by magnetic forces, the driving force of target compression transitions from magnetic to inertial prior to the target convergence ratio reaching a value significantly greater than one. As the problems are identically massed, the target is heated to similar adiabat independent of the timing of shock launch.

A similar set of simulations was conducted using identical initial conditions, in which the only variable is liner material - Ne, Ar, Kr, or Xe. Resistivity generally increases with atomic number, though the difference is less significant than between the SESAME 25171 and 25174 tables. Consequently, the observed onset of shock compression in the target is present, but to a lesser extent than observed in the first problem. It was shown again, that (a) though the target was initially compressed by magnetic forces, inertial forces became dominant, and (b) comparable target adiabats are reached among the four liner materials.

There was clearly greater azimuthal magnetic flux within the liner in higher-Z materials, warranting a consideration of whether the azimuthal magnetic field strength at the interface between the liner and target could be large enough to inhibit thermal conduction. It was shown that, despite this larger flux, the electron Hall parameter, $\omega_{ce}\tau_{ei}$, was at most of order 10 during the run-in, and of order unity at peak compression - when thermal conduction losses are the largest. It was thus concluded that - for this particular configuration - thermal conduction losses are not reduced simply by azimuthal flux diffusion.

Finally, a preliminary study of magneto-Rayleigh-Taylor instability growth by introducing the discrete Fourier transform and performing it on two sets of density contours at 10 and 20 ns prior to peak compression. Sub-mm wavelengths observed on Ne and Ar liner surfaces were not present or much lower amplitude in the more-resistive Kr and Xe surfaces in the earlier images, whereas the $\sim$ 1 mm mode was present in all cases at similar amplitude. This supports the hypothesis, e.g. in [4], that using a higher-Z liner may provide an inherent degree of MRT mitigation due to higher resistivity.

6.1.2 A semi-analytic model for single liner-on-target gas-puff magneto-inertial fusion

Existing analytic and semi-analytic models do not capture all the relevant physics to a SZP-like gas-puff implosion, motivating the development of the presented model. The semi-analytic model for MagLIF (SAMM, [77]) formed the backbone of this model, but physics relevant to MagLIF - e.g. laser preheating - were removed and physics relevant to SZP were added. These include solving for magnetic field diffusion, separate ion and electron temperatures and heat transport, a simplified 1-D radiation transport model that allows for a transition from optically thin to optically thick, and a target shock heating model that solves the Rankine-Hugoniot relations for MHD for a shock propagating perpendicularly to **B** presented in Chapter 2.

Following a presentation of the model, three test problems are presented and discussed. In the first test problem, an Ar/D SZP implosion on the Zebra driver with initial conditions comparable to those used in experiments is presented. The results are compared with a 1-D HYDRA simulation of the same problem. The trajectory of the liner, target and shock front agree well between the two codes, but the peak temperatures between the codes varied significantly, particularly for ions. The difference (4 keV in HYDRA vs. 6.7 keV in the model) could not be attributed to additional compression in the HYDRA simulation. It was seen that in HYDRA, the artificial viscosity model led to significant overheating in low-density liner regions. Limiting the ratio of artificial viscous pressure to plasma pressure, q/p to 0.1 mitigated some of this overheating but not all of it. It was shown that this overheating has some material dependence - peak temperatures were in much better agreement when the liner was hydrogen. A more detailed investigated is challenging due to the "black-box" nature of HYDRA simulations. It was shown that shock heating provided 40 J of heating, equivalent to a preheat of 270 eV, followed by ~ 1 kJ of PdV heating. The predominant heating losses were from electron thermal conduction, followed by ion thermal conduction and then radiation losses, consistent with conventional knowledge that

thermal conduction losses dominate radiation losses at lower densities.

The second test problem considered the original MagLIF point design, which required re-introducing some simple models to account for the solid-density liner, Z circuit, laser preheating, and end losses. The goal was to produce general agreement with the SAMM results illustrating that the results of the original model could be adequately recovered. Comparable yields were obtained with the SAMM results and the original MagLIF point design simulations ([15]), with a fusion yield of 1.2 MJ as opposed to 1.0 MJ in SAMM and 0.5 MJ in Slutz et al. Though α-particle deposition was found to be the dominant heating mechanism when included, end losses were also higher to a simulation without α-particle heating, so the net difference in yield was not large. This was also somewhat seen in [77] for the point design.

The greatest practical use for a semi-analytic model is in performing parameter scan and scaling studies, because they can give ballpark estimates of performance for many configurations without consuming significant computational resources or time. Here, a two-part design study is conducted in which a Kr/D SZP is imploded on the 850-kA, 160 ns LTD recently constructed at UCSD. First, a parameter scan of liner and target densities was performed, holding the load geometry and initial axial magnetic field constant. Neutron yield was maximized while satisfying the constraints of maximum allowable target CR of 30, and limiting the instantaneous growth rate of the $\lambda = 1$ mm, m = 0 MRT mode to $(10\text{ ns})^{-1}$. A point design of 15.5 μg/cm liner mass and 2.1 μg/cm target mass was selected, predicting $Y_{DD} \sim 5 \times 10^9$.

In the second part of the design study, the driver was scaled to a peak current of ~ 20 MA. There were two objectives of the scaling study. First, the radiation model adequately captured the transition of the liner from optically thin to optically thick at two times during the implosion: shock arrival on axis, and at peak compression. In the original "point desigh", the fraction of reabsorbed radiation by the liner at these two times is 1% and $\sim 70\%$, respectively, and increases to $\gtrsim 60\%$ and 90%, respectively, for peak currents higher than a few MA. This is due to scaling the initial density as I^2 to maintain the same implosion time, and optical depth scales approximately

as ρ^{-1}.

HYDRA simulations are conducted at peak currents of 1, 2, 5, 7, and 10 MA and compared with the model predictions. Yield agreement within a factor of 2 is observed between the HYDRA simulation and model predictions for I>2 MA, but is an order of magnitude higher in the model prediction than in the HYDRA simulation for the 1 MA case. This is qualitatively consistent with the higher temperatures observed in the target in the Zebra problem in the model relative to the HYDRA simulation.

6.1.3 Magnetized and double-liner on target implosions

Mitigation of the MRT instability is critical for reproducible, thermonuclear neutron production in a liner-on-target magneto-inertial Z-pinch like the SZP. Both axial premagnetization and density profile tailoring have been implemented successfully in the literature, and are implemented independently here on a Ne/D test problem on the 850-kA, 160 ns LTD at UCSD. The HYDRA code was implemented because the MACH2 code is known to violate axial magnetic flux conservation, which could overpredict stabilization by field line tension in the load. In the unmagnetized Ne/D test problem, the $\lambda = 1.667$ mm mode was dominant and grew linearly during run-in before saturating. However, the growth rate of this mode was shown to be a factor of $\sqrt{3}$ smaller than predicted by the conventional growth rate $\sqrt{gk}$. Similar reductions in growth of the other modes were also observed.

Axial premagnetization was shown to stabilize the pinch for values $B_{z0} \gtrsim 0.5$ T. Estimates of instantaneous growth rate for the $\lambda = 1.667$ mm mode when liner radius is 1 cm for the $B_{z0} = 0.2$ and 0.5 T cases showed that there was virtually no mitigation and zero growth of the mode, respectively. Density profile tailoring by adding a second liner was shown to delay significant MRT growth by introducing a period of positive radial acceleration during the run-in. However, this approach alone was not sufficient to prevent disruption of the pinch due to rapid MRT growth near peak compression. It was found that the field-line tension when $B_{z0} = 0.2$ T

sufficiently mitigated MRT growth and preserved liner integrity through peak compression.

In both single- and double-liner test problems, a B_{z0} of 0.1 or 0.2 T had negligible impact on target heating, compression, and yield except at peak compression when the magnetic pressure in the load is comparable to or larger than the plasma pressure. In 1-D, neutron yield decreased for both configurations as axial magnetic field increased, due to lower target compression and peak temperatures. Neutron yield decreased from 1-D to 2-D only in the $B_{z0} = 0$ T case, and increased for the other configurations. For 0.1 T and 0.2 T cases, this can be attributed to instabilities - though the unstable target has larger radius and lower density, the average temperature is higher and the effective dwell time is longer, resulting in greater peak temperatures and yields. For 0.5 and 0.7 T cases, the load is compressed more in 2-D than in 1-D, which correlates with a larger $\mathbf{J}_\theta \times \mathbf{B}_z$ force. The reason for the greater magnitude of this force in 2-D is unclear and further investigation is warranted, though likely not in the context of magneto-inertial fusion.

The yield reduction from 1-D, $B_{z0} = 0$ T to stabilized 2-D is $>$ 100x for the single liner, because a large B_{z0} field is required - 1.4×10^9 for $B_{z0} = 0$ T, 1-D vs. 8.9×10^6 for $B_{z0} = 0.5$ T, 2-D. The same yield reduction for the double liner is only 2.5x - 2×10^9 for $B_{z0} = 0$ T, 1-D vs. 8.3×10^8 for $B_{z0} = 0.2$ T, 2-D. This is a significant improvement, providing strong motivation for future SZP experiments using double liners.

6.2 Future Work

The results and conclusions of the problems considered in this thesis have provided insight into some of the unanswered questions regarding gas-puff, liner-on-target Z-pinches, however there are several paths forward for future work. The common thread among these categories is the need to evaluate the presented hypotheses in experiments and in simulations that accurately reflect those experiments, i.e. validation. For example, it is well-known that in SZP and other gas-puff experiments, that it is challenging to produce a liner that has an axially uniform mass

distribution. This can result in zippering, in which the low-mass region implodes ahead of the high-mass region. The initial axial magnetic field required to stabilize MRT could be substantially different in the different regions.

While extremely computationally expensive, it would be invaluable to conduct 3-D HYDRA simulations of SZP-like implosions on UCSD's LTD. The growth of $m > 0$ modes are not significantly affected by B_{z0} and their influence on the dynamics remains relatively unknown. Presently, evaluations of liner stability are limited to side-on XUV images. Images taken at recent experiments on the Zebra driver suggest that an initial axial magnetic field of ~ 0.15 T can provide significant MRT mitigation. However, simple estimates of expected growth like those presented in Chapter 5 suggest this should not occur - recall that $B_{z0} = 0.2$ T provided essentially no mitigation for the single liner case, and the dynamics for that test problem are comparable to those on Zebra. It would be useful to extend the analyses here into cylindrical geometry, and to conduct an experiment similar to that posed in Chapter 5 on LTD and directly compare the required B_{z0} for stabilization in experiment with the value predicted by simulations. This would necessarily require generation of synthetic diagnostics that could be used for comparison with experimental data.

Finally, the use of triple-shell or double liner-on-target gas-puff configurations for the production of thermonuclear neutrons has, to our knowledge, not been explored in the literature. While the triple-shell concept has been demonstrated on other platforms for the production of X-rays, to our knowledge there have not been experiments conducted with this load geometry with axial premagnetization. If positive results are achieved on LTD, extending the semi-analytic model to include Ne and double liners could prove useful in designing future multi-MA experiments.

Bibliography

[1] M. A. Liberman, J. S. De Groot, A. Toor, and R. B. Spielman. *Physics of High-Density Z-Pinch Plasmas*. Springer New York, New York, NY, 1999.

[2] D. D. Ryutov, M. S. Derzon, and M. K. Matzen. The physics of fast Z pinches. *Reviews of Modern Physics*, 72:167–223, 2000.

[3] M. G. Haines. A review of the dense Z-pinch. *Plasma Physics and Controlled Fusion*, 53:093001, 2011.

[4] J. L. Giuliani and R. J. Commisso. A Review of the Gas-Puff Z-Pinch as an X-Ray and Neutron Source. *IEEE Transactions on Plasma Science*, 43:2385–2453, 2015.

[5] D. Mosher, S. J. Stephanakis, K. Hain, C. M. Dozier, and F. C. Young. Electrical characteristics of high energy-density exploded wire plasmas. *Annals of the New York Academy of Sciences*, 251:632–648, 1975.

[6] S. V. Lebedev, R. Aliaga-Rossel, J. P. Chittenden, I. H. Mitchell, A. E. Dangor, M. G. Haines, and J. F. Worley. Coronal plasma behavior of the Z pinch produced from carbon and cryogenic deuterium fibers. *Physics of Plasmas*, 5:3366–3372, 1998.

[7] J. D. Sethian, A. E. Robson, K. A. Gerber, and A. W. DeSilva. Enhanced stability and neutron production in a dense Z-pinch plasma formed from a frozen deuterium fiber. *Physical Review Letters*, 59:892–895, 1987.

[8] J. Hammel. The High Density Z-pinch II experiments. In *AIP Conference Proceedings*, volume 195, pages 303–307. AIP, 1989.

[9] J. D. Sethian, A. E. Robson, K. A. Gerber, and A. W. DeSilva. The NRL frozen deuterium fiber Z-pinch experiment. In *AIP Conference Proceedings*, volume 195, pages 308–314. AIP, 1989.

[10] H. U. Rahman, F. J. Wessel, and N. Rostoker. Staged Z-pinch. *Physical Review Letters*, 74:714–717, 1995.

[11] T. W. L. Sanford, G. O. Allshouse, B. M. Marder, T. J. Nash, R. C. Mock, R. B. Spielman, J. F. Seamen, J. S. McGurn, D. Jobe, T. L. Gilliland, M. Vargas, K. W. Struve, W. A. Stygar, M. R. Douglas, M. K. Matzen, J. H. Hammer, J. S. De Groot, J. L. Eddleman, D. L. Peterson, D. Mosher, K. G. Whitney, J. W. Thornhill, P. E. Pulsifer, J. P. Apruzese, and Y. Maron. Improved Symmetry Greatly Increases X-Ray Power from Wire-Array Z-Pinches. *Physical Review Letters*, 77:5063–5066, 1996.

[12] R. B. Spielman, C. Deeney, G. A. Chandler, M. R. Douglas, D. L. Fehl, M. K. Matzen, D. H. McDaniel, T. J. Nash, J. L. Porter, T. W. L. Sanford, J. F. Seamen, W. A. Stygar, K. W. Struve, S. P. Breeze, J. S. McGurn, J. A. Torres, D. M. Zagar, T. L. Gilliland, D. O. Jobe, J. L. McKenney, R. C. Mock, M. Vargas, T. Wagoner, and D. L. Peterson. Tungsten wire-array Z-pinch experiments at 200 TW and 2 MJ. *Physics of Plasmas*, 5:2105–2111, 1998.

[13] S. V. Lebedev, R. Aliaga-Rossel, S. N. Bland, J. P. Chittenden, A. E. Dangor, M. G. Haines, and I. H. Mitchell. The dynamics of wire array Z-pinch implosions. *Physics of Plasmas*, 6:2016–2022, 1999.

[14] J. P. Chittenden, S. V. Lebedev, S. N. Bland, F. N. Beg, and M. G. Haines. One-, two-, and three-dimensional modeling of the different phases of wire array Z-pinch evolution. *Physics of Plasmas*, 8:2305–2314, 2001.

[15] S. A. Slutz, M. C. Herrmann, R. A. Vesey, A. B. Sefkow, D. B. Sinars, D. C. Rovang, K. J. Peterson, and M. E. Cuneo. Pulsed-power-driven cylindrical liner implosions of laser preheated fuel magnetized with an axial field. *Physics of Plasmas*, 17:056303, 2010.

[16] M. E. Cuneo, M. C. Herrmann, D. B. Sinars, S. A. Slutz, W. A. Stygar, R. A. Vesey, A. B. Sefkow, G. A. Rochau, G. A. Chandler, J. E. Bailey, J. L. Porter, R. D. McBride, D. C. Rovang, M. G. Mazarakis, E. P. Yu, D. C. Lamppa, K. J. Peterson, C. Nakhleh, S. B. Hansen, A. J. Lopez, M. E. Savage, C. A. Jennings, M. R. Martin, R. W. Lemke, B. W. Atherton, I. C. Smith, P. K. Rambo, M. Jones, M. R. Lopez, P. J. Christenson, M. A. Sweeney, B. Jones, L. A. McPherson, E. Harding, M. R. Gomez, P. F. Knapp, T. J. Awe, R. J. Leeper, C. L. Ruiz, G. W. Cooper, K. D. Hahn, J. McKenney, A. C. Owen, G. R. McKee, G. T. Leifeste, D. J. Ampleford, E. M. Waisman, A. Harvey-Thompson, R. J. Kaye, M. H. Hess, S. E. Rosenthal, and M. K. Matzen. Magnetically Driven Implosions for Inertial Confinement Fusion at Sandia National Laboratories. *IEEE Transactions on Plasma Science*, 40:3222–3245, 2012.

[17] J. Bailey, Y. Ettinger, A. Fisher, and N. Rostoker. Gaspuff Z pinches with D2 and D2 Ar mixtures. *Applied Physics Letters*, 40:460–462, 1982.

[18] H. Sze, P. L. Coleman, B. H. Failor, A. Fisher, J. S. Levine, Y. Song, E. M. Waisman, J. P. Apruzese, Y. K. Chong, J. Davis, F. L. Cochran, J. W. Thornhill, A. L. Velikovich, B. V. Weber, C. Deeney, C. A. Coverdale, and R. Schneider. Initial results for an argon Z pinch using a double-shell gas puff. *Physics of Plasmas*, 7:4223, 2000.

[19] S. A. Chaikovsky, A. Yu. Labetsky, V. I. Oreshkin, A. V. Shishlov, R. B. Baksht, A. V. Fedunin, and A. G. Rousskikh. The K-shell radiation of a double gas puff z-pinch with an axial magnetic field. *Laser and Particle Beams*, 21:255–264, 2003.

[20] F. C. Young, R. J. Commisso, D. P. Murphy, J. P. Apruzese, D. Mosher, A. L. Velikovich, P. L. Coleman, J. W. Banister, B. H. Failor, J. S. Levine, N. Qi, and H. M. Sze. Measurement and Analysis of Continuum Radiation From a Large-Diameter Long Implosion Time Argon Gas PuffZ-Pinch at 6 MA. *IEEE Transactions on Plasma Science*, 34:2312–2324, 2006.

[21] C. A. Coverdale, C. Deeney, A. L. Velikovich, R. W. Clark, Y. K. Chong, J. Davis, J. Chittenden, C. L. Ruiz, G. W. Cooper, A. J. Nelson, J. Franklin, P. D. LePell, J. P. Apruzese, J. Levine, J. Banister, and N. Qi. Neutron production and implosion characteristics of a deuterium gas-puff Z pinch. *Physics of Plasmas*, 14:022706, 2007.

[22] E. Kroupp, D. Osin, A. Starobinets, V. Fisher, V. Bernshtam, L. Weingarten, Y. Maron, I. Uschmann, E. Förster, A. Fisher, M. E. Cuneo, C. Deeney, and J. L. Giuliani. Ion Temperature and Hydrodynamic-Energy Measurements in a Z-Pinch Plasma at Stagnation. *Physical Review Letters*, 107:105001, 2011.

[23] D. Klir, A. V. Shishlov, P. Kubes, K. Rezac, F. I. Fursov, V. A. Kokshenev, B. M. Kovalchuk, J. Kravarik, N. E. Kurmaev, A. Yu Labetsky, and N. A. Ratakhin. Deuterium gas puff Z-pinch at currents of 2 to 3 mega-ampere. *Physics of Plasmas*, 19:032706, 2012.

[24] J. Ongena, R. Koch, R. Wolf, and H. Zohm. Magnetic-confinement fusion. *Nature Physics*, 12:398–410, 2016.

[25] R. Betti and O. A. Hurricane. Inertial-confinement fusion with lasers. *Nature Physics*, 12:435–448, 2016.

[26] I. R. Lindemuth and R. C. Kirkpatrick. Parameter space for magnetized fuel targets in inertial confinement fusion. *Nuclear Fusion*, 23:263–284, 1983.

[27] R. E. Siemon, I. R. Lindemuth, and K. F. Schoenberg. Why Magnetized Target Fusion Offers A Low-Cost Development Path for Fusion Energy. *Comments Plasma Phys. Controlled Fusion*, 18:363, 1999.

[28] I. R. Lindemuth and R. E. Siemon. The fundamental parameter space of controlled thermonuclear fusion. *American Journal of Physics*, 77:407–416, 2009.

[29] G. A. Wurden, S. C. Hsu, T. P. Intrator, T. C. Grabowski, J. H. Degnan, M. Domonkos, P. J. Turchi, E. M. Campbell, D. B. Sinars, M. C. Herrmann, R. Betti, B. S. Bauer, I. R. Lindemuth, R. E. Siemon, R. L. Miller, M. Laberge, and M. Delage. Magneto-Inertial Fusion. *Journal of Fusion Energy*, 35:69–77, 2016.

[30] U. Shumlak, R. P. Golingo, B. A. Nelson, and D. J. Den Hartog. Evidence of Stabilization in the Z-Pinch. *Physical Review Letters*, 87:205005, 2001.

[31] U. Shumlak, J. Chadney, R. P. Golingo, D. J. Den Hartog, M. C. Hughes, S. D. Knecht, W. Lowrie, V. S. Lukin, B. A. Nelson, R. J. Oberto, J. L. Rohrbach, M. P. Ross, and G. V. Vogman. The Sheared-Flow Stabilized Z-Pinch. *Fusion Science and Technology*, 61:119–124, 2012.

[32] S. A. Slutz and R. A. Vesey. High-Gain Magnetized Inertial Fusion. *Physical Review Letters*, 108:025003, 2012.

[33] H. U. Rahman, F. J. Wessel, R. Presura, and P. Ney. High gain fusion in a Staged Z-pinch. In *2013 19th IEEE Pulsed Power Conference (PPC)*, pages 1–6. IEEE, 2013.

[34] F. J. Wessel, B. Moosman, N. Rostoker, Y. Song, A. Van Drie, P. Ney, and H. U. Rahman. UCI staged Z pinch facility. In *The fourth international conference on dense z-pinches*, volume 39, pages 39–45. ASCE, 1997.

[35] J. D. Lawson. Some Criteria for a Power Producing Thermonuclear Reactor. *Proceedings of the Physical Society. Section B*, 70:6–10, 1957.

[36] H. U. Rahman, E. L. Ruden, K. D. Strohmaier, F. J. Wessel, and G. Yur. Closed cycle cryogenic fiber extrusion system. *Review of Scientific Instruments*, 67:3533–3536, 1996.

[37] P. Ney, H. U. Rahman, F. J. Wessel, and N. Rostoker. Staged Z pinch for controlled fusion. *Physics of Plasmas*, 8:616, 2001.

[38] T. W. Hussey, N. F. Roderick, and D. A. Kloc. Scaling of (MHD) instabilities in imploding plasma liners. *Journal of Applied Physics*, 51:1452–1463, 1980.

[39] S. I. Braginskii. Transport processes in a plasma. *Reviews of Plasma Physics*, 1:205, 1965.

[40] E. M. Epperlein and M. G. Haines. Plasma transport coefficients in a magnetic field by direct numerical solution of the Fokker-Planck equation. *Physics of Fluids*, 29:1029, 1986.

[41] H. U. Rahman, F. J. Wessel, P. Ney, R. Presura, R. Ellahi, and P. K. Shukla. Shock waves in a Z-pinch and the formation of high energy density plasma. *Physics of Plasmas*, 19:122701, 2012.

[42] D. Klir, P. Kubes, K. Rezac, J. Cikhardt, J. Kravarik, O. Sila, A. V. Shishlov, B. M. Kovalchuk, N. A. Ratakhin, V. A. Kokshenev, A. Yu Labetsky, R. K. Cherdizov, F. I. Fursov, N. E. Kurmaev, G. N. Dudkin, B. A. Nechaev, V. N. Padalko, H. Orcikova, and K. Turek. Efficient neutron production from a novel configuration of deuterium gas-puff z-pinch. *Physical Review Letters*, 112:1–5, 2014.

[43] H. U. Rahman, F. J. Wessel, N. Rostoker, and P. H. Ney. High yield fusion in a staged Z-pinch. *Journal of Plasma Physics*, 75:749, 2009.

[44] W. H. Bennett. Magnetically Self-Focussing Streams. *Phys. Rev.*, 45:890–897, 1934.

[45] R. S. Pease. Equilibrium Characteristics of a Pinched Gas Discharge Cooled by Bremsstrahlung Radiation. *Proceedings of the Physical Society. Section B*, 70:11–23, 1957.

[46] S. I. Braginskii. The Behavior of a Completely Ionized Plasma in a Strong Magnetic Field. *J. Exptl. Theoret. Phys. (U.S.S.R.)*, 6:645–654, 1958.

[47] G. B. Rybicki and A. P. Lightman. *Radiative Processes in Astrophysics*. Wiley-Interscience, New York, 1979.

[48] G. Bekefi. *Radiation Processes in Plasmas*. John Wiley & Sons, Inc., New York, 1966.

[49] J. D. Huba. *NRL Plasma Formulary*. Naval Research Laboratory, Washington, D.C., 2016.

[50] I. R. Lindemuth. Two-dimensional fiber ablation in the solid-deuterium Z pinch. *Physical Review Letters*, 65:179–182, 1990.

[51] I. R. Lindemuth. The ignition design space of magnetized target fusion. *Physics of Plasmas*, 22:122712, 2015.

[52] A. B. Sefkow, S. A. Slutz, J. M. Koning, M. M. Marinak, K. J. Peterson, D. B. Sinars, and R. A. Vesey. Design of magnetized liner inertial fusion experiments using the Z facility. *Physics of Plasmas*, 21:072711, 2014.

[53] J. Narkis, H. U. Rahman, P. Ney, M. P. Desjarlais, F. J. Wessel, F. Conti, J. C. Valenzuela, and F. N. Beg. Shock formation in Ne, Ar, Kr, and Xe on deuterium gas puff implosions. *Physics of Plasmas*, 23:122706, 2016.

[54] H. U. Rahman, E. Ruskov, P. Ney, F. Conti, J. C. Valenzuela, N. Aybar, J. Narkis, F. Beg, E. Dutra, and A. Covington. Ar and Kr on deuterium gas-puff Staged Z-pinch implosions on a 1-MA driver: Experiment and Simulation. *Physics of Plasmas*, 26:052706, 2019.

[55] Lord Rayleigh. The Form of Standing Waves on the Surface of Running Water. *Proceedings of the London Mathematical Society*, s1-15:69–78, 1883.

[56] G. I. Taylor. The instability of liquid surfaces when accelerated in a direction perpendicular to their planes. I. *Proceedings of the Royal Society of London. Series A. Mathematical and Physical Sciences*, 201:192–196, 1950.

[57] M. Kruskal and M. Schwarzschild. Some instabilities of a completely ionized plasma. *Proceedings of the Royal Society of London. Series A. Mathematical and Physical Sciences*, 223:348–360, 1954.

[58] S. Chandrasekhar. *Hydromagnetic and Hydrodynamic Stability*. Oxford University Press, London, 1961.

[59] E. G. Harris. Rayleigh-Taylor Instabilities of a Collapsing Cylindrical Shell in a Magnetic Field. *Physics of Fluids*, 5:1057, 1962.

[60] M. R. Douglas, J. S. De Groot, and R. B. Spielman. The magneto-RayleighTaylor instability in dynamic z pinches. *Laser and Particle Beams*, 19:527–540, 2001.

[61] H. U. Rahman, P. Ney, N. Rostoker, A. Van Drie, and F. J. Wessel. Control of the Rayleigh-Taylor instability in a staged Z pinch. *Physics of Plasmas*, 11:5595, 2004.

[62] D. Mikitchuk, C. Stollberg, R. Doron, E. Kroupp, Y. Maron, H. R. Strauss, A. L. Velikovich, and J. L. Giuliani. Mitigation of Instabilities in a Z-Pinch Plasma by a Preembedded Axial Magnetic Field. *IEEE Transactions on Plasma Science*, 42:2524–2525, 2014.

[63] A. G. Rousskikh, A. S. Zhigalin, V. I. Oreshkin, V. Frolova, A. L. Velikovich, G. Yu Yushkov, and R. B. Baksht. Effect of the axial magnetic field on a metallic gas-puff pinch implosion. *Physics of Plasmas*, 23:063502, 2016.

[64] A. L. Velikovich, F. L. Cochran, and J. Davis. Suppression of Rayleigh-Taylor Instability in Z-Pinch Loads with Tailored Density Profiles. *Physical Review Letters*, 77:853–856, 1996.

[65] H. Sze, J. S. Levine, J. Banister, B. H. Failor, N. Qi, P. Steen, A. L. Velikovich, J. Davis, and A. Wilson. Magnetic Rayleigh-Taylor instability mitigation and efficient radiation production in gas puff Z-pinch implosions. *Physics of Plasmas*, 14:056307, 2007.

[66] D. R. Welch, D. V. Rose, R. E. Clark, C. B. Mostrom, W. A. Stygar, and R. J. Leeper. Fully Kinetic Particle-in-Cell Simulations of a Deuterium Gas Puff z Pinch. *Physical Review Letters*, 103:255002, 2009.

[67] J. P. Chittenden, S. V. Lebedev, C. A. Jennings, S. N. Bland, and A. Ciardi. X-ray generation mechanisms in three-dimensional simulations of wire array Z-pinches. *Plasma Physics and Controlled Fusion*, 46:B457–B476, 2004.

[68] J. P. Chittenden, A. Ciardi, C. A. Jennings, S. V. Lebedev, D. A. Hammer, S. A. Pikuz, and T. A. Shelkovenko. Structural Evolution and Formation of High-Pressure Plasmas in X Pinches. *Physical Review Letters*, 98:025003, 2007.

[69] P.-A. Gourdain, R. J. Concepcion, M. T. Evans, J. B. Greenly, D. A. Hammer, C. L. Hoyt, E. Kroupp, B. R. Kusse, Y. Maron, A. S. Novick, S. A. Pikuz, N. Qi, G. Rondeau, E. Rosenberg, P. C. Schrafel, C. E. Seyler, and T. C. Shelkovenko. Initial magnetic field compression studies using gas-puff Z -pinches and thin liners on COBRA. *Nuclear Fusion*, 53:083006, 2013.

[70] C. E. Seyler, M. R. Martin, and N. D. Hamlin. Helical instability in MagLIF due to axial flux compression by low-density plasma. *Physics of Plasmas*, 25:062711, 2018.

[71] T. J. Awe, C. A. Jennings, R. D. McBride, M. E. Cuneo, D. C. Lamppa, M. R. Martin, D. C. Rovang, D. B. Sinars, S. A. Slutz, A. C. Owen, K. Tomlinson, M. R. Gomez, S. B. Hansen, M. C. Herrmann, M. C. Jones, J. L. McKenney, G. K. Robertson, G. A. Rochau,

M. E. Savage, D. G. Schroen, and W. A. Stygar. Modified helix-like instability structure on imploding z-pinch liners that are pre-imposed with a uniform axial magnetic field. *Physics of Plasmas*, 21:056303, 2014.

[72] A. B. Sefkow. On the helical instability and efficient stagnation pressure production in thermonuclear magnetized inertial fusion. In *APS Meeting Abstracts*, 2016.

[73] D. A. Yager-Elorriaga, P. Zhang, A. M. Steiner, N. M. Jordan, P. C. Campbell, Y. Y. Lau, and R. M. Gilgenbach. Discrete helical modes in imploding and exploding cylindrical, magnetized liners. *Physics of Plasmas*, 23:124502, 2016.

[74] M. H. Frese. MACH2: A Two-Dimensional Magnetohydrodynamic Simulation Code for Complex Experimental Configurations. Technical report, Mission Research Corporation, Albuquerque, NM, 1987.

[75] M. M. Marinak, G. D. Kerbel, N. A. Gentile, O. Jones, D. Munro, S. Pollaine, T. R. Dittrich, and S. W. Haan. Three-dimensional HYDRA simulations of National Ignition Facility targets. *Physics of Plasmas*, 8:2275–2280, 2001.

[76] J. M. Koning, G. D. Kerbel, and M. M. Marinak. The Hydra Magnetohydrodynamics Package. In *APS Meeting Abstracts*, page NP8.101, 2009.

[77] R. D. McBride and S. A. Slutz. A semi-analytic model of magnetized liner inertial fusion. *Physics of Plasmas*, 22:052708, 2015.

[78] M. Rosenbluth, R. Garwin, and A. Rosenbluth. Infinite conductivity theory of the pinch. Technical report, Los Alamos Scientific Laboratory, Los Alamos, 1954.

[79] D. Potter. The formation of high-density z-pinches. *Nuclear Fusion*, 18:813–823, 1978.

[80] M. A. Liberman and A. L. Velikovich. *Physics of Shock Waves in Gases and Plasmas*. Springer-Verlag, Berlin, 1986.

[81] Ya. B. Zel'dovich and Yu. P. Raizer. *Physics of Shock Waves and High-Temperature Hydrodynamic Phenomena*. Academic Press, New York, 1967.

[82] P. M. Bellan. *Fundamentals of Plasma Physics*. Cambridge University Press, Cambridge, 2006.

[83] M. R. Weis, P. Zhang, Y. Y. Lau, I. M. Rittersdorf, J. C. Zier, R. M. Gilgenbach, M. H. Hess, and K. J. Peterson. Temporal evolution of surface ripples on a finite plasma slab subject to the magneto-Rayleigh-Taylor instability. *Physics of Plasmas*, 21:122708, 2014.

[84] M. R. Weis, P. Zhang, Y. Y. Lau, P. F. Schmit, K. J. Peterson, M. Hess, and R. M. Gilgenbach. Coupling of sausage, kink, and magneto-Rayleigh-Taylor instabilities in a cylindrical liner. *Physics of Plasmas*, 22:032706, 2015.

[85] C. H. Su and C. S. Gardner. Korteweg-de Vries Equation and Generalizations. III. Derivation of the Korteweg-de Vries Equation and Burgers Equation. *Journal of Mathematical Physics*, 10:536–539, 1969.

[86] J. Narkis, H. U. Rahman, F. J. Wessel, and F. N. Beg. Investigation of magnetic flux transport and shock formation in a staged Z-pinch. *Physics of Plasmas*, 24:102514, 2017.

[87] S. Hussain and S. Mahmood. Korteweg-de Vries Burgers equation for magnetosonic wave in plasma. *Physics of Plasmas*, 18:052308, 2011.

[88] S. Bujarbarua and P. K. Shukla. Magnetosonic shocks in nonlinear dispersive media. *Astrophysics and Space Science*, 69:515–519, 1980.

[89] T. Taniuti and C.-C. Wei. Reductive perturbation method in nonlinear wave propagation I. *Journal of the Physical Society of Japan*, 24:941–946, 1968.

[90] H. Leblond. The reductive perturbation method and some of its applications. *Journal of Physics B: Atomic, Molecular and Optical Physics*, 41:043001, 2008.

[91] W. Malfliet. The tanh method: A tool for solving certain classes of non-linear PDEs. *Mathematical Methods in the Applied Sciences*, 28:2031–2035, 2005.

[92] R. E. Peterkin Jr. and M. H. Frese. MACH: A Reference Manual - Second Edition. Technical report, Air Force Research Laboratory, Albuquerque, NM, 2000.

[93] D. E. Post, R. V. Jensen, C. B. Tarter, W. H. Grasberger, and W. A. Lokke. Steady-state radiative cooling rates for low-density, high-temperature plasmas. *Atomic Data and Nuclear Data Tables*, 20:397–439, 1977.

[94] A. L. Velikovich, J. L. Giuliani, and S. T. Zalesak. Magnetic flux and heat losses by diffusive, advective, and Nernst effects in magnetized liner inertial fusion-like plasma. *Physics of Plasmas*, 22:042702, 2015.

[95] J. J. MacFarlane, I. E. Golovkin, and P. R. Woodruff. HELIOS-CR – A 1-D radiation-magnetohydrodynamics code with inline atomic kinetics modeling. *Journal of Quantitative Spectroscopy and Radiative Transfer*, 99:381–397, 2006.

[96] J. R. Rygg, J. A. Frenje, C. K. Li, F. H. Séguin, R. D. Petrasso, D. D. Meyerhofer, and C. Stoeckl. Electron-ion thermal equilibration after spherical shock collapse. *Physical Review E*, 80:026403, 2009.

[97] L. L. Cowie and C. F. McKee. The evaporation of spherical clouds in a hot gas. I - Classical and saturated mass loss rates. *The Astrophysical Journal*, 211:135, 1977.

[98] G. A. Moses and J. J. Duderstadt. Improved treatment of electron thermal conduction in plasma hydrodynamics calculations. *Physics of Fluids*, 20:762–770, 1977.

[99] A. Nishiguchi, K. Mima, H. Azechi, N. Miyanaga, and S. Nakai. Kinetic effects of electron thermal conduction on implosion hydrodynamics. *Physics of Fluids B: Plasma Physics*, 4:417–422, 1992.

[100] J. Narkis, H. U. Rahman, J. C. Valenzuela, F. Conti, R. D. McBride, D. Venosa, and F. N. Beg. A semi-analytic model of gas-puff liner-on-target magneto-inertial fusion. *Physics of Plasmas*, 26:032708, 2019.

[101] J. Liu, D. Sprecher, C. Jungen, W. Ubachs, and F. Merkt. Determination of the ionization and dissociation energies of the deuterium molecule (D2). *The Journal of Chemical Physics*, 132:154301, 2010.

[102] H.-S. Bosch and G. M. Hale. Improved formulas for fusion cross-sections and thermal reactivities. *Nuclear Fusion*, 32:611–631, 1992.

[103] S. Atzeni and J. Meyer-ter-Vehn. *The Physics of Inertial Fusion: Beam Plasma Interaction, Hydrodynamics, Hot Dense Matter*. Clarendon Press, Oxford, 2004.

[104] M. M. Basko, A. J. Kemp, and J. Meyer-ter-Vehn. Ignition conditions for magnetized target fusion in cylindrical geometry. *Nuclear Fusion*, 40:59–68, 2000.

[105] F. Conti, J. C. Valenzuela, N. Aybar, F. J. Wessel, M. P. Ross, J. Narkis, H. U. Rahman, E. Ruskov, and F. N. Beg. Characterization of a Liner-on-Target Gas Injector for Staged Z-Pinch Experiments. *IEEE Transactions on Plasma Science*, 46:3855–3863, 2018.

[106] W. B. VanderHeyden and B. A. Kashiwa. Compatible Fluxes for van Leer Advection. *Journal of Computational Physics*, 146:1–28, 1998.

[107] I. R. Lindemuth. An extended study of the ignition design space of magnetized target fusion. *Physics of Plasmas*, 24:055602, 2017.

[108] B. L. Bures and M. Krishnan. An alternative scaling model for neutron production in Z-pinch devices. *Physics of Plasmas*, 19:112702, 2012.

[109] A. L. Velikovich, R. W. Clark, J. Davis, Y. K. Chong, C. Deeney, C. A. Coverdale, C. L. Ruiz, G. W. Cooper, A. J. Nelson, J. Franklin, and L. I. Rudakov. Z-pinch plasma neutron sources. *Physics of Plasmas*, 14:022701, 2007.

[110] N. Qi, S. V. Rocco, J. Engelbrecht, E. S. Lavine, P. De Grouchy, J. T. Banasek, L. Atoyan, T. Byvank, W. M. Potter, J. B. Greenly, D. A. Hammer, B. R. Kusse, S. A. Pikuz, T. A. Shelkovenko, E. Kroupp, A. Fisher, and Y. Maron. Study of Triple Ar Gas Puff Z-Pinches on 0.9-MA, 200-ns COBRA. *IEEE Transactions on Plasma Science*, 46:3864–3870, 2018.